KOBELCO TECHNOLOGY REVIEW

No. 39 Nov. 2021

Feature-Ⅰ: Energy and Environment
Feature-Ⅱ: Advanced Materials Business

Contents

Feature-Ⅰ Energy and Environment

Feature-Ⅱ Advanced Materials Business

Published by

Technical Development Group
Kobe Steel, Ltd.

5-5, Takatsukadai 1-chome,
Nishi-ku, Kobe, HYOGO 651-2271, JAPAN
https://www.kobelco.co.jp

Editorial Office: **Kobelco Business Partners Co., Ltd.**
2-4, Wakinohama-Kaigandori 2-chome,
Chuo-ku, Kobe, HYOGO 651-8585,
JAPAN
Fax: +81-78-261-7843
E-mail: rd-office@kobelco.com

Demonstration of Hydrogen Refueling Station Using Renewable Energy for Fuel Cell Vehicles

Dr. Akitoshi FUJISAWA[*1] ・ **Shigeru KINOSHITA**[*1] ・ **Dr. Shin-ichi MIURA**[*2] ・ **Sueki NAKAO**[*3] ・ **Fumiaki SUZUKI**[*4] ・ **Kazuhiro YAMASHITA**[*4]

[*1] Mechanical Engineering Research Laboratory, Technical Development Group
[*2] Rotating Machinery Engineering Department, Rotating Machinery Business unit, Machinery Business
[*3] Kobelco Eco-Solutions Co.,Ltd.
[*4] Shinko Engineering & Maintenance Co.,Ltd

Abstract

To significantly reduce CO_2 emissions during the production of hydrogen for hydrogen refueling stations, it is effective to use water-electrolysis hydrogen generated with renewable electricity. Kobe Steel has devised a configuration to add a hydrogen generator using a solid-polymer-electrolyte water electrolyzer (20 Nm^3/h) and equipment for storing generated hydrogen at a high pressure (45 MPa) to a standard hydrogen refueling station (hydrogen supply capacity 300 Nm^3/h) and has designed and built a demonstration plant. The demonstration included the operation of the water-electrolysis hydrogen generator for about 780 hours with the variable power source without any problems with followability and durability. In addition, the function of the entire system designed was verified by the operation linked with the hydrogen refueling station. In the future, further cost reduction and efficiency improvement will be considered. It is necessary to set a social value for hydrogen, which emits less CO_2.

Introduction

Japan's Fifth Strategic Energy Plan was formulated in 2018 by the Agency for Natural Resources and Energy of the Ministry of Economy, Trade and Industry (METI).1) This Strategic Energy Plan positions hydrogen as the secondary energy, and hydrogen infrastructure is becoming an energy infrastructure that Japan should develop as a measure against global warming. In December 2017, the Ministerial Council on Renewable Energy, Hydrogen and Related Issues enacted the Basic Hydrogen Strategy.2) With a view to 2050, this basic strategy has been established as an action plan covering the period up to 2030 to realize a hydrogen society, as well as the direction and vision that the public and private sectors should share as concepts and goals to aim at in the future. In addition, this Basic Hydrogen Strategy is directed at "establishing a fully CO_2-free hydrogen supply system by combining hydrogen production with CCS[Note 1] or by utilizing hydrogen based on renewable energy" around 2040 as a CO_2 reduction measure during hydrogen production.

Furthermore, the New Energy and Industrial Technology Development Organization (NEDO) is developing a hydrogen production technology based on alkaline water electrolysis using renewable energy generated by wind power, for example, in the "Advancement of Hydrogen Technologies and Utilization Project, (FY2014-FY2017); Research and development of low-cost hydrogen production system."

On the other hand, against the backdrop of the fact that fuel cell vehicles (hereinafter referred to as "FCVs"), using hydrogen as fuel, are attracting attention as Zero Emission Vehicles in the mobility field, the development and network construction of hydrogen refueling stations for FCVs are in progress. The hydrogen sources for hydrogen refueling stations employ off-site supply, including the transport and supply of by-product hydrogen from large-scale natural gas reforming and refinery plants, as well as on-site hydrogen supply that locally manufactures hydrogen using natural gas or liquefied petroleum gas (LPG) as raw material.

In Japan, the construction of a hydrogen supply network is being prioritized; however, since the hydrogen is based on fossil fuels, CO_2 is currently emitted during the production process. Hence, it is expected that there will be a greater increase in the social demand for the use of hydrogen based on renewable energy, which can significantly reduce the amount of CO_2 emissions.

The hydrogen supplied to the hydrogen refueling station is required to be high-purity hydrogen of 4N (99.99%) or higher. Also, it is required to be easy to use and handle in urban areas without any problems such as waste liquid emissions and corrosiveness. Hence, the method using a solid-polymer-type water-electrolysis hydrogen generator, which has already been commercialized and can produce high-purity hydrogen, is considered to be advantageous for producing hydrogen based on renewable energy for this application. Meanwhile, regarding its application to hydrogen refueling stations, there are challenges, including the reduction of hydrogen

---

[Note 1] CCS stands for Carbon Dioxide Capture and Storage.

production cost and improvement of hydrogen production efficiency.

Hence, in collaboration with Kobelco Eco-Solutions Co.,Ltd. and Shinko Engineering & Maintenance Co.,Ltd, Kobe Steel has jointly developed technologies related to refueling stations using hydrogen based on renewable energy and conducted a demonstration testing (hereinafter referred to as "the present development"). This paper gives an outline of these activities.

1. Configuration of facility for demonstrating refueling station to supply hydrogen based on renewable energy

The present development aims to supply water-electrolysis hydrogen based on renewable energy to a hydrogen refueling station. Hence, it was planned to install a water-electrolysis hydrogen generator and hydrogen storage facility (**Fig. 1**) with a capacity of 20 Nm^3/h adjacent to a standard-scale hydrogen refueling station (rated 300 Nm^3/h). This is because a 300 Nm^3/h water-electrolysis hydrogen generator at the current cost will not be acceptable for a hydrogen refueling station and not be easily adapted to large-scale renewable energy power of MW-class. The process capacity of 20 Nm^3/h corresponds to approximately 6% of the 300 Nm^3/h rating, and the CO_2 reduction effect is limited. However, it can be replaced with a larger-scale one as the demand increases.

The demonstration facility used in the present development was designed to comply with the regulations applicable to hydrogen refueling stations. The facility was annexed to the hydrogen refueling station installed in Kobe Steel's Takasago Works to verify its own equipment. **Fig. 2** shows the layout and installation of this facility. The following outlines its main components.

(1) Water-electrolysis hydrogen generator

A 20 Nm^3/h water-electrolysis hydrogen generator [3)] manufactured by Kobelco Eco-Solutions, Co., Ltd. was used (**Fig. 3**). This generator is a development product with an electrical current density 1.4 times greater than that of the conventional model and has been designed with the aim of reducing initial cost and downsizing. It has also been configured as a package type that can be installed outdoors, assuming installation in a hydrogen refueling station.

(2) Hydrogen storage unit

When hydrogen is made using power based on

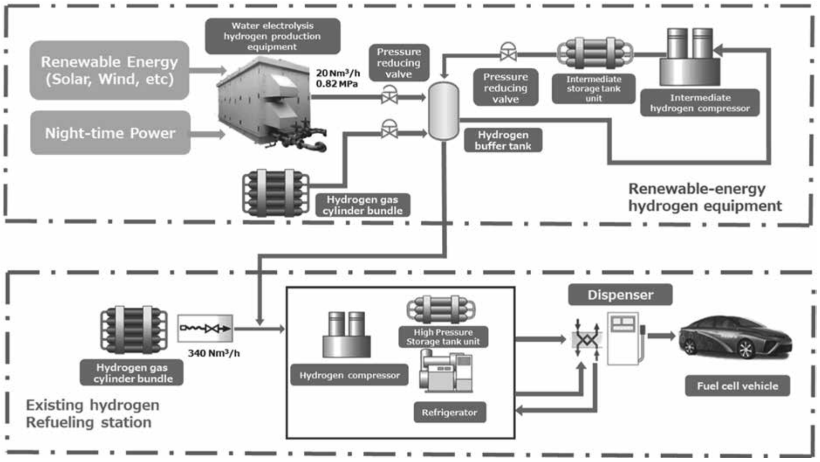

Fig. 1 Conceptual diagram of refueling station of hydrogen based on renewable energy

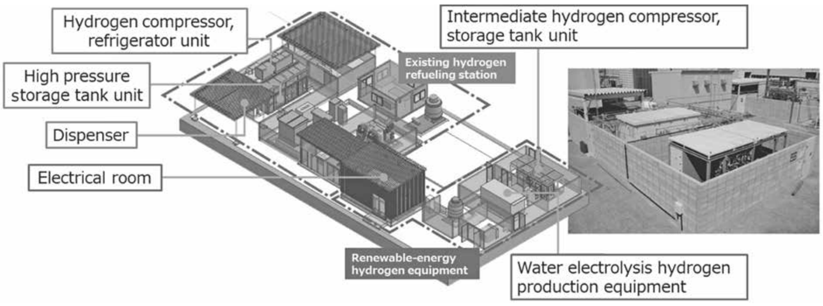

Fig. 2 Demonstration facility for refueling station of hydrogen based on renewable energy

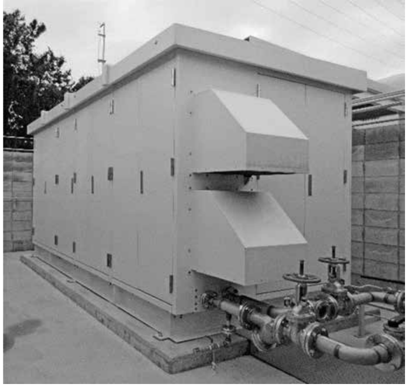

Fig. 3 Water-electrolysis hydrogen generator

renewable energy, a fluctuating power source, the hydrogen flow rate fluctuates in accordance with the power. In addition, the hydrogen demand at the hydrogen refueling station is unsteady, due to the filling demand for FCVs. Therefore, it is necessary to temporarily store the generated hydrogen in the case where the demand is low. Hence, the present development has adapted a system comprising an intermediate compressor and an intermediate accumulator, wherein hydrogen is stored as compressed gas.

Since the hydrogen storage capacity depends on the pressure and capacity settings of the intermediate accumulator, it is necessary to design in accordance with the hydrogen production capacity and the demand on the side of the hydrogen refueling station. The hydrogen storage capacity for the present development was set to approximately 90 Nm^3, which enables hydrogen supply to about two FCVs and can operate the water-electrolysis hydrogen generator for approximately 4 hours.

The pressure of the intermediate accumulator was set to a normal operation pressure of 45 MPa, which is equivalent to that of the accumulator used for unloading from the hydrogen curdle at an off-site hydrogen refueling station. In addition, two intermediate accumulators were installed to deal with such problems as valve troubles, for example. The accumulator capacity that meets the above requirements was studied, and an accumulator with 150-liter capacity was adopted.

In addition, a low-pressure hydrogen buffer tank was installed to suppress the pressure fluctuation of the hydrogen supplied to the hydrogen refueling station. Connected to this were the inlet piping of the intermediate compressor, the outlet piping of the intermediate accumulator, the outlet piping of the water-electrolysis hydrogen generator, and the hydrogen supply piping to the hydrogen refueling station. This construction aims at minimizing the equipment configuration so as to respond to each operational pattern of hydrogen production, storage, and supply.

2. Demonstration operation

2.1 Verification of water-electrolysis hydrogen generator

The applications of conventional water-electrolysis hydrogen generators have been predominantly for industrial hydrogen supply and mainly focused on hydrogen production using a stable power source. On the other hand, the refueling station of hydrogen based on renewable energy produces hydrogen by using renewable energy power, which is generally regarded as an unstable power source. Hence, in the present development, a hydrogen production test was conducted using a solar-cell simulating power source to verify the followability and durability of the water-electrolysis hydrogen generator with respect to the photovoltaic power source, whose power generation fluctuates particularly steeply among the power sources based on renewable energy.

The amount of photovoltaic power generation varies depending on the season and the weather. Hence, in the present development, "summer", "intermediate period", and "winter" were set as the seasons, and "sunny", "cloudy" and "rainy" were set for the weather. The water-electrolysis hydrogen generator was operated on the premise of the amount of power generated based on the solar radiation data in each season and weather (integrated operation time, 780 hours). Also, as for the solar radiation data, reference was made to the Solar Radiation Database Browsing System[4) published by NEDO to set the solar radiation data that is regarded as the standard in Tsukuba City from June 2011 to December 2012.

As a typical example, **Fig. 4** shows the changes over time in the amount of power generated and the

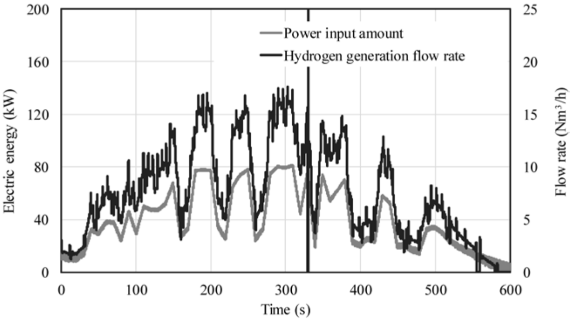

Fig. 4 Changes in electric energy and amount of hydrogen production over time (by pattern of cloudy weather in summer)

amount of hydrogen produced in the solar radiation pattern assuming cloudy weather in summer. It has been confirmed that hydrogen production that follows the power fluctuation is feasible, although the load fluctuation is great, and the conditions are severe for a water-electrolysis hydrogen generator. In addition, the operation was completed without any particular problems during the demonstration period. The change rate of the electrolytic cell voltage, which affects the efficiency, is 1% or less before and after the demonstration period, which is a sufficiently acceptable value from the viewpoint of durability. Also, regarding hydrogen purity, it was confirmed that the concentration of impurities is lower than the allowable impurity concentration, specified by ISO, in the hydrogen fuel for FCV and is suppliable to FCVs.

From the above, it has been confirmed that the newly developed water-electrolysis hydrogen generator has no problem with the fluctuating power source.

2.2 Demonstration operation of hydrogen production and hydrogen refueling to FCVs

The demonstration facility has the following 3 processes assuming actual operation:

(1) Hydrogen production process: The process in which the water-electrolysis hydrogen generator produces hydrogen.

(2) Hydrogen storage process: The process of storing the produced hydrogen in the intermediate accumulator using the intermediate compressor.

(3) Hydrogen supply process: The process of dispensing hydrogen from the intermediate accumulator and supplying it to the hydrogen refueling station in association with hydrogen refueling an FCV with hydrogen.

The hydrogen supply process has been designed so that the water-electrolysis hydrogen and hydrogen supplied from the intermediate accumulator are supplied to the hydrogen refueling station with stable pressure via the low-pressure hydrogen buffer tank.

To confirm the operation as a refueling station of hydrogen based on renewable energy, in which the station is linked with a hydrogen generator, demonstrations have been conducted for the hydrogen production and hydrogen refueling to FCVs. **Fig. 5** shows the test results. It should be noted that, in Fig. 5, the start time of refueling an FCV with hydrogen is set to 0.

Since water-electrolysis hydrogen is introduced into the intermediate accumulator before the start of filling, the pressure of the intermediate accumulator

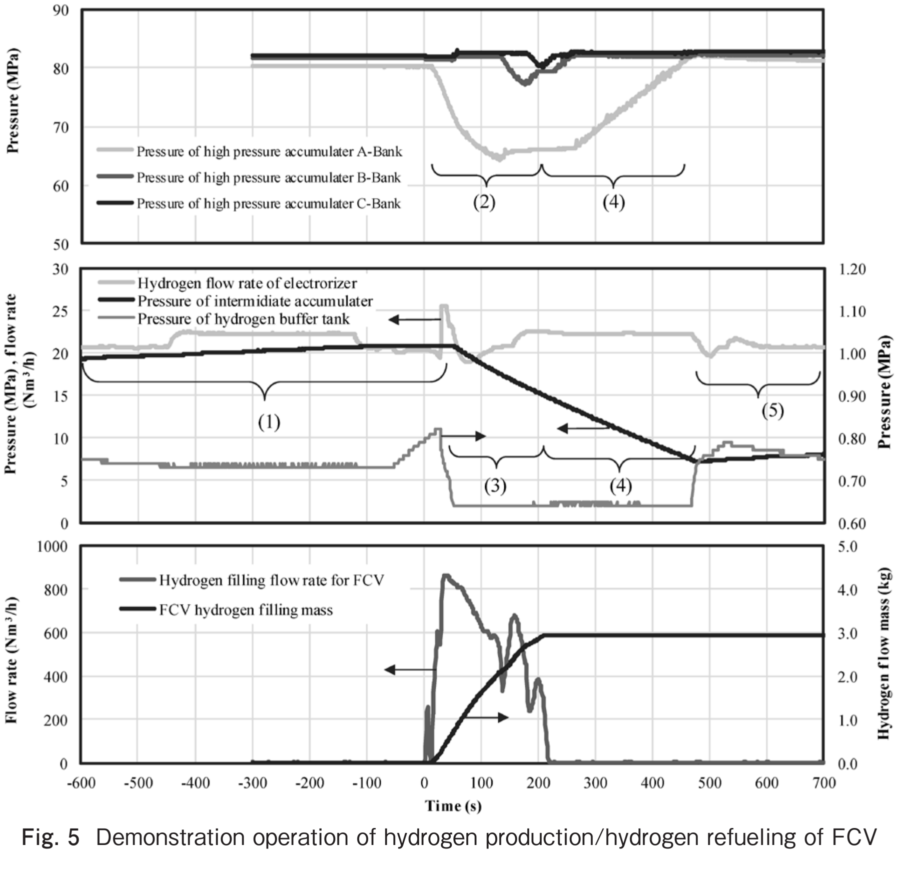

Fig. 5 Demonstration operation of hydrogen production/hydrogen refueling of FCV

increases (Part (1) of Fig. 5). After the filling begins, hydrogen is first supplied from the high-pressure accumulator to the FCV, so the pressure of the high-pressure accumulator decreases (Part (2) of Fig. 5). Next, a start command is sent to the compressor on the side of the hydrogen refueling station, and hydrogen is introduced to the high-pressure accumulator. At the same time, the hydrogen supply process begins, and as a result, the pressure of the intermediate accumulator decreases (Part (3) of Fig. 5). The hydrogen filling completes in 219 seconds, but the compressor continues to operate until the high-pressure accumulator returns to the initial pressure. Thus, the hydrogen supply process goes on. (Part (4) of Fig. 5). As soon as the pressure returns to the initial, the hydrogen supply process is completed, and the hydrogen accumulation process is restarted (Part (5) in Fig. 5).

The following has been confirmed by this demonstration:

- The FCV was filled with 2.9 kg of hydrogen, and approximately the same amount of water-electrolysis hydrogen was supplied from this demonstration facility during that period.
- During the operation, the pressure in the low-pressure hydrogen buffer tank was controlled within the set pressure range.
- The water-electrolysis hydrogen generator was stably producing hydrogen during the series of processes.

As described above, the operation linked with the hydrogen refueling station has been demonstrated.

Conclusions

As a form of refueling stations of hydrogen based on renewable energy, a demonstration facility was designed and built to supply hydrogen produced by a water-electrolysis hydrogen generator with a capacity of 20 Nm^3/h to a hydrogen refueling station. This demonstration facility was used to demonstrate hydrogen production & storage, supply to hydrogen refueling station and filling to an FCV under fluctuating power source.

This demonstration assumed a production and storage facility of hydrogen based on renewable energy, the facility being annex to an existing hydrogen refueling station, i.e., on-site hydrogen production. The application, however, is not limited to this, but possibly includes producing hydrogen by utilizing renewable energy power and/or surplus power, supplying the hydrogen to a trailer or a hydrogen curdle, etc., on a transportation network and thus introducing hydrogen based on renewable energy to the supply network of off-site hydrogen refueling stations.

In the meantime, in order to disseminate hydrogen based on renewable energy, it is necessary to reduce the cost and improve the efficiency of various facilities including water-electrolysis hydrogen generators. In addition, it will be necessary to define hydrogen containing a small amount of CO_2 emissions and to establish the certification system for it.

Kobe Steel will strive to study optimization and cost reduction to contribute to the future of the hydrogen energy society.

This demonstration was conducted with the consignment and assistance from the Ministry of the Environment, "Hydrogen filling station using medium-scale (1.5 kg/h) water electrolyzer powered by renewable energy" under "Low Carbon Technology Research, Development and Demonstration Program, 2016-2017". We would like to express our gratitude here.

References

1) Ministry of Economy, Trade and Industry (METI), Agency for Natural Resources and Energy. Strategic Energy Plan. 2018, https://www.enecho.meti.go.jp/en/category/others/basic_plan/5th/pdf/strategic_energy_plan.pdf, (accessed 2019-12-05).
2) Ministerial Council on Renewable Energy, Hydrogen and Related Issues. Basic Hydrogen Strategy. 2017, https://www.cas.go.jp/jp/seisaku/saisei_energy/pdf/hydrogen_basic_strategy.pdf, (accessed 2019-12-05).
3) Y. Ishii et al., KOBELCO ECO-SOLUTIONS ENGINEERING REPORTS, 2018, Vol.15, No. 1, pp.2-9.
4) NEDO. Solar Radiation Database Browsing System. http://app0.infoc.nedo.go.jp/, (accessed 2019-12-05).

Utilization of Cold Energy in Intermediate Fluid-type Vaporizer (IFV) for LNG Receiving Terminals

Tomohiro SUZUKI[*1] · Shinji EGASHIRA[*1] · Yuji SUMIDA[*2]

[*1] Static Equipment Department, Industrial Machinery Division, Machinery Business
[*2] Industrial Machinery Plant, Industrial Machinery Division, Machinery Business

Abstract

Intermediate fluid-type vaporizers (IFVs), a type of LNG vaporizers, have been used as vaporizers that enable the utilization of the cold energy of LNG in, for example, cryogenic power generation. Recently, there is an increasing number of cold energy utilization projects using chilled water from an IFV for, e.g., the intake air cooling of gas turbines. This paper introduces the latest trends in LNG receiving terminals including offshore receiving terminals, the features of IFVs as LNG vaporizers for cold energy utilization, and examples of cold energy utilization using IFV including gas-turbine-intake air cooling.

Introduction

The demand for natural gas, a clean fuel, is increasing globally. Since many natural gas consumption areas, including Japan, are located far from gas producing areas, natural gas is once transported as liquefied natural gas (hereinafter referred to as LNG) in the cryogenic state (approximately -160 ℃). In consumption areas, LNG is reheated to the ambient temperature and gasified to be used as power generation fuel and city gas.

As a leading manufacturer, Kobe Steel has delivered many LNG vaporizers in Japan and other countries. In recent years, there are increasing inquiries from regions other than the ones for which the company has delivery records, as well as inquiries for projects aiming at the effective utilization of LNG cold energy.

LNG is transported by sea from gas producing areas on large LNG carriers and is unloaded from LNG receiving terminals in each consumption area. The LNG receiving terminals are classified into primary receiving terminals and secondary receiving terminals (satellite terminals). Primary receiving terminals are the first facilities to receive the marine-transported LNG. Secondary receiving terminals are facilities that regasify the LNG land-transported by lorries and the like.

This paper outlines the latest trends of primary receiving terminals and the effective utilization of LNG cold energy using intermediate fluid-type vaporizers (hereinafter referred to as "IFVs") adopted in these primary receiving terminals.

1. Trends of primary LNG-receiving terminals

1.1 Diversification of areas

LNG was formerly received by onshore LNG receiving terminals in Japan, South Korea, Taiwan, former Western European countries, and China. LNG recipient countries, however, have diversified with increasing demand, as a result of the recent shale gas revolution in the United States and global efforts toward CO_2 reduction to prevent global warming, which has increased gas thermal power generation. In recent years the LNG receiving areas have the following characteristics.

- An increase in the construction of LNG receiving terminals in countries that had not previously received LNG, including the Middle East and Latin America areas.
- An increase in construction plans for LNG receiving terminals in Southeast Asian countries such as the Philippines and Myanmar, which used to produce and consume natural gas domestically.

1.2 Diversification in form of LNG receiving terminals

Conventionally, LNG receiving terminals were constructed onshore in coastal areas, and seawater was mainly used as a heat source for vaporizing LNG and raising it to the ambient temperature. In addition, the heat of combustion has been used in cold areas and seasons when the seawater temperature is low. Meanwhile, in countries other than traditional LNG importing countries such as Japan, South Korea, and Taiwan, offshore receiving terminals have started to be built in place of the conventional onshore receiving terminals for the purpose of the prompt introduction of LNG receiving terminals and reduction of construction cost. In addition, the number of offshore terminals is gradually increasing in countries that have newly started receiving LNG.

These offshore LNG receiving terminals take the following two forms.

(1) A Floating Storage Re-gasification Unit (hereinafter referred to as "FSRU")
(2) A Floating Storage Unit + Re-gasification Unit (hereinafter referred to as "FSU +Re-gas")

Many LNG receiving terminals in the above forms have been introduced in developing countries, and as of 2019, twenty-seven FSRU terminals are already in operation. This indicates that FSRUs account for approximately 10% of the gas vaporization capacity, including that of the onshore LNG receiving terminals. As for FSU + Re-gas, three terminals are in operation, and one terminal is to begin operation shortly.1)

1.2.1 FSRU

An FSRU is a form of terminal in which an LNG carrier equipped with vaporization equipment is moored offshore and is used as an LNG receiving terminal. One terminal that has adopted IFV as its LNG vaporizer, there is an FSRU that is run by OLT (Offshore LNG Toscana) off the coast of Livorno, Tuscany, Italy. **Fig. 1** shows the appearance of the FSRU and the appearance of three IFV units mounted as LNG vaporizers. FSRUs have the following three features.

- In addition to the fact that, unlike onshore terminals, no civil engineering work is necessary, there is no need for the onshore construction of an LNG tank, since a carrier equipped with an LNG tank is built at the shipyard. This makes it possible to shorten the construction period and to reduce the construction cost.
- Since the terminal itself is a ship, it can be moved by ship and used in other places in the future.
- An offshore terminal restricts the utilization of LNG cold energy to shipboard. There is, however, no utilization application on board so far, and no LNG cold energy has been utilized effectively.

The main LNG vaporization processes in current FSRUs occurs in shell-and-tube type vaporizers. This type of vaporizer uses ethylene glycol water warmed by the heat of seawater to exchange heat with LNG, and many terminals employ this type of LNG vaporizer.

1.2.2 FSU + Re-gas

An FSU + Re-gas is a form of terminal in which the regasification equipment in FSRU is built onshore or on a fixed platform to be used as an LNG receiving terminal. One terminal in the form of FSU + Re-gas whose IFV is adapted as an LNG vaporizer is a gas turbine combined cycle (hereinafter referred to as "GTCC") run by ElectroGas Malta (EGM) in the Republic of Malta. The appearance of the FSU + Re-gas and GTCC is shown in **Fig. 2**. The features of an

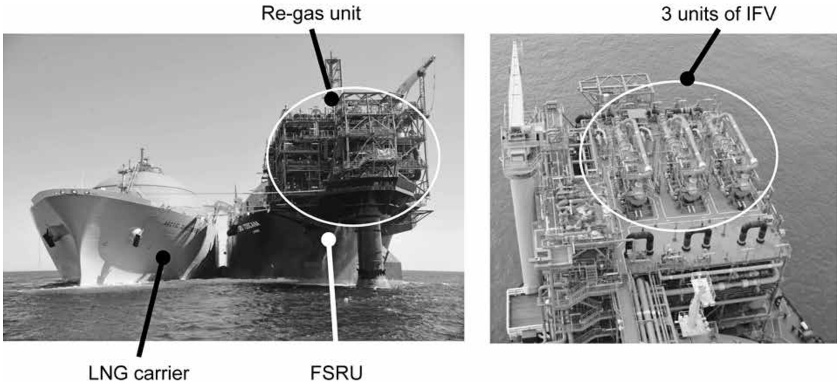

Fig. 1 FSRU and LNG carrier (left), and IFVs on FSRU (right) by OLT of Italy (photo courtesy of Offshore LNG Toscana)

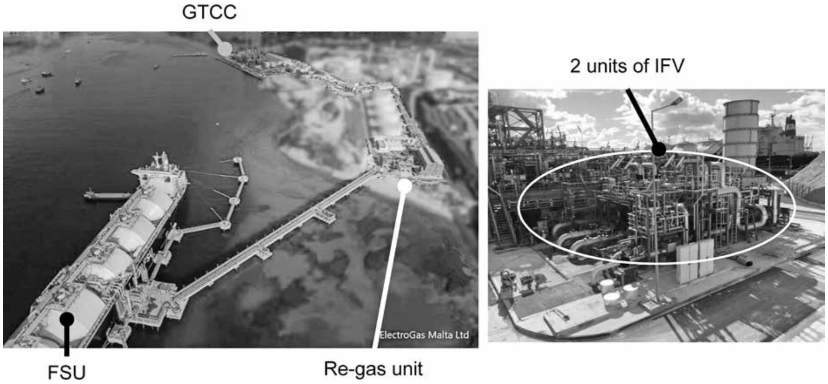

Fig. 2 FSU and power plant (left), and IFVs on re-gas unit (right) by EGM of Malta (photo courtesy of ElectroGas Malta Ltd.)

FSU + Re-gas terminal are as follows.

- Similar to FSRUs, the construction of LNG tanks, which account for most of the construction period/time and cost of onshore terminals, is no longer required, which can shorten construction periods.
- The regasification equipment is built onshore instead of onboard, allowing the use of a secondhand LNG carrier, which is a normal practice for FSUs. This expands the choices for shipping companies placing orders, in comparison with FSRU.
- Unlike FSRUs, many of which are based on fixed-term lease contracts, regasification equipment can be owned by a group or by a local government as infrastructure.
- The onshore construction of regasification equipment facilitates the effective utilization of LNG cold energy, as in the case of onshore primary receiving terminals.

2. Construction and features of LNG vaporizers for primary receiving terminals

2.1 Overview of LNG vaporizers

LNG vaporizers commonly used in onshore LNG receiving terminals include open rack vaporizers (hereinafter referred to as ORVs), IFVs, and submerged combustion vaporizers (hereinafter referred to as SCVs). ORVs and IFVs are LNG vaporizers using seawater as their heat source. An SCV is a backup vaporizer that is used only when and where the seawater temperature is too low to be used as the heat source. It is configured to vaporize LNG by the heat of the combustion of fuel with an underwater burner and requires consideration of environmental regulations and the like for the combustion exhaust gas.[2)]

Among these LNG vaporizers, IFVs have many introduction records for LNG cold energy utilization.

2.2 IFV

2.2.1 Overview of IFV configuration and vaporization process

An IFV is a vaporizer that utilizes heat sources such as seawater to vaporize LNG through a heating fluid such as propane. It was developed by Osaka Gas Co., Ltd. in the 1970s under the name of TRI-EX and consists of three components; namely, intermediate fluid evaporator (hereinafter referred to as E-1), an LNG vaporizer (hereinafter referred to as E-2), and an NG heater (hereinafter referred to as E-3).

Fig. 3 shows the schematic diagram of an IFV. The LNG supplied into the heat-transfer tube of E-2 undergoes heat exchange with the intermediate fluid gas in the upper part of the E-1 shell. Almost all the LNG is vaporized and then transferred to the E-3 shell side through a connecting piping. At E-3, the natural gas is heated by heat-exchange with seawater flowing in the heat transfer tube and is sent out as gas at the ambient temperature. On the other hand, the intermediate fluid, condensed by heat-exchange with LNG on the outer surface of the heat transfer tube, E-2, drops to the bottom in the E-1 shell to exchange heat with the seawater flowing in the heat transfer tube and then is vaporized as intermediate fluid gas to vaporize LNG in the E-2 tube again.

Propane is mainly used for the intermediate fluid. As an option for customers who have concerns about using propane, a flammable gas, as the intermediate fluid in limited spaces, as is the case

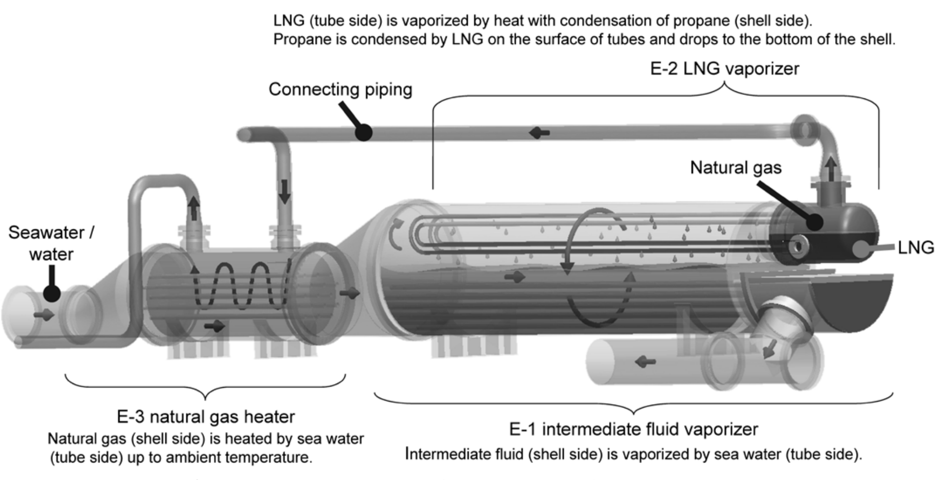

LNG (tube side) is vaporized by heat with condensation of propane (shell side).
Propane is condensed by LNG on the surface of tubes and drops to the bottom of the shell.

Natural gas (shell side) is heated by sea water (tube side) up to ambient temperature.

Intermediate fluid (shell side) is vaporized by sea water (tube side).

Fig. 3 Schematic diagram of intermediate fluid vaporizer (IFV) in an FSRU, it is suggested to use a non-flammable heat medium as an alternative.3)

Titanium alloy is used for the heat transfer tubes (transfer tubes E-1 and E-3 heat) through which seawater flows to assure extremely high seawater corrosion resistance.

2.2.2 Characteristics of IFV

The characteristics of an IFV as an LNG vaporizer are as follows:

(1) The running cost is low since the heat source is mainly seawater.
(2) The heat exchange is performed between LNG and heat source fluid via an intermediate fluid with a low freezing point, which avoids problems such as channel blockage due to freezing of the heat source fluid.
(3) The use of titanium alloy as the material of the heat transfer tube prevents the occurrence of erosion and corrosion even if seawater of poor quality is used as the heat source.
(4) The intermediate fluid and cooled heat-source fluid after heat exchange can be applied to cold energy utilization.

One embodiment of the application to cold energy utilization in (4) above is the LNG cryogenic power generation system that utilizes propane as the intermediate fluid. This was developed for the purpose of saving energy in an LNG receiving terminal and has been actively introduced mainly in the LNG receiving terminals of gas companies at various locations in Japan since the 1970s. The appearance and process outline of the cryogenic power generation plant are shown in **Fig. 4** and **Fig. 5**, respectively. These cryogenic power generation plants are still in operation, including the one operated by Osaka Gas Co., Ltd.

A decision was made in the late 2010s to introduce cryogenic power generation systems using Kobe Steel's IFVs in an update project for a terminal in Japan and an LNG terminal in Shanghai, China.

3. Utilization of LNG cold energy by IFVs

As described in Section 2.2, an increasing number of projects are considering IFVs as LNG vaporizers to utilize the cold energy of LNG. This section describes LNG cold energy utilization using IFVs that are already running at LNG receiving terminals.

3.1 Overview of LNG cold energy utilization

LNG is a cryogenic fluid of approximately -160 ℃, and its cold energy has been disposed of in seawater after heat exchange without being effectively utilized. Hence, the owners of LNG receiving terminals have been working on the effective utilization of LNG cold energy from the economic aspect of terminal operation and from the aspect of CO_2 reduction.

Fig. 4 Appearance of LNG cryogenic power generation plant in Osaka Gas Co., Ltd.

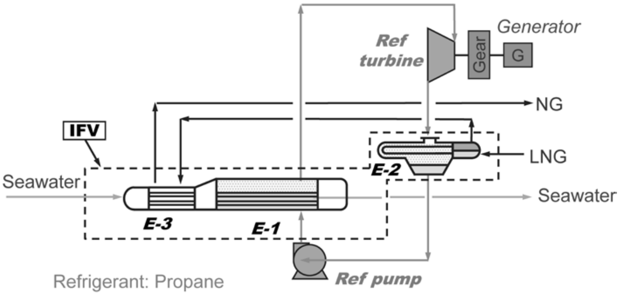

Fig. 5 Schematic diagram of process flow for LNG cryogenic power generation system (Rankine cycle)

The following applications are considered for the cold energy utilization of LNG in LNG receiving terminals:

(1) LNG cold energy power generation systems.
(2) Utilization in dry-ice production, freezer warehouses, etc.
(3) Cooling systems for gas turbine intake air.
(4) The supply of cold energy to cooling equipment used in plant factories and data centers.

Applications (1) and (2) above have long been adapted to LNG receiving terminals, mainly by gas companies in Japan. The following sections outline (3) and (4), which are increasingly being introduced in the LNG receiving terminals in subtropical areas such as Southeast Asia.

3.2 Utilization of LNG cold energy for cooling gas-turbine intake air

In an IFV, a heat source fluid such as seawater flows through its pipes. Therefore, it is possible to reciprocally circulate the heat source with one heat-source circulation pump between an LNG vaporizer and the destination of cold energy utilization. In an ORV, on the other hand, seawater flows down on the outer surface of a heat transfer tube from the upper part of the heat exchanger body, open to the ambient air, to perform heat exchange. For this reason, two heat-source circulation pumps are required for the supply to the ORV and for delivery to the destination of cold energy utilization. In addition, since the ambient air is encountered during the flow-down on the heat transfer tubes, it is necessary to control foreign matter and water quality. In this sense, an IFV is regarded as more effective for the cold energy utilization of the heat source circulation type.

3.2.1 Intake air cooling of gas turbines

A gas turbine mixes compressed intake air with fuel in its combustor and burns the mixture to utilize the pressure of the combustion gas for rotating the generator to generate electricity. The temperature of the air taken in by a compressor is specified to be 15 ℃ by the ISO standard, and the rated output is also designed at the atmospheric temperature of 15 ℃.

In hot and humid subtropical areas, there are many places where the temperature becomes higher than 15 ℃ throughout the year. In those areas, the mass of air sent to the combustor of a gas turbine decreases due to the decrease in air density. As a result, the power generated by the gas turbine becomes lower and the power generation decreases. If air at 35 ℃ is cooled down to 15 ℃, for example, the air density increases by 10%, and the power generation increases by 10%. For these reasons, there is a significant economic benefit in working on the cooling of gas turbine intake air in hot and humid subtropical areas.

There are several types of intake air cooling. Among them, the most efficient type directly cools the intake air with chilled water. In other words, it is a type in which chilled water is supplied to the intake air cooling coil incorporated in the intake air filter chamber, such that direct heat exchange is performed with the intake air to lower the intake air temperature to 15 ℃ or below. **Fig. 6** shows a schematic diagram of the process flow of intake air cooling in a gas turbine using an IFV. One of the embodiments of gas-turbine intake-air cooling is found in GTCCs in Southeast Asia, to give one example. At these power plants, chilled water is supplied from a turbo chiller using electric power to perform the intake air cooling of gas turbines to improve power generation efficiency.[4)]

In the LNG receiving terminals that have recently been constructed in Southeast Asia, and other such areas, there are an increasing number of projects called "Gas-to-Power," in which an LNG receiving terminal and GTCC are constructed together. These projects are suitable for the intake air cooling of gas turbines utilizing LNG cold energy for the following reasons:

- They are mostly in high temperature areas where the temperature exceeds 15 ℃ throughout the year.
- The distance between the LNG receiving terminal and GTCC is short, facilitating the transfer of the heating fluid.
- Because the business entity of the LNG receiving terminal and the business entity of the gas thermal power plant are often the same, it is easy to make investment decisions because there is no conflict between the operational aspect and the interests of economic benefit.

3.2.2 Advantages of IFV in intake air cooling system

Two types of LNG vaporizers have been installed

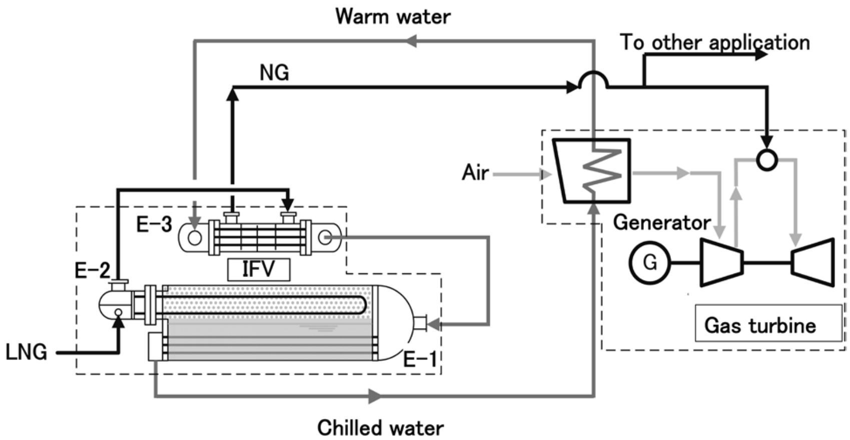

Fig. 6 Schematic diagram of process flow for cooling intake air of gas turbine using IFV

in gas turbine intake air cooling systems utilizing LNG cold energy, namely, shell-and-tube LNG vaporizers (hereinafter referred to as "STVs") using ethylene glycol as the circulating heat source,[5)] and IFVs using industrial water as the circulating heat source.[2)] STVs have been introduced to several systems in Caribbean countries, and IFVs have been introduced to systems in the Republic of Malta and the Kingdom of Thailand, in addition to Japan. The advantages of the system using IFV are as follows:

- The temperature of the heat source required for the intake of an air-cooling system is approximately 5 ℃, which is within the temperature range where even the industrial water used by an IFV as its circulating heat source does not freeze. This keeps the systems running.
- In an STV, direct heat exchange occurs between LNG and the circulating heat source. Therefore, industrial water at 5 ℃ is likely to freeze, making the STV's adoption difficult. An IFV, on the other hand, uses intermediate fluid for the LNG vaporization process and can be operated without concern about freezing even if industrial water of 5 ℃ is used as the circulating heat source.
- The circulating heat source of an IFV can be industrial water, which is less expensive to prepare than glycol water. The circulating heat source is often utilized simultaneously by applications other than the gas turbine intake air cooling. In these applications, if a storage tank for temperature adjustment is required, the difference in filling cost between water and glycol water will be even greater.
- Glycol water, which is corrosive to the pipes, requires water quality management, but industrial water basically requires no water quality management.

Thanks to the advantages of IFVs as described above, there are an increasing number of LNG vaporizer projects adapting IFVs that use industrial water as their circulating heat source.

From the viewpoint of energy saving, the following effects can be expected for intake air cooling using IFVs:

- If an IFV has an LNG flow rate capacity of 100 tonnes/hour, it has a cooling capacity of approximately 20,000 kW, and the consumption energy (or the power of water circulation pump) required to supply cold energy to the IFV is approximately 700 kW. On the other hand, a turbo refrigeration system with the same cooling capacity consumes approximately 4,200 kW (refrigerator power, cooling tower fan power and water circulation pump power) of energy and, thus, a greater economic effect is achieved by LNG cold energy utilization using an IFV.

The total power generation at the terminal in the Republic of Malta, shown in Fig. 2, is 150 MW. The output recovery effect of the gas turbine in summer is 6%, and an effect of 9 MW has been confirmed to be obtained by cold energy utilization of an LNG. In this terminal, cooling water sent to the compressor for boil-off gas is supplied from an IFV in addition to the gas turbine intake air cooling.[6)]

In the case of a gas-to-power terminal, the amount of LNG for generating the chilled water required for the intake air cooling of the gas turbine is approximately 3 times the amount of gas (natural gas vaporized from LNG) sent from the LNG vaporizer (assuming an inlet air temperature of 35 ℃ and an outlet temperature of approximately 15 ℃). This means that there are cases where the output recovery by intake air cooling may not be sufficient when the entire amount of gas vaporized by the LNG vaporizer is consumed by the gas turbine. As a result, the gas may often be sent, not only to the gas turbine, but also to the gas conduit and other parts.

When the above utilization environment is in place and the cold energy of LNG is utilized for the intake air cooling of the gas turbine, the maximum amount of energy that can be obtained from 1 tonne of LNG is 180 kWh. This offers a significant advantage in utilization efficiency over the 23 kWh/tonne for the cryogenic power generation system (propane Rankine cycle type) described in Section 2.2.

3.3 Other types of LNG cold energy utilization using IFVs

Other than gas turbine intake air cooling systems, IFVs have been utilized for chilled water supply to large cooling systems such as those for plant-cultivation factories. The methods used for supplying chilled water from IFVs include the following:

(1) Cases where chilled water is directly supplied as a circulating heat source to the utilizer as in the case of gas turbine intake air cooling.
An LNG receiving terminal in the Kingdom of Thailand utilizes the chilled water directly supplied from IFV to the cooling of a cultivation factory for plants such as tulips, together with the intake air cooling of the gas turbine installed in the LNG receiving terminal.

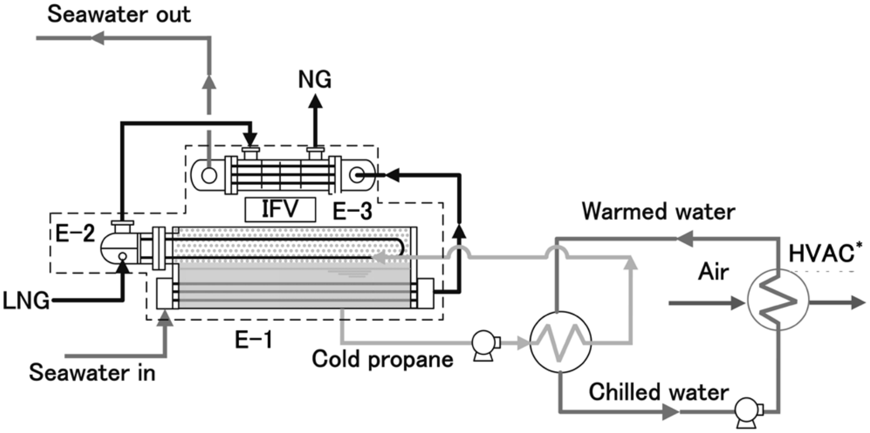

*Heating, Ventilation, and Air Conditioning

Fig. 7 Process flow of IFV for supplying cold energy to air conditioning apparatus

Fig. 8 Appearance of IFV for supplying cold energy to air conditioning apparatus in Kagoshima Terminal of NIPPON GAS Co., Ltd.

(2) Cases where propane (liquid) cooled by cold energy of LNG in E-1 of an IFV is extracted by a circulation pump, and the propane liquid is heat-exchanged with circulating water to be indirectly supplied to the destination where the cold energy is utilized.

In this case, the normal operation is to circulate propane while utilizing seawater as a vaporization heat source. Therefore, this has the advantage that gas can be sent to the conduit without being affected by the operational situation of the destination of cold energy utilization.

The system overview and IFV appearance for such a case are shown in **Fig. 7** and **Fig. 8**, respectively. In the terminal shown in Fig. 8, an IFV sends intermediate fluid in a liquid state at 3 ℃ to a heat exchanger to turn the circulating water into cooling water of 8 ℃. This cooling water is circulated between the fan coil unit (FCU) in a fully artificial light-type plant factory and utilized for cooling air conditioning. The temperature in the plant factory is kept at 18 to 25 ℃.[7] A fully artificial light-type plant factory has high operational costs, for utilities, as an example; however, the utilization of LNG cold energy is reported to reduce the cost by approximately 40%.

Conclusions

This paper has outlined the latest trends of primary LNG-receiving terminals, the characteristics of IFVs, and LNG cold energy utilization using IFVs.

Kobe Steel has been developing and proposing LNG vaporizer systems optimal for developing LNG vaporizers in accordance with diversification in the forms of LNG receiving terminals and for improving the efficiency of cold energy utilization in the LNG receiving terminals. We will continue to develop this technology and maintain our position as the world's top manufacturer of LNG vaporizers.

References

1) IGU 2019 WORLD LNG REPORT
2) S. Egashira. *R&D Kobe Steel Engineering Reports*. 2013, Vol.63, No.2, pp.33-36.
3) K. Higashi et al. ICE2019-25th IIR International Congress of Refrigeration. Montreal, 2019, pp.437-444.
4) T. Komuro et al. Mitsubishi Heavy Industries Technical Review. 2010, Vol.47, No.4, pp.49-54.
5) A. Bulte. Integration of CCGT Plant and LNG Terminal. 2008, 19th WORLD PETROLIUM CNGRESS, Madrid.
6) J. L. Maseda et al. LNG to power in islands. Maltacase with the FSU terminal of Delimala. https://www.gti.energy/wp-content/uploads/2019/10/94-LNG19-03April2019-Losada-Maseda-Jes%C3%BAs-poster.pdf,(accessed 2019-12-06).
7) K. Himono. Utilization of LNG cold energy for plant factory air conditioning (control method). Gas Energy News, December 18, 2017.

Expanding Application of Micro Channel Equipment (Diffusion Bonded Compact Heat Exchanger; DCHE™)

Yasutake MIWA[*1] · Masataka AZUMA[*1] · Dr. Koji NOISHIKI[*1]

[*1] Static Equipment Department, Industrial Machinery Division, Machinery Business

Abstract

The demand for microchannel heat exchangers, a type of compact heat exchanger, is expected to increase as they are used in applications requiring light weight and compactness and as apparatuses for offshore equipment. Above all, their demand has been increasing in recent years for use in the fuel supply systems of offshore equipment that uses liquefied natural gas (LNG) and small-capacity LNG vaporizers for satellite bases.

These applications require, not only pressure tightness and compactness, but also measures to be taken against the freezing of the fluid serving as the heat medium. In the case of diffusion bonded compact heat exchangers (DCHE™s), concepts having to do with the suppression of freezing have been incorporated into their design, and tests were conducted using liquid nitrogen and LNG, to establish the design guidelines for the range of vaporization performance and icing. This report introduces the effort to apply a DCHE™ to LNG vaporizer applications.

Introduction

Microchannel heat exchangers, or diffusion bonded compact heat exchangers (hereinafter referred to as the "DCHE™"),[Note 1] have high pressure resistance and are used as compressed gas coolers for natural gas processing plants, heat exchangers for natural gas fluids, as well as for coolers and precoolers of compressed hydrogen for hydrogen refueling stations. With the requirements for improving equipment reliability and for compactness, studies are taking place to use the DCHE™ for LNG vaporizers and natural gas processing plants in the future.

This paper mainly introduces the characteristics of the DCHE™ from aspect of its design for LNG vaporizer applications.

1. Structure and characteristics of DCHE™

1.1 Structure of DCHE™

The DCHE™ is a type of compact heat exchanger and has a structure consisting of stacked plates with millimeter-sized channels. Kobe Steel has the designing and manufacturing technology of brazed aluminum plate-fin heat exchangers (hereinafter referred to as the "ALEX™"[Note 2]), which have been delivered for more than 50 years, and the DCHE™ exploits this technology. An ALEX™ comprises a brazed core body for exchanging heat, and a header and nozzle for guiding the fluid into the core (**Fig. 1**).1) The DCHE™ has a stacked structure like the ALEX™, and the manufacturing know-how and design concept cultivated for the ALEX™ can be applied to the DCHE™.2) The greatest differences in the manufacturing process are found in the processes of etching to form channels, and diffusion bonding to join the plates all at once. Etching is a technology for melting and processing metals by utilizing the corrosive action of chemicals such as etching solutions. This technique is applied to stainless steel plates to form channels through which fluid passes. Since the DCHE™ applies diffusion bonding, it has a pressure resistance higher than those of other heat exchangers.

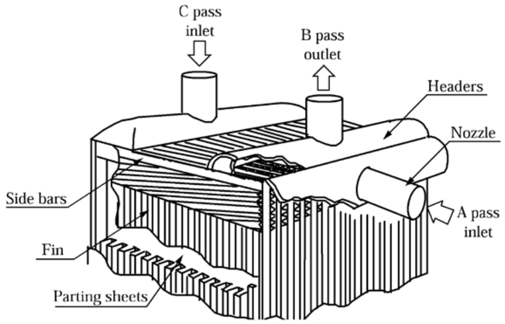

Fig. 1 Structure of ALEX™

1.2 Characteristics of DCHE™

The DCHE™ has the following basic characteristics:

(1) Performance highly resistant against pressure and heat
By selecting material and optimizing channel size, it can be used up to 100 MPa and 900℃. The applicable temperature range follows the allowable stress table stipulated by the law for each material.

[Note 1] DCHE is a registered trademark of Kobe Steel, Ltd.

[Note 2] ALEX is a registered trademark of Kobe Steel, Ltd.

(2) Compactness
Its large heat-transfer area ensures high heat-transfer performance, making its size approximately 1/10 of those of multi-tube (shell & tube) heat exchangers.

(3) Excellent corrosion resistance
The use of SS316L and the like enables its application to cooling water, etc.

It should be noted, however, that the ALEX™ is more economical, and the ALEX™ is proposed for applications where it is applicable, e.g., where the temperature difference between fluids is smaller than 50℃ (single phase), the application is not corrosive, and the pressure resistance requirement is 13 MPa or lower.

Kobe Steel handles both the DCHE™ and ALEX™, each being a type of compact heat exchanger, and can propose an optimum heat exchanger in accordance with the design and operating conditions. Kobe Steel also has performed numerous stress analyses on various static equipment such as heat exchangers and pressure vessels. Therefore, in the case of operations with a large temperature difference between fluids, or with a significant operating variation that causes concerns about damage during operation, it is also possible to predict the expected lifetime of heat exchangers by using the finite element method of analysis (hereinafter referred to as "FEM analysis").

1.3 Applicable use of DCHE™

As described above, the DCHE™ is a compact heat exchanger with excellent heat transfer performance. For this reason, it is used, for example, for offshore equipment with footprint limitations and coolers for hydrogen refueling stations. It is also adapted to cases where the ALEX™ cannot be used, e.g., coolers using cooling water for natural gas or hydrogen gas and LNG vaporizer applications with a large temperature difference between fluids of 50℃ or greater.

The recent increase in shale gas production in the United States has initiated several projects, not only for onshore natural gas plants, but also for offshore floating production storage and offloading (FPSO) systems for oil and gas as well as natural gas liquefaction processing facilities (Floating LNG),3), 4) in which the DCHE™ is often applied to heat exchangers of the natural gas fluid and after-gas coolers of compressors. Also expected as offshore applications are LNG vaporizers used in the fuel supply systems of LNG fueled ships (Fuel Gas Supply Systems: FGSSs).

In these applications, natural gas is expected to be increasingly used as an environmentally friendly fuel, with emissions of carbon dioxide, sulfur oxides and nitrogen oxides lower than those of coal and petroleum, to comply with the new limit on sulfur content stipulated by the International Maritime Organization (IMO)5) and to meet the 2025 regulations on CO_2 emissions.6) In addition, the DCHE™ is expected to be applied to offshore facilities with limitations in footprint area, requiring equipment down-sizing.

As for onshore applications, the demand for natural gas supply systems using LNG satellite terminals[Note 3] for industrial use is on the rise.7) From the perspective of achieving global warming countermeasure goals, there are high expectations in Japan, the United States, Europe, and Asia for hydrogen as a means of storing increasing renewable energy in large quantities over medium-to-long terms, and the construction of hydrogen refueling stations is in progress with the prevalence of fuel cell vehicles (FCVs).8)-10) The DCHE™ has been applied to the aftercoolers of compressed hydrogen and precoolers for dispensers used there.

The following sections describe the details of Kobe Steel's unique design concept and the approach of the DCHE™ in the natural gas vaporizer applications used in the fuel supply systems for offshore and satellite terminals, whose demand is increasing in recent years.

2. Antifreezing structure

Besides compactness, it is important for LNG vaporizer applications to prevent hot water and glycol water used as a heat source, from being frozen in the channel inside a heat exchanger by the cold heat of LNG, so as to keep the operation running continuously. For other types of heat exchangers, such as multi-tube heat exchangers, it is recognized as one of the problems that, when freezing occurs, it is necessary to stop the operation of the LNG vaporizer until the ice is thawed. Hence, Kobe Steel has incorporated a unique concept into its design and applied a structure that is less likely to cause freezing to the LNG vaporizer applications. This section provides an overview.

2.1 Concept 1: Stacked structure11)

In the case of LNG vaporizer applications, the conventional concept involves two-fluid heat

---

[Note 3] A secondary receiving terminal that accepts and regassifies LNG carried from a primary receiving terminal by a lorry, or the like exchange between LNG, which is the COLD side fluid, and the HOT side fluid, and the design is conducted with the number of layers based on COLD: HOT = 1: 1. In this structure, however, if the fluid in the channel on the HOT side is plugged by freezing, it is necessary to wait until it naturally thaws. On the other hand, by applying the COLD: HOT = 1: 3 structure including two HOT1 layers and one HOT2 layer against one COLD side layer as shown in **Fig. 2**, it is possible to supply the heat of HOT2 to HOT1, even if freezing begins to occur in the layer of HOT1, which is in contact with the COLD side. Thus, it is possible to suppress the freezing of the HOT side fluid that obstructs the channel, unlike the conventional COLD: HOT = 1: 1 structure. Hereinafter, the combination of COLD: HOT = 1: 1 is referred to as the 1: 1 structure, and the combination of COLD: HOT = 1: 3 is referred to as the 1: 3 structure.

2.2 Concept 2: LNG channel pattern design

When LNG is supplied at a low pressure, there is created a region where LNG is evaporated inside a heat exchanger. Therefore, it is predicted that the temperature of the metal (the wall temperature of channels) of the heat exchanger will decrease due to the latent heat and the increase in the heat transfer coefficient on the LNG side. To mitigate this, a channel type (straight channel) with poor heat transfer is intentionally adopted in the part where the heat transfer coefficient is high in the LNG vaporization region. In addition, in order to reduce the heat-transfer area in the LNG evaporation region, a channel design with a large pitch is adopted for the LNG channels.

Meanwhile, on the heat medium side, a channel type with a high heat transfer coefficient (wavy channels) and a channel type with a small pitch are adopted so that a large heat-transfer area can be obtained for the sake of raising the temperature of the metal of/in the heat exchanger.

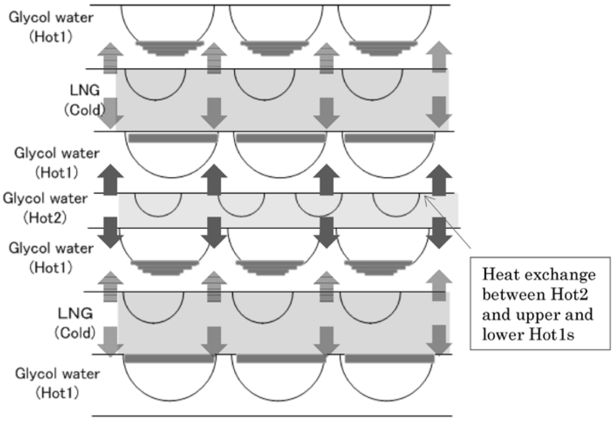

Fig. 2 Concept of antifreezing

3. Performance test using liquid nitrogen (LN_2) and LNG

The effectiveness of the antifreezing structure described in the previous section was examined by investigating the changes in the LNG outlet temperature and the pressure loss of the fluid on the HOT side, while confirming the performance of the equipment and the freezing conditions of the fluid in the channels. This section provides an overview.

3.1 Test with high pressure LN_2

3.1.1 Confirmation test of vaporization performance range

Two DCHEs™, one with the 1: 1 structure and the other with the 1: 3 structure, were prepared to confirm their operable ranges while using the parameters of LN_2 inlet temperature, LN_2 flow rate, etc. for both of the structures. The heat medium used for the test was 40 vol% propylene glycol water with a freezing temperature of -22℃. **Fig. 3** shows the results of the confirmation test performed on the range for vaporizing performance. First, a test was carried out at an inlet temperature of 60℃ and a flow rate of 32.5 m^3/h for propylene glycol water, and a flow rate of 1,500 kg/h for LN_2. The results confirmed that the LNG outlet temperature satisfies the specified temperature without freezing for both the 1: 1 structure and 1: 3 structure.

Next, the operation range in which freezing occurs was confirmed by increasing the LN_2 flow rate stepwise to 2,000 kg/h, 2,500 kg/h, and 3,000 kg/h while keeping the flow rate of propylene glycol water constant (32.5 m^3/h) and decreasing the inlet temperature stepwise from 60℃ to 50℃, 40℃ and 30℃. As a result, the 1: 1 structure used

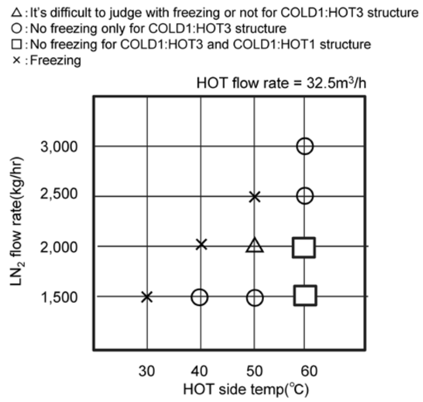

Fig. 3 Test results of range for vaporizing performance

in conventional design exhibited a decrease in heat transfer performance and an increase in pressure loss on the heat source side, which are considered to be attributable to freezing, for all the conditions at the propylene glycol water inlet temperature of 60℃, flow rate of 2,000 kg/h or higher, and inlet temperature of 50℃ or below. On the other hand, the 1: 3 structure caused no freezing in all the conditions indicated by the circles (○), confirming that it can handle a wider range of operating conditions than the 1: 1 structure can.

3.1.2 Confirmation tests on performance of recovery from freezing

After the above test, a test was carried out to confirm the performance of the recovery of the heat source fluid from freezing. The test results are graphed in **Fig. 4**, the change in flow rate is graphed in **Fig. 5**, and the change in pressure loss is graphed in **Fig. 6**. The testing conditions were as follows:

First, a test was conducted under the conditions of an LN_2 inlet temperature of 60℃ and the flow rate of 3,000 kg/h. Then, the LN_2 inlet temperature was changed to 50℃ to confirm that freezing occurred in the fluid in the HOT side channel by checking the change in the pressure loss on the basis of the HOT side inlet and outlet pressures. From here, the flow rate was decreased to confirm whether the freezing would be reversed. As described in the graph, the flow rates were set to 1,200 kg/h, 750 kg/h, and 500 kg/h. The freezing was judged to have recovered when the pressure loss based on the inlet and outlet pressures on the HOT side decreased to their pre-freezing level under the conditions reduced to 750 kg/h and 500 kg/h. In other words, it was confirmed that, in the case of the 1: 3 structure, lowering the flow rate on the COLD side is effective for performance of recovery even when the fluid in the channel on the HOT side is frozen. Alternatively, when HOT2 is managed as a separate fluid, freezing can be reversed by increasing the temperature of the HOT2 side fluid or by increasing its flow rate.

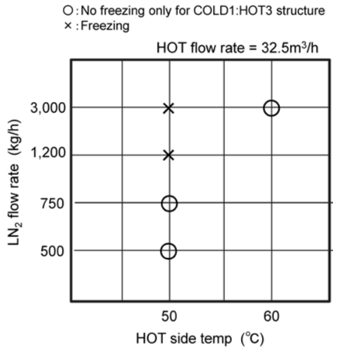

Fig. 4 Test results for performance of recovery from freezing condition

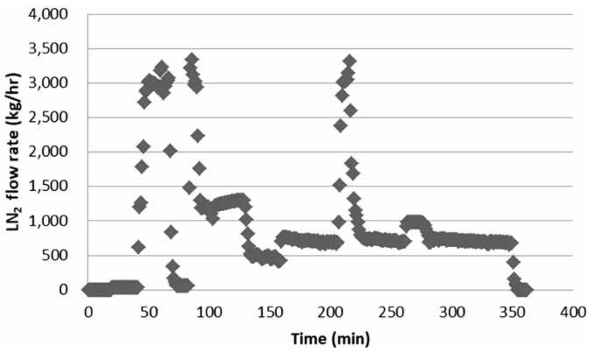

Fig. 5 Test results for performance of recovery from freezing condition (LN_2 Flow rate)

3.2 Test with low pressure LNG

3.2.1 Confirmation test on heat exchanger performance

Using low-pressure LNG, a test was conducted under conditions where an LNG vaporization region occurs inside the equipment. **Table 1** shows the test conditions. In addition to Concept 1 described in Section 2, the DCHE^{TM} adopting the structure of Concept 2 was used, and the effectiveness of these against freezing was confirmed in test conditions ① and ② shown in Table 1. The performance evaluation of the heat exchangers was conducted by comparing the designed *UA*, in which *UA* is the product of the overall heat transfer coefficient (*U*) representing the performance of the heat exchanger

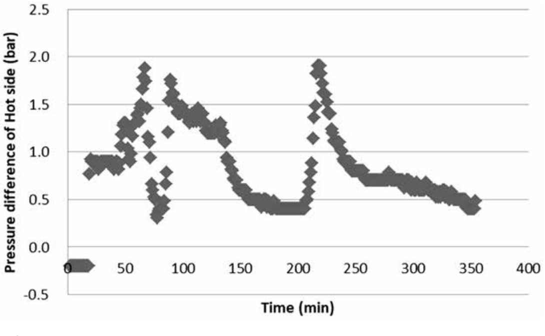

Fig. 6 Test results for performance of recovery from freezing condition (pressure difference on HOT side)

Table 1 Test condition of heat exchanger performance

	LNG side	Hot water side
Pressure	6.5 barg	2.0 barg
Flow rate	123.5 kg/h	9,753 kg/h
Inlet temperature	-125℃	①50℃ (design case) ②40℃ (critical case for freezing) ③30℃ (freezing condition)

and the heat-transfer area (A), with the UA of the actual device. The value UA is obtained by dividing Eq. (1), which expresses the heat exchange amount Q, by ΔT obtained from the process conditions. It is known that this is effective for evaluating heat exchangers when the flow rates of the fluids and their physical properties are close to each other.[12)]

$$Q=UA\Delta T \quad \cdots\cdots (1)$$

wherein Q: Amount of heat exchanged (kW)
U: Overall heat transfer coefficient (kW/m^2℃)
A: Heat-transfer area (m^2)
ΔT: Logarithmic mean temperature difference (℃)

As shown in **Table 2**, conditions ① and ② both yielded results exceeding the respective values of designed conditions, confirming that there was no problem with the performance of the heat exchanger.

3.2.2 Establishment of design guidelines against freezing

Continuing from the previous section, a test was conducted under test conditions ③, shown in Table 1. The freezing conditions were confirmed by the low-pressure LNG test and were compared with the wall temperature profile, obtained by the design calculation of Kobe Steel, inside the heat exchanger. As a result, the relationship between the design-calculation wall temperature and the freezing range was determined as shown in **Fig. 7**. These results confirmed that there was a difference between the design-calculation wall temperature and the freezing point of the fluid on the HOT side. The difference is considered to be due to the changes in flow rate and temperature, which occur even in normal operation, and the design margin has been determined from these values and used as the design guideline.

Table 2 Test results for heat exchanger performance

	Design condition	Test condition ① Inlet temperature: 50℃	Test condition ② Inlet temperature: 40℃
Heat exchanged amount (kW)	26.6	19.53	20.15
Long mean temperature difference (℃)	116.8	48.1	49.7
UA (kW/℃)	0.228	0.406	0.405
Comparison between design condition and test results	100%	178%	178%

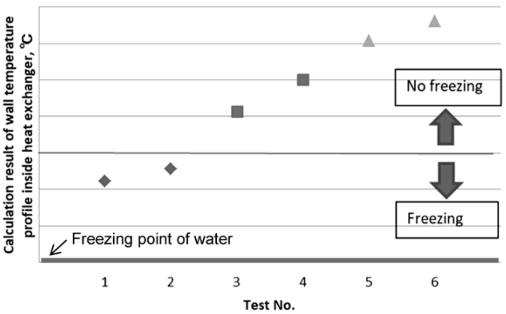

Test No.	Hot side in temp (℃)	LNG in temp (℃)
1	30	−129
2	30	−125
3	40	−129
4	40	−125
5	50	−129
6	50	−125

Fig. 7 Calculation results for wall temperature profile inside heat exchanger under each test condition

4. Verification of measures against thermal stress

LNG vaporizer applications inevitably accompany a significant temperature difference between LNG and the HOT-side fluid, which causes great thermal stress to be generated. Studies were conducted on how much thermal stress is generated, how to evaluate design life and how to reduce thermal stress.

4.1 Thermal stress evaluation by thermal stress analysis

The evaluation of thermal stress was based on confirming how many times the start and stop can be allowed under the following design conditions. The thermal stress was calculated using the FEM analysis, and the design life was derived from the design fatigue curve (**Fig. 8**) of austenitic stainless steel, as described in ASME Sec. VIII Div.2.

4.2 Evaluation of number of start/stop times in actual project

Thermal stress evaluation was carried out under the design conditions shown in **Table 3**. The resulting stress contour map is shown in **Fig. 9**. From Fig. 9, it has been found that the largest thermal stress is generated on the LNG header side of the weld between the HOT side header and core

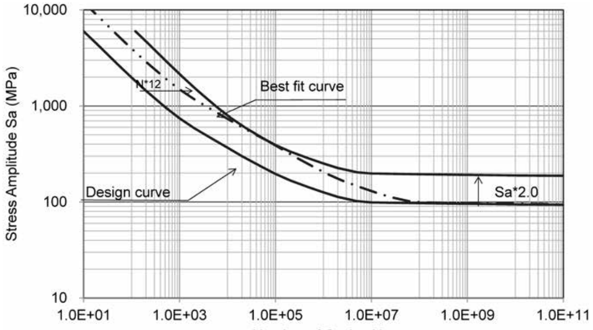

Fig. 8 S-N curve for stainless steel

Table 3 Thermal stress evaluation for design condition (three streams: LNG1, LNG2, heat medium)

	LNG side	Heat medium side
Pressure	6.0 bar	2.0 bar
Temperature	-163℃	60℃
Flow rate	LNG1:840 kg/h LNG2:680 kg/h	25,300 kg/h

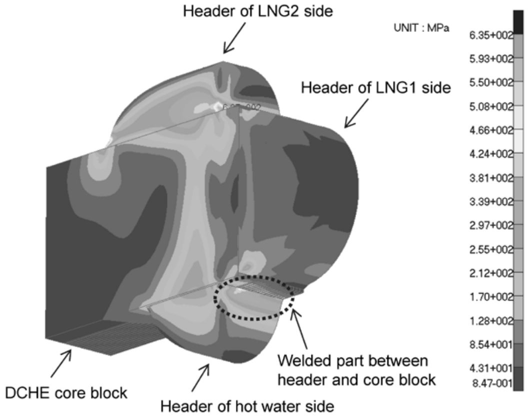

Fig. 9 Contour map of Mises stress (before improvement)

Table 4 Fatigue life evaluation for basic design and improved design

	Basic design	Improved design
Fatigue life (design)(*1)	6,900 times	40,000 times
Fatigue life (average)	75,000 times	1,000,000 times

(*1) Design fatigue life is considered safety factor by ASME rule.

body and at the weld between header and core body on the LNG side. From the maximum thermal stress amplitude at said parts and the S-N curve in Fig. 8, the design life is confirmed to be 6,900 cycles. These results confirm that the thermal stress can be reduced by properly arranging the header position to reduce the thermal stress, and at the same time, by devising the arrangement of the hot water channel. The life has been successfully improved to 40,000 cycles, which corresponds to start and stop of at least 5 times a day for over 20 years (5 times/day × 365 days/year × 20 years = 36,500 times) (**Table 4**).

5. Advantages of DCHE™ as LNG vaporizer in FGSS application

5.1 Design life (thermal stress)

The LNG vaporizers in the FGSS applications experience significant temperature differences between fluids, in which operating variation is also expected. Therefore, it is important to estimate the design life in advance, giving consideration to thermal stress.

Kobe Steel has delivered more than 200 units of the DCHE™ to hydrogen refueling stations since 2012. Thermal stress analysis has also been conducted for verification in advance for these hydrogen refueling stations. One of the advantages of the DCHE™ is that appropriate life evaluation and design improvement can be performed on the basis of experience with actual products.

5.2 Integration of vaporizer for tank pressurization and vaporizer for main engine

A low-pressure LNG vaporizer application may require two heat exchangers, i.e., an LNG vaporizer for tank pressurization and a LNG vaporizer for the main engine. In such a case, the LNG vaporization heat exchanger for tank pressurization is activated to send out the LNG in the tank to supply it to the vaporizer for the main engine. It is an advantage for customers that an inexpensive system can be configured without using a pump. Several customers have adopted the above system. Instead of the two-units of two-fluid heat exchangers in a conventional system, the DCHE™ enables the proposal of one-unit of a three-fluid heat exchanger, comprising LNG for tank pressurization, LNG supplied to the main engine, and the fluid on the HOT side (**Fig.10**). This enables the reduction of the number of heat exchangers and effective utilization of the space. Another advantage is the ability to reduce peripheral piping and mounting. The fact that not only two fluids, but also multiple fluids can exchange heat is also considered to be an advantage of the FGSS application using the DCHE™.

5.3 Antifreezing structure

For stable operation of LNG vaporizers, freezing of the heat medium is currently cited as the greatest concern for the customers. The DCHE™ can suppress freezing with Concept 1: stacked structure (COLD: HOT = 1: 3 structure); furthermore, as mentioned in Section 3.2.2, the design guidelines against freezing have also been established. The load of LNG fuel ship operation fluctuates and, if the operating conditions are provided by customers, it is possible to design with the focus on the risk of freezing during load fluctuations, in addition to the freezing risk evaluation, at the time of design.

Even if freezing should occur, recovering from freezing is possible while continuing operation, although it is necessary to reduce the natural gas

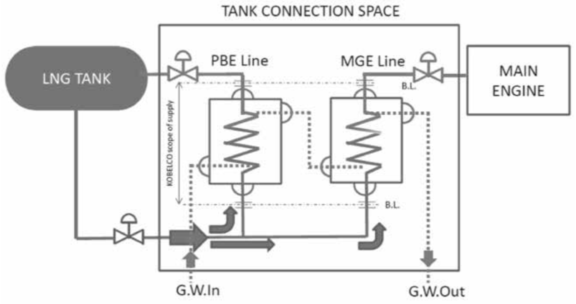

Layout of plate & shell type (two HX)

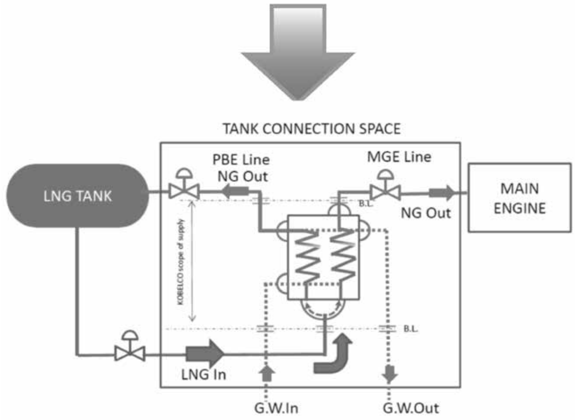

Layout of DCHE type (one HX)

Fig.10 System flow diagrams

flow rate, as mentioned in Section 3.1.2, which contributes to the continuous operation of natural gas processing plants.

5.4 Cost reduction by standardization

In an FGSS application, the amount of vaporization is pre-determined to some extent for each output of the main engine of the LNG fuel ship. Hence, cost reduction can be realized by standardizing equipment, preparing standard products for each vaporization amount, and manufacturing them as semi-general-purpose products.

Currently, several standard products are continuously manufactured for the DCHE™ used in hydrogen refueling stations. Here, standardization of the parts and simultaneous manufacturing have enabled cost reduction compared with the case where only one unit is manufactured. With reference to these achievements, Kobe Steel plans to promote cost reduction by standardization even for medium- and small-capacity LNG vaporizers, including those for FGSS applications.

Conclusions

This paper has introduced the characteristics of the DCHE™ in LNG applications, focusing on the design aspect. Influenced by environmental regulations, the number of LNG vaporizer applications is expected to increase in the future. Regarding the DCHE™, we would like to continue to focus on expanding sales by exploiting its compactness and the ability to integrate multiple fluids. In addition, heat exchangers used in gas treatment plants are being studied more and more as an applicable use involving natural gas.

As a manufacturer capable of proposing both the DCHE™ and ALEX™, Kobe Steel would like to contribute to the supply of equipment to the ever-increasing number of natural gas plants.

References

1) K. Noishiki et al. *R&D Kobe Steel Engineering reports*. 2003, Vol.53, No.2, pp.28-31.
2) Y. Miwa et al. *R&D Kobe Steel Engineering reports*. 2013, Vol.63, No.2, pp.23-27.
3) S. Matsuzawa. JOGMEC document. "US oil and natural gas situation centered on shale". November 22, 2018.
4) Engineering network. October 25, 2019.
5) Ministry of Land, Infrastructure, Transport and Tourism website, https://www.mlit.go.jp/report/press/kaiji07_hh_000095.html, (accessed 2019-12-06).
6) Ocean Development and Environment Policy Division, Ministry of Land, Infrastructure, Transport and Tourism, "Greenhouse gas reduction measures from international shipping" August 2018, http://www.mlit.go.jp/common/001250110.pdf, (accessed 2019-12-06).
7) T. Yoshida et al. *R&D Kobe Steel Engineering reports*. 2013, Vol.63, No.2, pp.37-39.
8) NEDO. "Trends in hydrogen and fuel cell technology development in the United States." June 17, 2019, https://www.nedo.go.jp/content/100895017.pdf, (accessed 2019-12-06).
9) N. Takeo. "Hydrogen-related R&D trends in Europe". June, 2019. https://www.nedo.go.jp/content/100895075.pdf, (accessed 2019-12-06).
10) Ministry of Economy, Trade and Industry. "Hydrogen / Fuel Cell Strategy Roadmap," June 2019, https://www.meti.go.jp/press/2019/09/20190918002/20190918002.html, (accessed December 06, 2019).
11) Kobe Steel, Ltd. K. Noishiki. LAMINATION TYPE FLUID HEATER, AND METHOD OF HEATING FLUID BY LAMINATION TYPE FLUID HEATER. Japanese Unexamined Patent Application Publication 2017-166775. 2017-09-21.
12) Handbook of Chemical Engineering. Maruzen Publishing, September 2011, p.260.

Large Capacity Reactor, Stacked Multi-Channel Reactor (SMCR$^{\text{TM}}$) for Flow Chemistry

Nobumasa ICHIHASHI[*1] · Tomohiro OZONO[*1] · Akira MATSUOKA[*2]

[*1] Technical Development Department, Development Center, Machinery Business
[*2] Mechanical Engineering Research Laboratory, Technical Development Group (currently Shinko Engineering & Maintenance Co.,Ltd)

Abstract

The stacked multi-channel reactor (SMCR$^{\text{TM}}$) is a (continuous) flow chemical reactor that replaces the conventional stirred bed reactors and has been developed as a reactor capable of large-capacity processing. As an effort after the development, an SMCR$^{\text{TM}}$ made of metal has been added to the lineup and, furthermore, a ceramic SMCR$^{\text{TM}}$ with high corrosion resistance has been developed to expand the applications, for which verification tests have been conducted against thermal shock. Moreover, basic tests and bench scale testing equipment have been actively commissioned and implemented with the aim of promoting the commercialization of SMCR$^{\text{TM}}$ in addition to equipment supply. As for bench scale testing, a bench scale testing apparatus installed in Kobe Steel performs verification tests to verify the usefulness of SMCR$^{\text{TM}}$ units.

Introduction

Efficient reaction can be achieved by simply flowing two different fluids through a fine channel with a diameter of approximately 1 mm. This is the principle of microchannel reactors. For the chemical manufacturing process in Japan and overseas, flow synthesis (continuous synthesis) in the fine space of a microchannel reactor is attracting attention from the viewpoint of improving efficiency, quality stability, and safety.[1), 2)] The main focus has hitherto been placed on laboratory-level studies and application studies on products in small quantities with high additive value, such as those in the pharmaceutical field. However, full-scale studies are now being conducted on applications that require large-capacity processing of fine chemicals and bulk chemicals, for example.

Kobe Steel has developed a stacked multi-channel reactor (hereinafter referred to as the "SMCR$^{\text{TM}}$"[Note 1)] as a microchannel reactor capable of large-capacity processing for flow synthesis, with the aim of applying it to commercial production plants. This paper describes the fundamental configuration and characteristics of the SMCR$^{\text{TM}}$, Kobe Steel's efforts toward its application to commercial production, and its future perspective.

1. Characteristics and applicable use of SMCR$^{\text{TM}}$

1.1 Fundamental configuration and characteristics of SMCR$^{\text{TM}}$

In general, a microchannel reactor comprises microchannels of sub-millimeter to several millimeters in diameter, such that fluids meet inside the apparatus. The greatest characteristic of microchannel reactors is that these micro channels serve as reaction fields to achieve high heat transfer performance and mass transfer rate.[3)] **Fig. 1** compares a conventional stirred-bed reactor

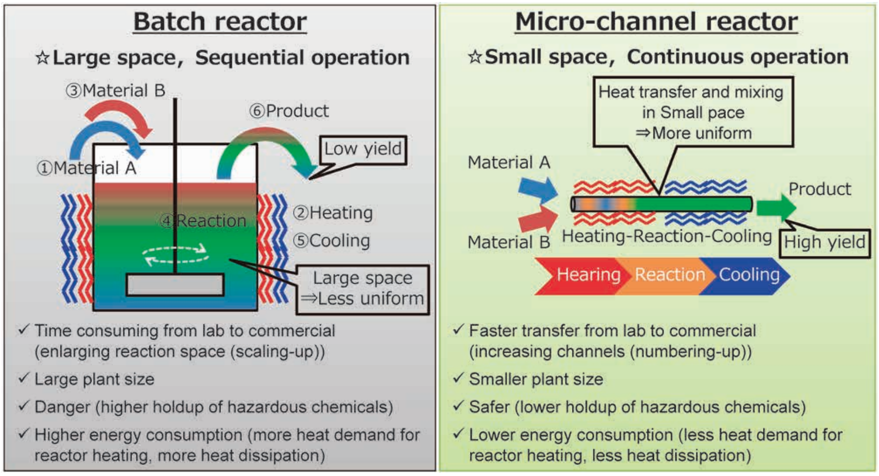

- ✓ Time consuming from lab to commercial (enlarging reaction space (scaling-up))
- ✓ Large plant size
- ✓ Danger (higher holdup of hazardous chemicals)
- ✓ Higher energy consumption (more heat demand for reactor heating, more heat dissipation)

- ✓ Faster transfer from lab to commercial (increasing channels (numbering-up))
- ✓ Smaller plant size
- ✓ Safer (lower holdup of hazardous chemicals)
- ✓ Lower energy consumption (less heat demand for reactor heating, less heat dissipation)

Fig. 1 Comparison between batch reactor and micro-channel reactor

---

[Note 1)] SMCR is a registered trademark of Kobe Steel, Ltd.

and a microchannel reactor. The throughput of each channel in a microchannel reactor is generally small, hence the throughput is increased by using a technique called "numbering-up," by which multiple channels are arranged.

The SMCR$^{\mathrm{TM}}$ is a unique product developed by Kobe Steel. This apparatus can easily be enlarged in capacity by the numbering-up of channels using chemical etching and diffusion bonding. **Fig. 2** shows the basic configuration of the channels. Multiple channels are formed on each metal plate by chemical etching, and a plurality of such plates is stacked to be firmly bonded by diffusion bonding. With such a configuration, a reactor with 10,000 or more channels can be made. The number and length of the channels inside an SMCR$^{\mathrm{TM}}$ can be freely designed depending on the reaction conditions. In addition, some of the plates may be used for heat medium channels to allow the adjustment of the reaction temperature.

With such characteristics, the SMCR$^{\mathrm{TM}}$ is a reactor that can simultaneously achieve capacity enlargement, continuous processing and apparatus downsizing for various reaction applications, and there is a strong need for their commercialization. **Fig. 3** shows the overall and inside images of the SMCR$^{\mathrm{TM}}$.

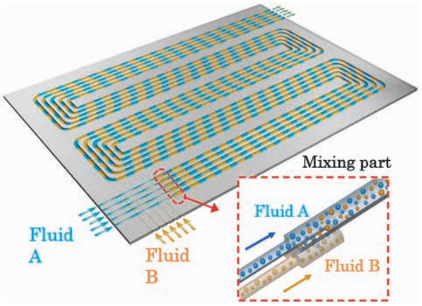

Fig. 2 Basic configuration of multi-channels in SMCR$^{\mathrm{TM}}$

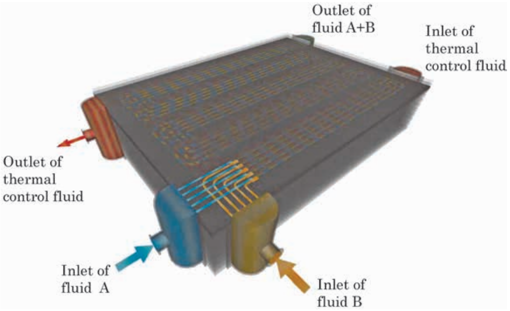

Fig. 3 Overall and inside image of SMCR$^{\mathrm{TM}}$

1.2 Applicable use of SMCR$^{\mathrm{TM}}$

The main applicable uses of SMCR$^{\mathrm{TM}}$ are considered to be "synthesis" and "extraction" in each unit operation of the chemical manufacturing process. Various organic synthesis and polymer syntheses occur at high rates with great heat of reaction, making temperature control of the synthesis difficult when conventional stirred-bed reactors are used. The use of an SMCR$^{\mathrm{TM}}$ for such synthesis enables precise temperature control and raises expectations for product quality stability and higher process efficiency.

In the extraction application, on the other hand, the use of fine channels increases the contact area, making the extraction of the target substance more efficient. In addition, since no active fluid mixing is performed in the channel inside the SMCR$^{\mathrm{TM}}$, the phase separation performance after extraction is significantly improved compared with the conventional stirred-bed reactors. The expected applications that can exploit these merits include the removal of impurities and catalysts after reactions and the recovery of rare metals.

2. Toward the commercialization of SMCR$^{\mathrm{TM}}$

Fig. 4 shows the main steps in development aimed at commercial production based on the SMCR$^{\mathrm{TM}}$. Basically, fundamental laboratory testing is performed first to optimize the reaction conditions in a manner similar to the development of the conventional chemical process. After that, bench-scale testing is performed using a SMCR$^{\mathrm{TM}}$ with multiple channels to confirm any differences from the results of the basic testing. Finally, the performance and operation control are checked

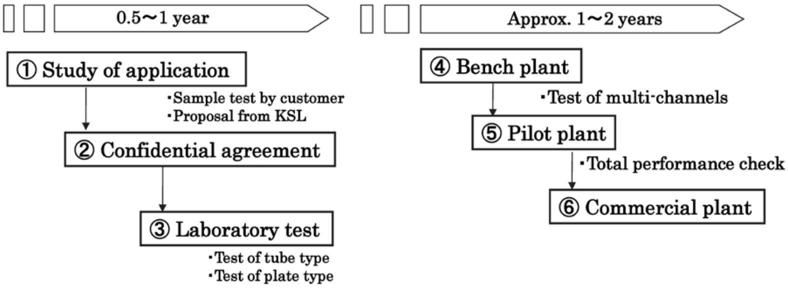

Fig. 4 Development workflow for commercialization

by pilot testing using a plant that has the same function as that used in commercial production, and the process shifts to commercial production. As mentioned earlier, when SMCR™ is used, a technique called numbering-up can be adapted to increase the throughput and to proceed to commercialization. Therefore, the reaction conditions obtained by the basic testing can be used as they are for commercial production, which reduces the risks in developing chemical processes and raises the expectation of cost reduction and period shortening.

Since the SMCR™ can be disposed in parallel or in series, there is theoretically no upper limit to capacity enlargement. In terms of configuration, it has enough functions for commercialization. On the other hand, for highly corrosive applications, metals that can be etched or diffusion bonded cannot be used. Therefore, it is necessary to solve the problems associated with the materials in order to expand the application.

Hence, Kobe Steel has been conducting the development of the ceramic SMCR™ in an effort to further promote the commercial production of the SMCR™. Furthermore, the company has been accepting consignment tests for the basic examination stage and bench stage in order to enhance the process (software) toward aiming at commercialization. The following sections introduce the details of the efforts and their results.

3. Development of ceramic SMCR™

Initially, the SMCR™ had only one lineup of apparatuses made of metals, mainly stainless steel. There are, however, many applications that cannot be handled by metallic apparatuses, e.g., applications that require corrosion resistance such as processes that use large amounts of acids and alkalis, and applications in the pharmaceutical, semiconductor and food industries, that permit no elution of metallic ions. The ceramic SMCR™ was developed with the aim of expanding its use to such applications.

3.1 Characteristics of ceramic SMCR™

Ceramics generally have high corrosion resistance and also have high strength at high temperatures. On the other hand, they are prone to brittle fracture, and caution is required during operations involving rapid heating and rapid cooling. Kobe Steel has optimized the configuration of SMCR™ by structural analysis and developed a ceramic SMCR™ with excellent thermal shock resistance. More specifically, the configuration includes a metal or resin flange separated from the ceramic core of the main body, in which fluids are supplied and extracted from the flange, as shown in **Fig. 5**. The ceramic SMCR™ has the following characteristics:

① Discontinuous shapes in the fluid supply have been eliminated from the ceramic body, leaving only straight channels. As a result, the stress concentration has been relaxed to ensure configuration with high thermal shock resistance (see **Fig. 6**).

② The channels were arranged as much as possible in the ceramic core so as to minimize the ceramic parts without channels, which are insensitive to temperature change. This has made it possible to equalize the temperature distribution in the apparatus when the fluid supply has a temperature different from that of the ceramic core, and thus to minimize the occurrence of thermal stress.

3.2 Implementation of thermal load test

In order to verify the thermal shock property, a ceramic SMCR™ with the configuration described in Section 3.1 and the specifications shown in **Table 1** was prepared to perform a thermal load test. In other words, it was verified whether or

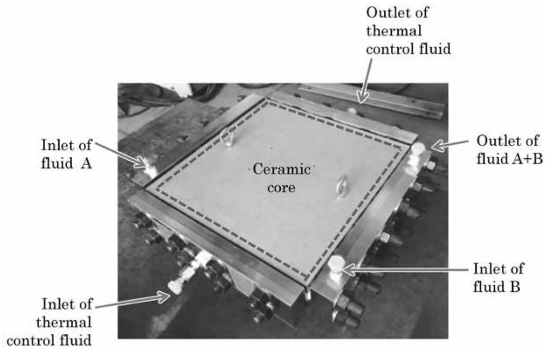

Fig. 5 Ceramic SMCR™

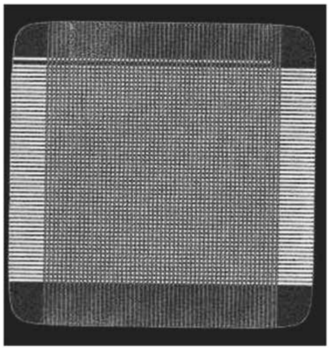

Fig. 6 Channel configuration inside ceramic SMCR™

Table 1 Specifications of ceramic SMCR™

Size (mm)	465 × 505 × 185
Weight (kg)	75
Channel specification	Size : 2 (mm) rectangle Length : 36 (m) Number : 1 Channel
Material (core)	Alumina (Al_2O_3)
Material (flange)	Hastelloy/ PEEK / PPS
Design temperature (° C)	180
Design pressure (MPa)	2
Internal volume (ml)	max. 144

not the apparatus can be used in the actual operation environment by clarifying the permissible temperature difference between the temperature of the fluid supplied to the temperature adjustment channel at the startup and the surface temperature of the apparatus. The permissible temperature difference between the apparatus and fluid that would ensure the safe use of the apparatus was set to 65℃ on the basis of the results of thermal shock tests and analysis using steam and liquid nitrogen. If the temperature difference between the apparatus and fluid is expected to exceed 65℃ at the starting up of the apparatus, the apparatus must be preheated step by step to manage the temperature difference with the fluid.

In the future, actual operational data will be accumulated to further improve the accuracy of the permissible values and to expand the applications of the apparatus for commercial production.

4. Implementation of Consignment testing

In the early days of the SMCR™ development, it was intended to have customers optimize the reaction conditions applied to the SMCR™, and Kobe Steel aimed at commercialization by designing the SMCR™ in accordance with the reaction conditions. There was, however, a problem in that it is difficult for customers to prepare experimental equipment and determine experimental conditions. Now, as Kobe Steel's latest effort, the company is happy to accept the consignment of various kinds of tests in the stages of basic testing and bench-scale testing. This owes to the fact that Kobe Steel has basic testing equipment and a bench unit in its laboratory. In addition to the basic testing and bench-scale testing, the specifications of the SMCR™ for commercial production are examined on the basis of the test results, and the economic evaluation is carried out in a consistent manner, which raises the expectations for promoting commercialization.

4.1 Bench unit

A bench unit was installed in 2018 at Kobe Steel's Corporate Research Laboratories. The appearance of the bench unit is shown in **Fig. 7**. The bench unit has the devices and instrumentation (tank, pump, various sensors, separator, heat medium/refrigerant supply unit, etc.) necessary for the SMCR™ operation and is configured to adapt the SMCR™ in accordance with reaction conditions and throughput. The major purposes of installing/using the bench unit are as follows:

① To acquire knowledge about operation and control on a commercial scale by conducting bench-scale testing incorporating the SMCR™.
② To obtain complementary data between basic testing and commercial production through bench-scale testing using the SMCR™.
③ To provide a showroom of unit equipment for flow synthesis, and to carry out external promotion.

4.2 Verification test using bench unit

Verification testing was performed using the

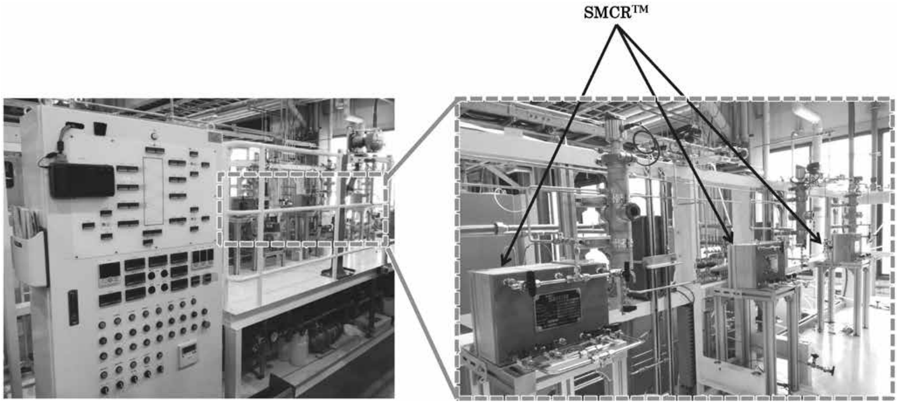

Fig. 7 Bench stage unit

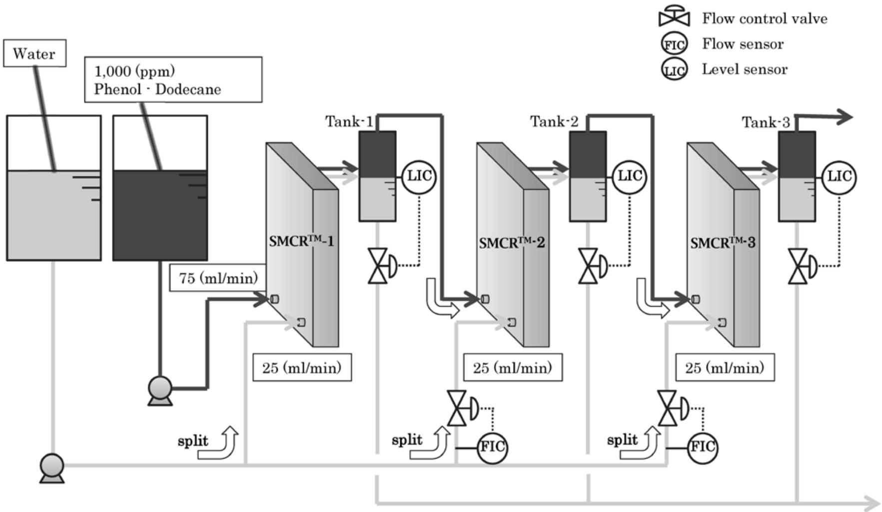

Fig. 8 Flow diagram of SMCR™ bench unit

bench unit to confirm the usefulness of the bench unit installed and of the SMCR™ incorporated therein. This test targeted the extraction operation, in which dodecane with phenol, dissolved as a simulated extraction substance, and water, a phenol extractant, were brought into liquid-liquid contact in an SMCR™ so that phenol was extracted to the water side. The data obtained from the extraction test in a single channel was used to estimate the performance of the standard type SMCR™ to confirm whether the estimated extraction efficiency could be achieved. **Fig. 8** shows the flowchart of this test, and **Fig. 9** shows the appearance of the standard SMCR™ installed.

The standard type of SMCR™ has 24 semicircular channels with a radius of 1 mm. This extraction operation was carried out in a multi-stage (3 stage) operation system, in which dodecane with 0.1 wt% phenol dissolved was pumped sequentially from the 1st stage to the 3rd stage, while solvent clean water was supplied to each of the stages. A level sensor was attached to the phase separation tank downstream of the SMCR™ at each stage to measure the interface position between the phenol-dodecane solution and water in the tank. The adopted method includes controlling the discharge amount of the water phase so that the interface position is kept constant while pumping dodecane to the SMCR™ in a later stage, thereby enabling simple operation without increasing the number of pumps.

The results of the bench-scale testing are shown in **Fig.10** to **Fig.13**.[4] Fig.10 shows the temporal change in the height of the dodecane-water interface in each phase separation tank attached to the subsequent stage of the respective SMCR™. These figures confirm that the height of the dodecane-water interface in the phase separation tank in

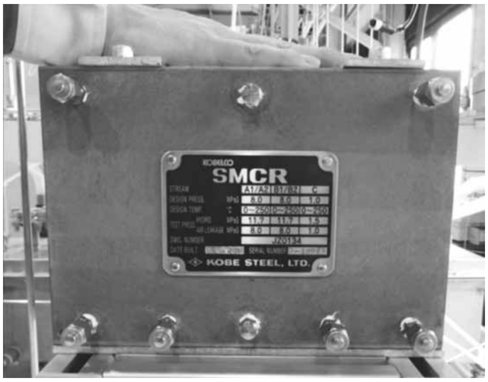

Fig. 9 Standard SMCR™

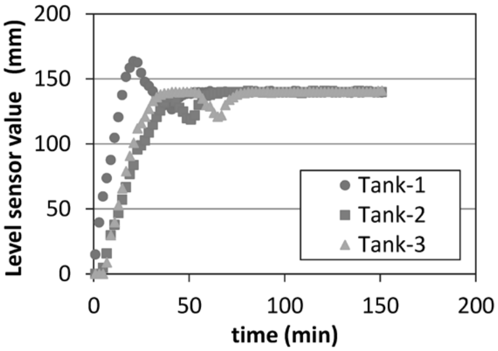

Fig.10 Temporal change of interface level at each stage

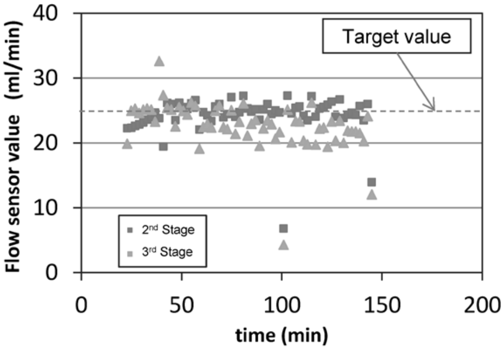

Fig.11 Flow rate of water phase of each stage

each stage was successfully kept constant. **Fig.11** shows the temporal change in the amount of water supplied to each stage, confirming that the distribution of water to the 2nd stage and the 3rd stage can be controlled stably near the set value, although there is some variation.

Fig.12 shows the extraction efficiency of phenol in dodecane to the water side at each stage. The efficiency *E* of phenol extraction is expressed by Equation (1) using the initial phenol concentration C_0 in dodecane and the phenol concentration C_n in dodecane at the outlet of the phase separation tank at the *n*th stage:

$$E=\frac{C_0-C_n}{C_0} \quad \cdots\cdots (1)$$

Fig.12 shows that the extraction efficiency of each stage is constant regardless of the passage of time, allowing stable extraction.

Fig.13 shows the experimental and estimated values of phenol extraction efficiency at each stage. The estimated value of phenol extraction efficiency in each stage is the equilibrium extraction efficiency calculated from the relationship of phenol concentration between the water side and the dodecane side (extraction isotherm) in the equilibrium state, in which the relationship has been obtained by a batch-type extraction test on a beaker scale, Fig.13 shows that the estimation results based on the equilibrium-state phenol-extraction data obtained by the batch-type extraction test and the bench-scale testing results are almost the same, confirming that an SMCR™ extraction system can be designed by using the batch-type extraction test results.

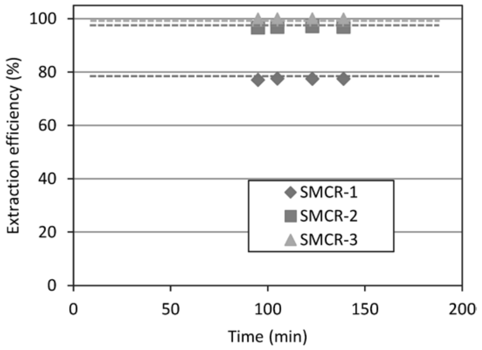

Fig.12 Temporal change of extraction efficiency

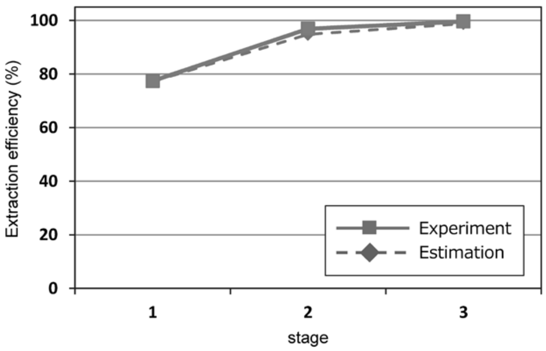

Fig.13 Experimental and estimated values of phenol extraction efficiency at each stage

5. Future perspective of SMCR™

In efforts such as the apparatus supply of SMCR™ and the latest basic/bench-scale testing, the goal is to achieve the early commercialization of SMCR™, and the standardization of SMCR™ units will be carried out with a mid- to long-term vision. Currently, custom-made specifications of SMCR™ for commercial production are being considered on the basis of the results of basic testing for each application and each customer. Cost reduction will be realized by defining a standard unit including the pump, tank, and instrumentation in addition to SMCR™ and by lining them up in accordance with the throughputs.

On the other hand, in order to apply the standard unit to processes with different reaction conditions, a circulation system as shown in **Fig.14** will be built as a standard unit. This is the concept of, for example, in the cases of multi-stage extraction, returning the ingredients and solvent to their respective tanks after extraction for a certain period of time in an SMCR™, and repeating this operation for a certain period of time to replenish the solvent to continue the extraction operation in the SMCR™. This operational method eliminates the need to change the specifications of the unit for any extraction time and number of extraction cycles, thus simplifying the configuration of the unit. In the future, detailed specifications and verification tests will be conducted on these standard units with the aim of putting them into practical use for their early commercialization.

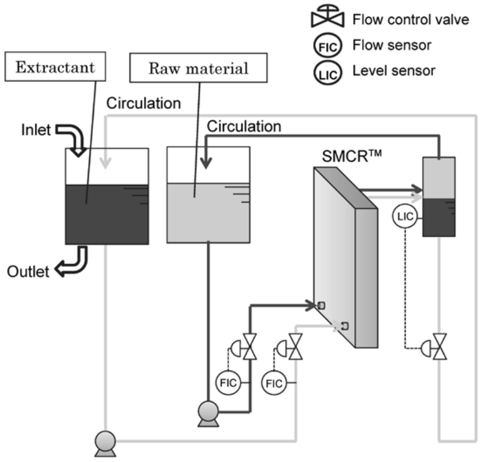

Fig.14 Concept of circulation unit

Conclusions

This paper has introduced the characteristics of the SMCR™, as well as Kobe Steel's latest efforts and future perspectives. The recent measures taken against environmental problems and the growing need for higher production efficiency will make a transition from batch processing to flow synthesis production. Such process conversion, however, has many problems that must be solved. Hence, Kobe Steel has been conducting the development of apparatuses such as a ceramic SMCR™, along with basic and bench-scale testing, so as to promote customer adoption of flow synthesis. As a result, there are an increasing number of cases where specific examination is conducted with the awareness of commercialization. To this end, Kobe Steel hopes to contribute to the conversion to flow synthesis production by achieving early commercial production and accelerating the initial examination of flow synthesis through the supplying of standard units.

References

1) Microreactor technology. NTS Inc. 2005, pp.1-10.
2) M. N. Kashid et al. Chem. Eng. Sci., 2011, Vol.66, pp.3876-3897.
3) J. Yoshida. Development and application of microreactors. CMC Publishing Co., Ltd. 2003, p.4.
4) R. Matsuoka, et al. Bench-scale demonstration of multi-stage continuous process with large capacity microchannel reactor (SMCR™). 18th Asian Pacific Confederation of Chemical Engineering Congress (APCChE 2019).

Compressed Air Energy Storage System

Hiroki SARUTA[*1] **・ Dr. Takashi SATO**[*1] **・ Masatake TOSHIMA**[*2] **・ Yohei KUBO**[*3]

[*1] Development Center, Machinery Business
[*2] Technical Development Department, Development Center, Machinery Business（currently New Energy and Industrial Technology Development Organization）
[*3] Mechanical Engineering Research Laboratory, Technical Development Group

Abstract

Large-scale power storage equipment for leveling the unstable output of renewable energy has been expected to spread in order to reduce CO_2 *emissions. The compressed air energy storage system described in this paper is suitable for storing large amounts of energy for extended periods of time. Particularly, in North America, China and other areas, where rock salt layers are widely distributed, using underground spaces formed in the rock salt layers to store compressed air can reduce the unit kWh cost of equipment. The equipment's responsiveness was obtained on the basis of the data for large-scale demonstration equipment of 1 MW class, verifying that the equipment can respond to commands within seconds. This paper further describes the future development of the compressed air energy storage system.*

Introduction

Recently, the introduction of renewable energy is progressing rapidly worldwide as a result of the requirements imposed both by the Paris Agreement on climate change control to reduce greenhouse gas emissions and also by the significant decrease in the unit power price of photovoltaic and wind-power generation.

There is, however, the problem that the power generated by photovoltaic and wind-power generation, or renewable energy, is not stable, due to solar irradiation and weather conditions. Therefore, if it is interconnected to the grid as-is, it becomes a disturbance factor to the power grid. This may disrupt the balance between the supply and demand of electricity, causing frequency fluctuations, and in the worst case, triggering power outage. Renewable energies such as wind power and photovoltaic power cannot be controlled to match the demand, causing a mismatch between the supply and demand. This mismatch is now relaxed mainly by adjusting the output of thermal power generation. If the unstable output can be leveled to decrease the adjustment load, the utilization of renewable energy will be encouraged. Hence, the wide-spread use of large-scale power storage plants that can level the power generation output is required, from the viewpoint of CO_2 emission reduction.

It is against this backdrop that Kobe Steel has received an order for, and delivered, a new compressed-air energy storage (hereinafter referred to as "CAES") system using a screw-type compressor/expander from the Institute of Applied Energy and has contributed to a verification test conducted by said institute and Waseda University for a year and a half beginning in April 2017. It should be noted that this verification test was carried out as a part of the "R&D Project on Grid Integration of Variable Renewable Energy" promoted by the New Energy and Industrial Technology Development Organization (hereinafter referred to as "NEDO").

This paper introduces the performance of the CAES plant designed and built by Kobe Steel and describes the future development in Kobe Steel.

1. CAES plant

Kobe Steel's CAES technology comprises storing compressed air in a tank with a screw-type compressor first; and subsequently expanding the stored compressed air with a screw-type expander to drive a power generator that is directly connected to the expander and thus to generate electricity, wherein the heat generated by the compression is collected by a heat medium for preheating the compressed air before it flows into the expander, thereby improving charge/discharge efficiency. In addition, thermal insulation measures are taken to prevent the charge/discharge efficiency from decreasing due to heat dissipation loss in the equipment.

Fig. 1 and **Fig. 2** show the flow of the CAES system at the time of charging and discharging, respectively. As can be seen by comparing these, the directions of the flows of the compressed air and heat medium are opposite, but the main components are almost the same for charging and discharging. A screw compressor can be used as-is for a screw expander by rotating its screw in the reverse direction. This means that the system can be configured as a compressor-cum-expander. Such a configuration not only makes the plant compact, but also reduce its cost significantly.[1)]

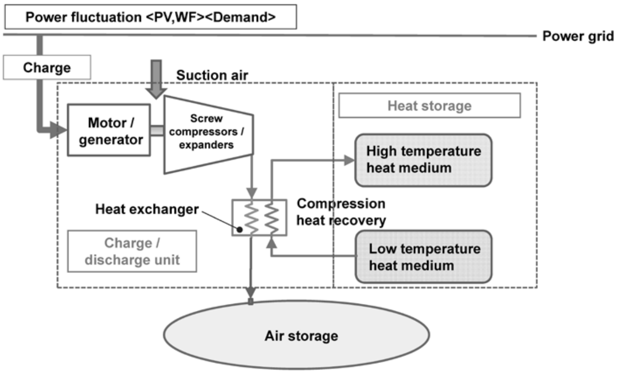

Fig. 1 Charge flow of CAES system

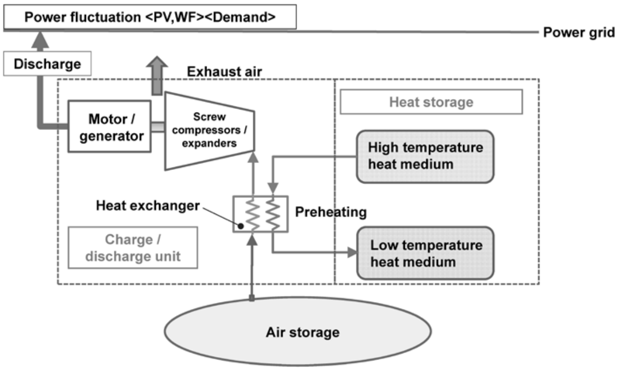

Fig. 2 Discharge flow of CAES system

2. Overview of demonstration plant

When developing the technology for a thermal insulation type CAES, Kobe Steel first installed a 50 kW class small-scale prototype in the Kobe Corporate Research Laboratories and conducted various basic tests. The know-how gained from this small-scale prototype has led to the delivery of a large-scale demonstration plant of 1 MW class to the Institute of Applied Energy. The following provides an overview of these two plants.

2.1 50 kW small-scale prototype

Fig. 3 shows the appearance of the 50 kW class small-scale prototype installed in Kobe Corporate Research Laboratories of Kobe Steel. This plant is based on Kobe Steel's standard oil-free screw compressors (output 55 kW) that have been modified into a compressor and expander for experiments on CAES technology. The accumulator that stores compressed air consists of four steel tanks, each having an internal volume of 7.6 m^3 and a withstanding pressure of 0.97 MPa G.

In February 2016, this in-house experimental plant began power generation tests, including the test runs of the compressor and expander and the performance test of the heat exchanger. The knowledge gained through these tests has led to the design and construction of a large 1 MW class demonstration plant.

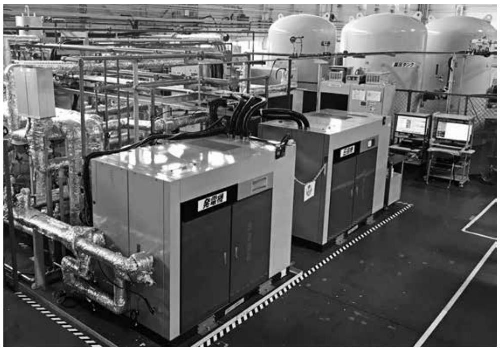

Fig. 3 Appearance of 50 kW small-scale prototype

Fig. 4 Appearance of 1 MW large-scale demonstration plant

2.2 Large-scale demonstration plant of 1 MW

Fig. 4 shows a large-scale demonstration plant of 1 MW class, that was installed at Higashiizu-cho, Kamo-gun, Shizuoka Prefecture (hereinafter referred to as the "Izu demonstration plant").[2), 3)] This plant was installed adjacent to the Higashiizu Wind Farm of Tokyo Electric Power Company Holdings, Inc., and underwent a pre-use inspection by the Ministry of Economy, Trade and Industry in March 2017 before beginning operation in April of the same year. Since then, the Institute of Applied Energy and Waseda University had conducted various experiments on the fluctuation relaxation of power generated by the wind farm for a year and a half until the power plant was closed in October 2018.

This plant comprises two sets of 500 kW basic units, each consisting of three units, namely, a charging unit, heat-accumulation unit, and discharging unit, in which the two sets are connected in parallel, enabling the charging/discharging of 1 MW power at the maximum.

The housing of each unit had the size of a 20-foot container to facilitate transportation from the Kobe Steel factory to the verification test site and on-site installation work, etc. As a result, the installation work period, including the installation of the

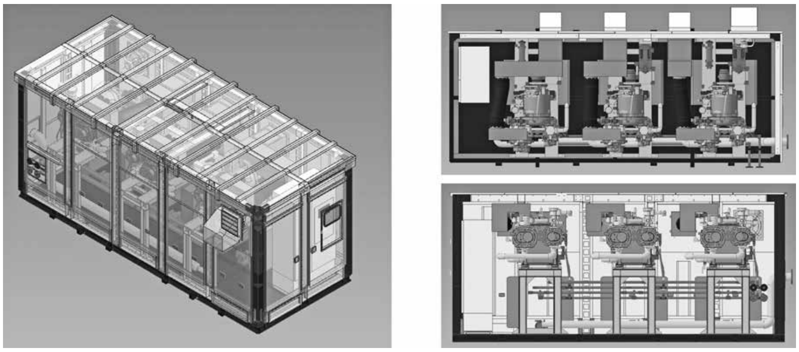

Fig. 5 500 kW charging unit

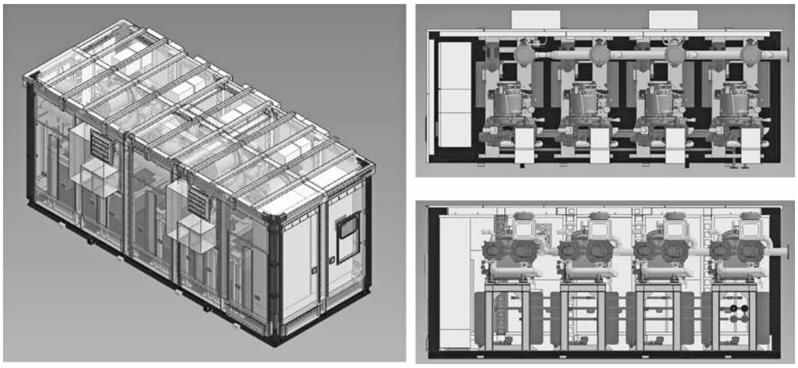

Fig. 6 500 kW discharging unit

compressed air tank, was reduced to less than one month. Housing in a standard container also offered the advantage of facilitating maintenance work after the beginning of operation. In addition, multiple basic units were connected in parallel in order to avoid stopping the entire plant during periodic inspections and repairs. **Fig. 5** and **Fig. 6** show the overviews of the charging unit and discharging unit, respectively. Each figure includes a transparent perspective view showing the internal structure, along with the front view and top view.

The charging unit houses three main bodies of Kobe Steel's standard oil-free two-stage screw compressors of 160 kW class with heat exchangers placed underneath. The combination of unit control and revolution control has enabled a continuous output control up to 500 KW. The heat generated during compression is absorbed in the heat medium by the heat exchanger and stored in the heat medium tank housed in the heat-accumulation unit. The maximum temperature of the heat medium was kept below 200℃, so as to allow the use of the general-purpose compressors.

The discharging unit, on the other hand, houses the main bodies of four 160 kW class oil-free two-stage screw compressors, which are rotated in the direction reversed from that during compression so as to serve as expanders. The difference in the number of compressors and that of expanders is resulted from the consideration of the charge/discharge efficiency. The high temperature heat medium in the heat-accumulation unit is used as the heat source of the heat exchanger for heating the compressed air at the ambient temperature in the air tank to produce high-temperature compressed air. The high-temperature compressed air is supplied to the expander so that the screw is rotated with the torque caused by the pressure difference from the atmosphere to drive the power generator.

3. Performance of Izu demonstration plant

The Izu demonstration plant used screw-type compressors and expanders. This offered the advantage of excellent responsiveness to charging and discharging commands compared with the turbo-type compressors and expanders used in conventional CAES systems. This section focuses on the responsiveness obtained by operating the Izu demonstration plant.

3.1 Startup performance

Fig. 7 shows an example of the response characteristics when the Izu demonstration plant is started from the standby state to the maximum charging state of 1 MW. Also, **Fig. 8** shows an example of the response characteristics when it

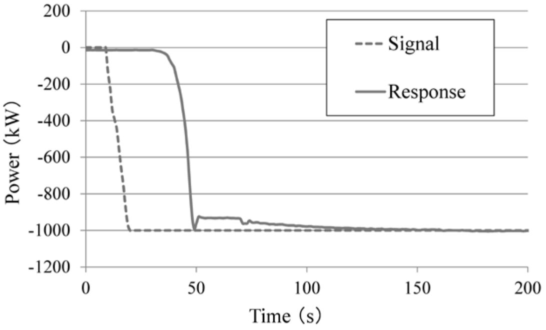

Fig. 7 Response time in charging

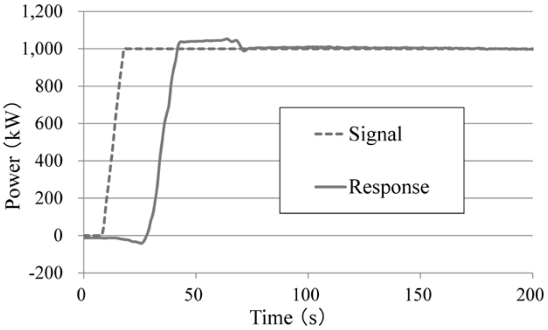

Fig. 8 Response time in discharging

is launched to the maximum discharging state of 1 MW. In Fig. 7 and Fig. 8, zero on the vertical axis indicates the zero charging/discharging state, negative values indicate charging states (compressor operating states), and positive values indicate discharging states (expander operating state).

As shown in Fig. 7 and Fig. 8, the maximum charging or discharging power can be reached in approximately 30 seconds from the stopped state after receiving the command value (signal). This indicates that it is fully usable for relaxing the output fluctuation of the wind farm.

The response time of start-up is expected to remain almost the same for even larger-scale plants of several tens of MW class, since they can be handled by adding the units in parallel. A backup power supply in case of power outage requires a separate device for measures against momentary power failure, and the plant is exploitable as equipment that can supply a large amount of electric power fairly soon.

3.2 Command-following performance

The power generation output of a wind farm changes greatly depending on the wind conditions, and thus the responsiveness to the output command is important in order to mitigate the fluctuation.

The evaluation of the command-following performance of the Izu demonstration plant used the simulated command (Reg. D) for the response confirmation test released by PJM Interconnection LLC (PJM), a power transmission company in the northeastern United States,[4] and the responsiveness of the CAES plant was evaluated. **Fig. 9** shows an example of the results.

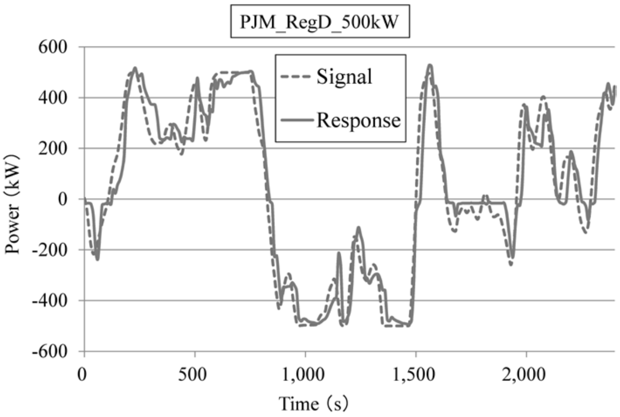

Fig. 9 Response to PJM Reg. D signal

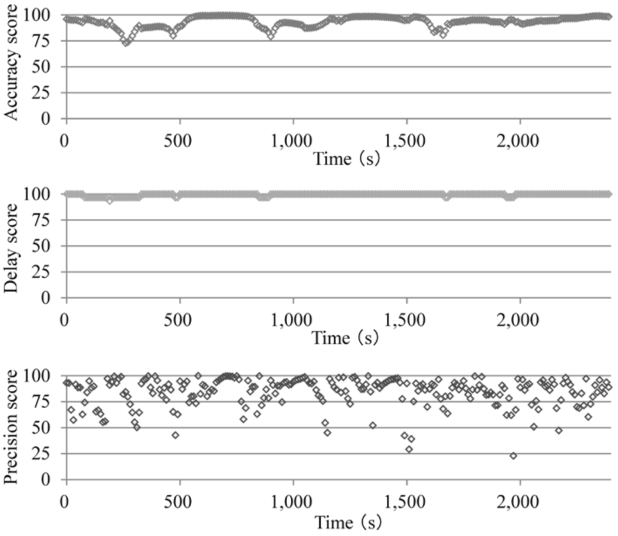

Fig.10 Results of PJM performance scores

The power command in Fig. 9 uses a waveform obtained by scaling the Reg. D Normalized Self-Test Signal released by PJM with the maximum value of plus or minus 500 KW. The response characteristics of the CAES plant were measured on the basis of the PJM responsiveness performance evaluation method. The evaluation results are shown in **Fig.10**. The evaluation is based on three scores, i.e., accuracy score, delay score, and precision score. The evaluation equation for each score is shown below.

$$Accuracy\ Score_{\delta=0\ to\ 5\ min}=\gamma_{Signal\ ,Response(\delta,\delta+5min)}$$

$$Delay\ Score=Abs\left|\frac{\delta\text{-}5\ Minutes}{5\ Minutes}\right|$$

$$Error=Avg\ of\ Abs\left|\frac{Response\text{-}Regulation\ Signal}{Hourly\ Average\ Regulation\ Signal}\right|$$

$$Precision\ Score=1-\frac{1}{n}\sum Abs(Error)$$

wherein, γ : correlation coefficient,
n : number of samples per unit time.

For the Izu demonstration plant, the simple average of each score of the 40-minute test was accuracy, 93.3; delay, 99.46; and precision, 84.12, respectively, with the average of the three values recording a high score of 92.29. PJM requires a performance score of 75 points or higher for a continuous test signal of 40 minutes as a condition for entry into the frequency adjustment market. The above score for the Izu demonstration plant is considered to be at a level that can sufficiently be used for a power-coordinating facility in the electricity market. It should be noted that several tests, performed by changing the conditions such as the amount of compressed air storage and the scaling width of the Reg. D test waveform, has confirmed a performance meeting the requirement of 75 points or above.

4. Future perspective

4.1 Performance improvement and cost reduction

The Izu demonstration plant has shown that a plant using oil-free screw compressors as key components can be used for the relaxation of output fluctuations of a wind farm. In order to expand the use of CAES facilities, however, further performance improvement and cost reduction are necessary.

Currently, Kobe Steel is aiming at achieving both the performance improvement and cost reduction by combining the charging unit and discharging unit. The company is also considering increasing the storage pressure to reduce the volume of the compressed air storage tank.

Fig.11 shows the overview of a charging-cum-discharging unit in which the screw compressor currently under consideration is used for charging and discharging and the maximum storage pressure is increased to 2 MPaG. This unit comprises three screw compressors with a maximum discharge pressure of 1 MPaG and one screw compressor with a maximum discharge pressure of 2 MPaG, each being usable as a compressor-cum-expander. The combination of unit control and revolution control has enabled continuous output control up to 555 KW.

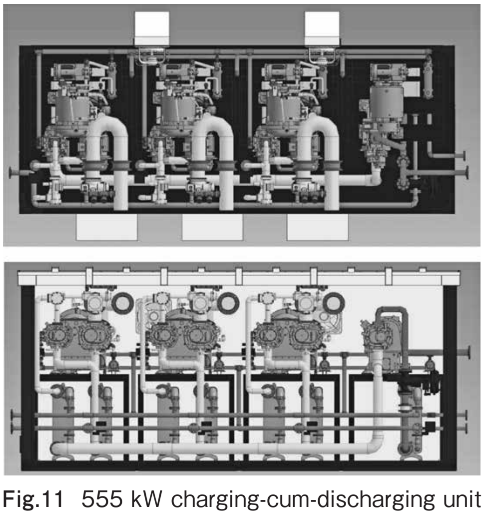
Fig.11 555 kW charging-cum-discharging unit

A study is being conducted to boost the pressure to approximately 5 MPaG by combining screw compressors with a discharge pressures higher than those of the example shown in Fig.11.

4.2 Global developments

There are specific plans to introduce CAES plants in countries where the introduction of renewable energy is progressing, particularly in North America and the People's Republic of China. In China, the construction of a CAES plant of several tens of MW has begun in Jiangsu as a national project.

The reason why CAES plants are highly evaluated in these countries is the existence of underground rock-salt beds, which do not exist in Japan. In North America, for example, underground rock-salt beds are widely distributed in plains on the eastern side of the Rocky Mountains, from Texas to Alberta, Canada, passing through Kansas, and on the eastern side of the Great Lakes. These underground rock-salt beds are not only used for rock salt mining, but also utilized as an underground space, formed in the rock-salt beds, for storing natural gas, for example. Since these underground spaces are excellent in airtightness, they may be used as storage tanks for compressed air; they represent/there is a possibility of realizing storage for large amount of energy at a low cost. For example, the power storage duration of a general large-scale lithium-ion battery with greater than MW capacity is from 4 hours to 8 hours at the longest. In a CAES plant that can secure a giant underground space such as a rock salt cavern, the power storage time can be significantly extended from approximately 24 hours to 48 hours.

The plains on the eastern side of the Rocky Mountains mentioned earlier are roughly in line with the suitable location for wind farms in the United States. Hence, there are expectations in this region for controlling the electrical power generated by the wind farms and planning the generation of power based on wind-power. Furthermore, there are expectations of obtaining backup power sources that will cover the needs of communities of a certain size during power outages.

Fig.12 depicts the concept of a CAES plant that utilizes the underground space formed in a rock-salt bed as a storage tank for compressed air. Fig.12 shows an example in which the CAES plant is interconnected with the transmission line of a wind farm, but it can also be interconnected with a photovoltaic power generation plant.

The only apparatuses installed on the ground are the containers housing the charging/discharging units and the electric plants. Although the footprint area may be no major issue in North America, the plants on the ground can be compactly organized with an appearance similar to that of a lithium-ion battery.

In 2019, Kobe Steel's proposal, "Demonstration Study of Underground Compressed Air Storage for Realizing Large-Scale Power Storage (North America)" was adopted by NEDO as a part of the "International Demonstration Project on Japan's Energy Efficiency Technologies: surveys of the suitability of demonstration requirements." In response to this, the company is currently exploring the possibility of developing CAES plants, mainly in the North American region.

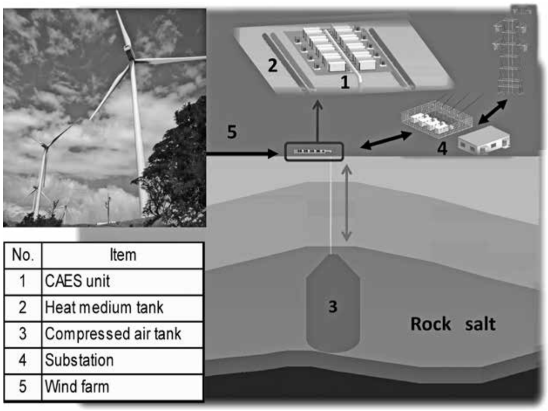

No.	Item
1	CAES unit
2	Heat medium tank
3	Compressed air tank
4	Substation
5	Wind farm

Fig.12 CAES plant using rock salt cavern

Conclusions

As a large-scale power storage unit with specifications for long-term storage and extended continuation of discharge, the compressed-air energy storage plant can be superior to (less expensive than) other power storage units in terms of the ratio of plant cost to the amount of power (kWh) that can be stored, that is, the unit price of kWh. In particular, when an underground space such as a rock salt cavern is utilized as a compressed air storage tank, it may be possible to configure a power storage plant providing power at several thousand yen/kWh, which is less expensive than the power provided by chemical secondary batteries, such as lithium-ion batteries.[5)]

Rock-salt beds are widespread in North America, China, and Central and Eastern Europe. Therefore, Kobe Steel believes that the spread of compressed-air energy storage plants can contribute to the promotion and introduction of renewable energy in these regions.

Finally, we would like to express our gratitude to the Institute of Applied Energy and Waseda University, which adopted Kobe Steel's compressed-air energy storage plant as a demonstration apparatus and gave Kobe Steel a great deal of guidance and advice in connection with the verification test at Izu.

References

1) M. Toshima et al. Journal of the Japan Institute of Energy. 2016, Vol.95, No.3, pp.180-187.
2) M. Domoto et al. Clean Energy. December 2017 issue, pp.13-20.
3) M. Matsukuma. Reito (refrigeration). May 2017 issue, Vol. 92, No.1075, pp.351-356.
4) PJM website. https://www.pjm.com, (accessed 2018-01-24).
5) K Mongird et al. Energy Storage Technology and Cost Characterization Report. July 2019, pp.6.1-6.2.

This paper was originally written in January 2020

MIDREX® Process: Bridge to Ultra-low CO_2 Ironmaking

Dr. Vincent CHEVRIER[*1] · Lauren LORRAINE[*1] · Haruyasu MICHISHITA[*1]

[*1] Midrex Technologies, Inc.

Abstract

Midrex Technologies Inc. - a wholly owned subsidiary of Kobe Steel since 1983 - has been the market leader in direct reduction of iron for nearly 45 years. This success is based on a simple and efficient process, years of continuous innovations and improvements, the excellence of plant operators, and the support from Kobe Steel.

With the emphasis on reducing greenhouse gas emissions following the ratification of the Paris Agreement, direct reduction is the only commercially-proven process that can achieve significant reduction in CO_2 *emissions for the iron and steel industry today, using natural gas or liquified natural gas (LNG). The MIDREX* H_2™ *is an evolution of the MIDREX® Process that can produce iron with almost no* CO_2 *emissions; but it requires amounts of hydrogen that are not currently available from renewable sources today. This article describes the MIDREX® Process and significant improvements made over the last 50 years and offers a vision of ultra-low carbon ironmaking that can be realized in the hydrogen economy.*

Introduction

Midrex Technologies, Inc., which owns the process technology for direct reduced iron ore (the MIDREX Process), began operation of its first unit in Portland, Oregon, USA in 1969 and celebrated its 50th anniversary in 2019. Meanwhile, it became a wholly owned subsidiary of Kobe Steel in 1983 and achieved the milestone of a cumulative production of reduced iron (direct reduced iron, hereinafter referred to as "DRI") of 1 billion tonnes in 2018. In addition, the annual plant capacity was increased from 150,000 tonnes to 2.5 million tonnes (**Fig. 1**).

Most of the 90 plus plants hitherto constructed are still in operation. For example, the plant constructed in Hamburg, Germany in 1971 is the oldest one currently in operation. In 2018, this plant achieved a production capacity of 564,000 tonnes and an uptime of approximately 8,000 hours with its initial design production capacity of 400,000 tonnes.

The latest plant is Tosyali Algérie with an annual production capacity of 2.5 million tonnes. It was constructed near Oran, Algeria. Its first product was made in November 2018, and just eight months later, in July 2019, it set a world production record of 7,700 tonnes per day. In addition, a plant with a 2.5 million tonne annual capacity is under construction (as of July 2020) in Belara, Algeria, for Algerian Qatari Steel (AQS); and most recently, another plant with an annual production capacity of 1.6 million tonnes, is under construction in Toledo, Ohio, for Cleveland-Cliffs Inc.. Therefore, two new plants are scheduled to begin operation in 2020.

The greatest factor that has driven the expansion of the DRI market is the increasing utilization of recycled scrap in various places and the worldwide shift from the conventional ironmaking method with integrated blast furnaces to the method using electric furnaces. In order to maintain the quality of electric furnace steel made from scrap, it is necessary to use iron sources derived from ore (ore-based metallics: OBM) in combination. For these reasons,

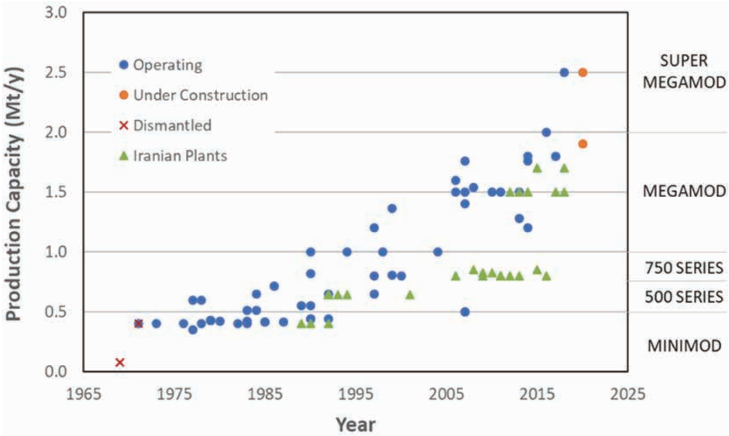

Fig. 1 Evolution of MIDREX® Module sizes over the last 50 years

the demand for DRI is increasing worldwide.

In the future, the market for DRI is expected to expand due to environmental concerns, since electric furnaces using scrap together with DRI reduced by using natural gas or hydrogen lead to CO_2 reduction.

1. DRI: Raw material for steelmaking adding value to products

DRI is a high-grade iron source derived from natural iron ore from which chemically bound oxygen has been removed without melting iron ore pellets or lump ore. Therefore, DRI consists of a high concentration of iron and little tramp elements such as copper, and nitrogen, which often adversely affect steel quality. In other words, DRI is said to be a raw material effective for diluting impurities contained in scrap. Hence, it is used in electric furnaces that produce high-quality steel products such as steel sheets for automotive bodies, deep-drawing steel, fine wire rods, special steel bars, forging steel bars, and seamless steel pipes.

DRI has been used most often in electric furnaces, but it has also been used in blast furnaces for many years. This is because DRI is mainly composed of reduced metallic iron, and when used in a blast furnace, it decreases the reduction burden in the furnace, which increases production volume and/or decreases coke consumption. For example, in the blast furnace at AK Steel in the United States, approximately 250 kg of DRI was used per tonne of molten iron.[1)]

2. Forms of DRI

DRI includes cold direct reduced iron (hereinafter referred to as "CDRI"), hot direct reduced iron (hereinafter referred to as "HDRI"), and hot briquetted iron (hereinafter referred to as "HBI") (**Fig. 2**), having favorable physical and chemical properties for use in electric furnaces, blast furnaces, and basic oxygen furnaces, respectively. A MIDREX Module constructed in the early days produced CDRI that had been cooled to around the ambient temperature after reduction and was used in an adjacent electric-furnace steel mill. As the advantages of using DRI prevailed, the demand for this high-grade iron source has grown worldwide, and Midrex Technologies Inc. has developed and commercialized two other forms of DRI, i.e., HDRI and HBI.

DRI at a high temperature after reduction has a lot of pores created by the oxygen removal and has the disadvantage that it generates heat and can catch fire when it comes into contact with air and is recombined with oxygen (reoxidation). Hence, it is compressed between a pair of rollers to produce HBI with a reduced pores rate. Therefore, HBI has an excellent reoxidation resistance, solves problems associated with long-term storage and marine transportation, and prevents a decrease in yield due to fines generation during handling. Having a form favorable for external sales, HBI is always available on the market with an established supply chain and is being produced in a place where the production cost is low and marine transportation is convenient.

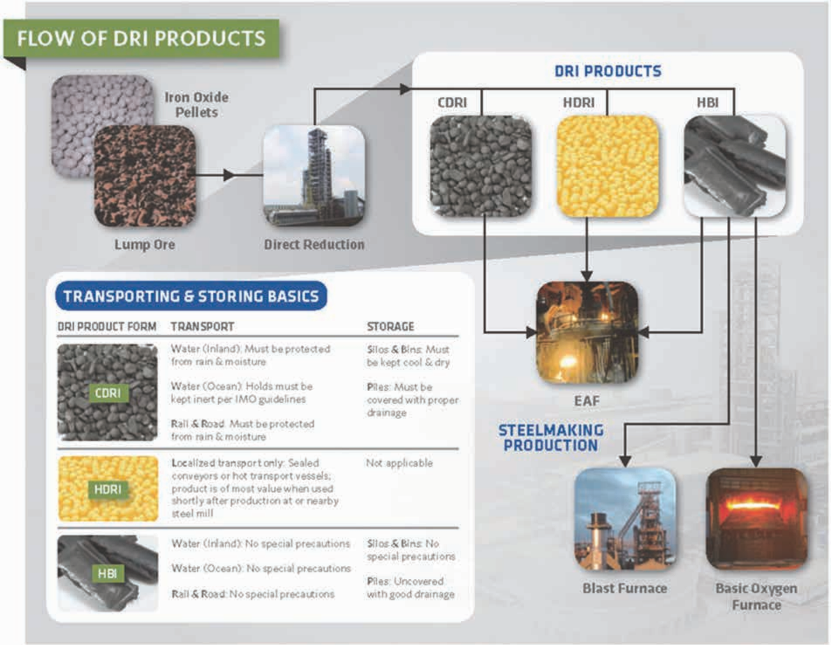

DRI PRODUCT FORM	TRANSPORT	STORAGE
CDRI	Water (Inland): Must be protected from rain & moisture Water (Ocean): Holds must be kept inert per IMO guidelines Rail & Road: Must be protected from rain & moisture	Silos & Bins: Must be kept cool & dry Piles: Must be covered with proper drainage
HDRI	Localized transport only: Sealed conveyors or hot transport vessels; product is of most value when used shortly after production at or nearby steel mill	Not applicable
HBI	Water (Inland): No special precautions Water (Ocean): No special precautions Rail & Road: No special precautions	Silos & Bins: No special precautions Piles: Uncovered with good drainage

Fig. 2 Description and use of DRI products

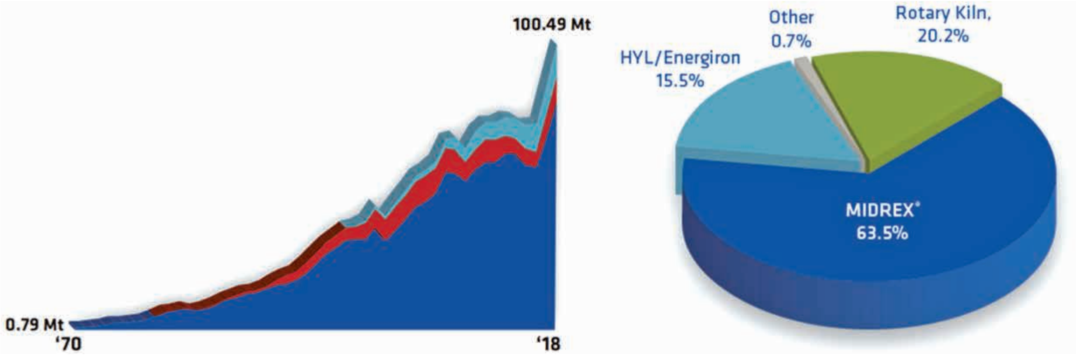

Fig. 3 Trends in world's annual DRI production[2)]

The plant for Cleveland-Cliffs Inc. mentioned above is a plant that produces HBI.

On the other hand, when the DRI produced by a MIDREX Module is used in an adjacent electric furnace shop, much of the energy required for melting in the electric furnace can be reduced by the use of the hot DRI, which has a temperature of 600℃ or higher after reduction. Therefore, Midrex Technologies Inc. has developed a technology to transport HDRI and charge it to an electric furnace. This has further enhanced the value of DRI. In the two latest plants in Algeria mentioned above, HDRI is produced and fed to an adjacent electric furnace.

Thus, the recent trends are the construction of a plant that produces HDRI adjacent to an electric furnace, and the construction of a large plant that produces HBI for external sales.

It should be noted that the term "DRI" referred to in this paper means comprehensive reduced iron products in all three product forms, CDRI, HDRI and HBI. This diversification of product forms in DRI also contributed to the increase in electric furnace production in the global steelmaking industry, and as shown in **Fig. 3**, the world DRI production in 2018 exceeded 100 million tonnes.[2)]

3. Overview of the MIDREX Process

Fig. 4 and **Fig. 5** show, respectively, the flowsheet for the standard MIDREX Process (MIDREX NG™) based on natural gas and an exterior photograph of the plant (Tosyali Algérie Steel Mill in Oran, Algeria). The MIDREX NG consists of two main units: a shaft furnace for reducing iron ore to metallic iron, and a reformer for producing the reducing gas required for the iron ore reduction in the shaft furnace.

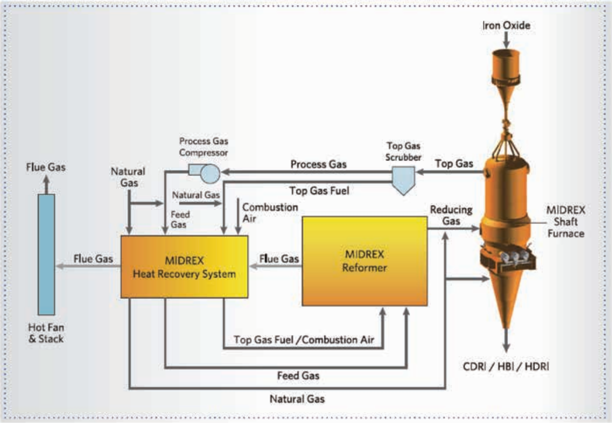

Fig. 4 MIDREX NG flowsheet

Fig. 5 Latest MIDREX NG plant: Tosyali in Oran, Algeria. (Reduction furnace in center with HDRI conveyor to EAF meltshop on left side.)

In the shaft furnace, reducing gas is countercurrently fed to the packed bed of iron-ore pellets or lump ore descending therein. The iron-ore pellets are heated up, reduced, and carburized very efficiently by the ascending gas. The iron ore is charged at the ambient temperature from the top of the shaft furnace and discharged from the bottom of the shaft furnace as CDRI or HDRI. The oxygen, which occupies approximately 30% (weight ratio) of the iron ore, is removed by the reactions with carbon monoxide (CO) and hydrogen (H_2) at high temperature in the shaft furnace, leaving carbon dioxide (CO_2) and water vapor (H_2O).

These solid-gas reactions are shown in **Fig. 6**. The reduction of iron ore by H_2 is an endothermic reaction, while the reduction by CO is an exothermic

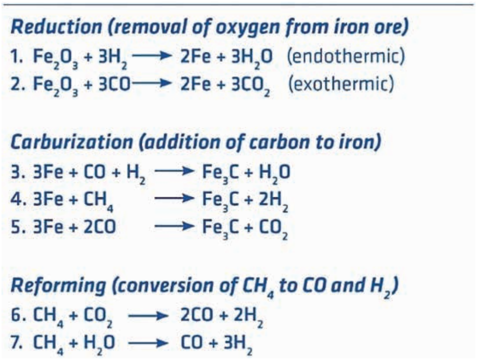

Reduction (removal of oxygen from iron ore)

1. $Fe_2O_3 + 3H_2 \longrightarrow 2Fe + 3H_2O$ (endothermic)
2. $Fe_2O_3 + 3CO \longrightarrow 2Fe + 3CO_2$ (exothermic)

Carburization (addition of carbon to iron)

3. $3Fe + CO + H_2 \longrightarrow Fe_3C + H_2O$
4. $3Fe + CH_4 \longrightarrow Fe_3C + 2H_2$
5. $3Fe + 2CO \longrightarrow Fe_3C + CO_2$

Reforming (conversion of CH_4 to CO and H_2)

6. $CH_4 + CO_2 \longrightarrow 2CO + 2H_2$
7. $CH_4 + H_2O \longrightarrow CO + 3H_2$

Fig. 6 Major chemical reactions in MIDREX Process

reaction. Furthermore, the carbon contained in DRI is produced by a chemical reaction with CO or methane (CH_4). Blowing natural gas from the bottom into the shaft furnace increases the amount of carbon content in the DRI and cools the DRI in a CDRI plant.

The post-reduction gas emitted from the top of the shaft furnace at 350-450℃ is cooled and dedusted. This gas contains CO and H_2 in addition to the products of reduction reaction, namely CO_2 and H_2O. Approximately two-thirds of it is recycled as reducing gas, and the rest is used as the heat source required for the reforming reaction. The recycled gas is sent to the MIDREX Reformer after natural gas has been added. The MIDREX Reformer has a structure in which a tube filled with a special nickel-based catalyst is housed in a refractory casing. As the gas passes through the tube, the oxidized compound (CO_2, H_2O) and methane are reacted by catalyst and reformed into CO and H_2. Other DRI production processes that use natural gas employ conventional steam reformers. On the other hand, the MIDREX Reformer, which uses CO_2, a reduction product, as the main reforming agent, can produce gas with a low H_2/CO ratio. Using this as the reducing gas of the shaft furnace enables the furnace interior to be stably maintained at a high temperature, thanks to the heat associated with the reduction reaction with CO, which ensures stable operation and the production of high-quality DRI.

The MIDREX Process uses natural gas efficiently for the following three purposes:

(1) as the raw material of CO and H_2 required for the reduction of iron ore,
(2) as a heat source for the shaft furnace and reformer, and
(3) as an agent to enhance cooling and carburizing of the direct reduced iron.

In addition, the MIDREX Reformer has the equipment for recovering the sensible heat of exhaust gas for preheating reformer feed gas, combustion air, natural gas, etc., to realize high thermal efficiency.

Many years of experience have shown that the MIDREX Process is flexible with respect to the applicable iron ore and reducing gas. As for iron ore, it is possible to charge a high volume of lump ore, depending on the brand, in addition to iron ore pellets from all over the world. The MIDREX Process has an experience of using various reducing gases with H_2/CO = 0.5 to 3.5 in commercial plants, such as COREX® gas, coal gas, coke furnace gas and steam reformer gas. Although in a small scale, Midrex Technologies Inc. has the experience of operating a pilot plant built at its R&D center, from the late 1970s to the mid-1980s, and using reducing gas with H_2/CO = 4.2 at the maximum.

The main reason that the MIDREX Process has expanded in the DRI production process is its simplicity. For example, the process control can be easily done by performing the iron ore reduction and gas reforming in separate reactor vessels. In addition, the MIDREX Process employs low operating pressure, which results in stable and easy operation of the plant. As a result, many of the plants have achieved an uptime of over 8,000 hours per year.

4. Evolution of MIDREX Process by continuing innovation

The MIDREX Process has undergone many improvements, large and small, from the time that the first MIDREX Module in Portland, Oregon began operation in 1969 until the latest Algerian plant was launched in 2020. Innovative ideas have been adopted according to Kobe Steel's technical development assistance to Midrex Technologies Inc., a member of the Kobe Steel Group, feedback from the plant operations, and collaboration with technology partners. Thanks to this, the MIDREX Process has evolved into the most reliable, efficient, and environmentally friendly process to reduce the iron ore.

A recent article from "Direct from Midrex"[3)] provides a comprehensive list of innovative technologies that have been used in the MIDREX Process. Six of them are exemplified below:

- Significant improvement in energy efficiency by enhanced heat recovery equipment.
- Preventing clustering and realizing high-temperature operation of the shaft furnace by coating the surfaces of iron ore pellets.
- Realizing high-temperature operation of the shaft furnace by blowing oxygen into reducing gas.
- Hot briquetting and cooling technologies to improve the strength, reoxidation resistance and

yield of the HBI.

- Reducing melting energy by directly charging HDRI to the electric furnace (HOTLINK® Note 1)) and thereby realizing improved productivity and cost reduction of the electric furnace.
- Expansion of plant scale by applying a large shaft furnace (MEGAMOD® Note 2)) (annual production of 400,000 tonnes in the 1970s → current annual production of 2.5 million tonnes)

Recently, the Midrex R&D team and Kobe Steel have collaborated to develop the following new technologies:

- Performance improvement technology for the MIDREX Reformer
  (1) Eleven-inch large diameter tube.
  (2) MA-1 alloy to suppress deformation at high temperature.
  (3) New catalyst (R7RWH, R17) that reduces pressure loss.
  (4) New burner system that reduces NOx emissions.
- Adjustable Carbon Technology (ACT™)
  A system for controlling HDRI discharge temperature and carbon content individually by blowing in a mixed gas of CO and natural gas at the bottom of the shaft furnace.
- DRIPAX and Expert system
  Computer tools for helping plant operators and engineers optimize the operations.
- MidrexConnect™
  Provision of services to remotely monitor plant equipment and analyze operation data. It accesses plant data in real time from Midrex headquarters via direct secured link to check process variables that affect plant performance and the impact on the entire production process. The information that the plant operator must immediately determine and take action upon is conveyed to the plant.[4)]
- Integrated Plant Solutions (IPS)
  Provision of a comprehensive solution by which the plant equipment and operation are integrally analyzed to improve the utilization rate and productivity. Midrex Technologies Inc. currently provides water treatment facility management services to multiple plants.
- MIDREX H_2
  MIDREX H_2 will be explained in detail in Section 5.4.

In the last decade, Midrex Technologies Inc. worked with its collaboration partners to construct and operate nine plants. In addition, two more plants are currently under construction or being commissioned. All these new plants employ all or most of the technologies listed above. This is the achievement of Midrex Technologies Inc., which has developed innovative and meaningful products on the basis of various ideas.

The latest Algerian plant, mentioned above, with an annual production of 2.5 million tonnes, mainly produces HDRI, in which maximum productivity and minimum energy consumption are realized by continuous feeding to the adjacent electric furnace using a hot transfer conveyor. In addition, the plants constructed by Midrex Technologies Inc. adapt new technologies, such as a newly designed reformer with 8 rows of large diameter M1 alloy tubes, two-point gas feed to the reducing gas header, and 2 parallel reformer exhaust gas hot fans.

The 1.6 million tonne HBI plant under construction for Cleveland-Cliffs Inc. is the first plant capable of regulating HBI carbon content by adopting the ACT technology mentioned above.

5. Steps taken toward CO_2-free ironmaking by MIDREX Process

5.1 Iron and steel industry CO_2 emissions

The iron and steel industry is one of the major greenhouse gas emitters, accounting for approximately 7-9% of the total amount of emissions, especially because its ironmaking process relies heavily on coal. Approximately 70% of the crude steel produced in the world is blast furnace pig iron refined by converters.[5)] Ironmaking in blast furnaces uses coke and coal as energy sources and reductants. Therefore, the blast furnace-basic oxygen furnace process emits a large amount of CO_2, 1.6 to 2.0 t/t-steel.

The MIDREX Process, on the other hand, uses natural gas as its energy source and reductant, enabling ironmaking with lower CO_2 emissions than blast furnaces. The following sections outline the steps to reduce the amount of CO_2 emissions by using the MIDREX Process.

5.2 Replacement of blast furnace with MIDREX NG Process

As mentioned above, the MIDREX NG Process, which uses natural gas, enables ironmaking with a low amount of CO_2 emissions. When this process is combined with an electric furnace, the amount

---

Note 1) HOTLINK is a registered trademark of Midrex Technologies Inc.

Note 2) MEGAMOD a registered trademark of Midrex Technologies Inc.

of CO_2 emissions can be 1.1-1.2 t/t-steel,[6)] which is the lowest among the commercial processes that produce crude steel from iron ore. In other words, significant CO_2 reduction is possible by replacing the blast furnace– basic oxygen furnace process with the MIDREX NG–electric furnace process.

Furthermore, if CO_2 removal equipment is installed in the MIDREX NG Process and the removed CO_2 is stored deep in the ground (Carbon Capture and Storage, CCS) or used as a new product or energy (Carbon Capture and Utilization, CCU), the amount of CO_2 emissions can be reduced to approximately 1/3 of that of the blast furnace– basic oxygen furnace process.

The MIDREX NG Process has plenty of experience, including the use of CO_2 removal equipment, and by switching to this process, the amount of CO_2 emissions can be effectively and significantly reduced without taking any technical risks.

5.3 Partial replacement with hydrogen in MIDREX NG Process

The ultimate way to dramatically reduce the CO_2 emitted by the MIDREX Process is to use hydrogen produced from renewable energy (hereinafter referred to as "green hydrogen") instead of the natural gas used for fuel and reductant.

The first step is to replace some of the natural gas with green hydrogen when green hydrogen becomes available in an existing MIDREX NG Plant. **Fig. 7** depicts the flowsheet for adding hydrogen to the MIDREX NG Process. In the case of Fig. 7 (a), it is possible to replace up to 20 to 30% of natural gas with hydrogen without modifying the equipment. In a DR plant with an annual production capacity of 2 million tonnes, for example, approximately 20,000 Nm^3/h of natural gas, which accounts for approximately 30% of the total natural gas consumption, can be replaced by 60,000 Nm^3/h of hydrogen. For replacing even more natural gas, steam needs to be fed to the MIDREX Reformer. This steam can be produced separately in a boiler, or can be other steam sources available at the steel mills. Fig. 7 (b) is the flowsheet for this case. It is possible to make these steam-feeding modifications to an existing MIDREX NG Plant. Also, a newly constructed plant can be designed considering the future modifications.

If the amount of hydrogen available fluctuates daily or seasonally in the course of infrastructure changing from a carbon economy to a hydrogen economy, the MIDREX Process can flexibly change the energy source in accordance with the situation at that time. Hydrogen may also be produced within a plant site or be received from external producer.

5.4 MIDREX H_2 Process (based on 100% hydrogen)

Fig. 8 depicts the flowsheet of the MIDREX H_2 Process. Fig. 8 (a) shows the case where externally produced hydrogen is fed, and Fig. 8 (b) shows the case where the hydrogen production equipment is incorporated in the process. The MIDREX Reformer is no longer needed; only a gas heater is needed for heating up hydrogen to the required temperature. When an existing MIDREX NG Plant is switched to a MIDREX H_2 Plant, the MIDREX Reformer can easily be converted to a gas heater because the endothermic reforming reaction is eliminated, decreasing the heat load. In a newly constructed MIDREX H_2 Plant, the equipment specifications may be tailored to only heating up hydrogen. For the shaft furnace, by means of process model calculations and laboratory experiments it has been verified to be able to produce DRI by applying 100% hydrogen without changing the existing furnace design.

The hydrogen consumption rate in these

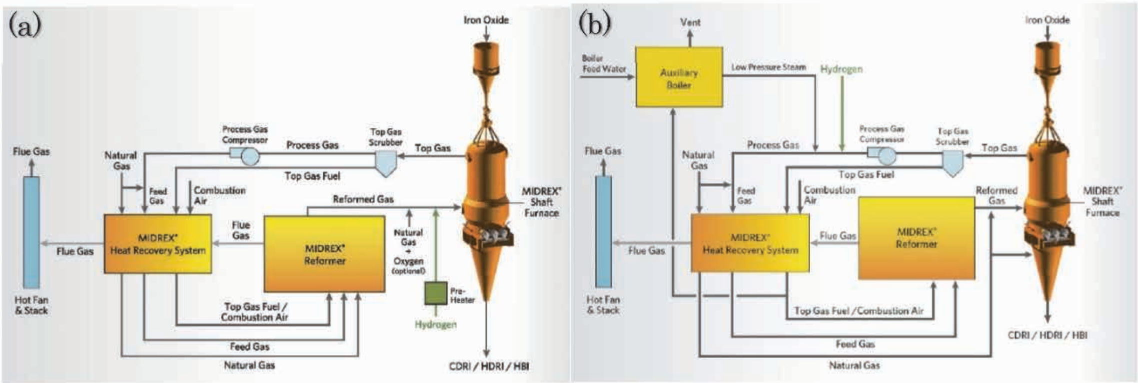

Fig. 7 MIDREX NG Process with hydrogen addition:
(a) less than 20-30% of natural gas displacement, (b) more than 30% natural gas displacement

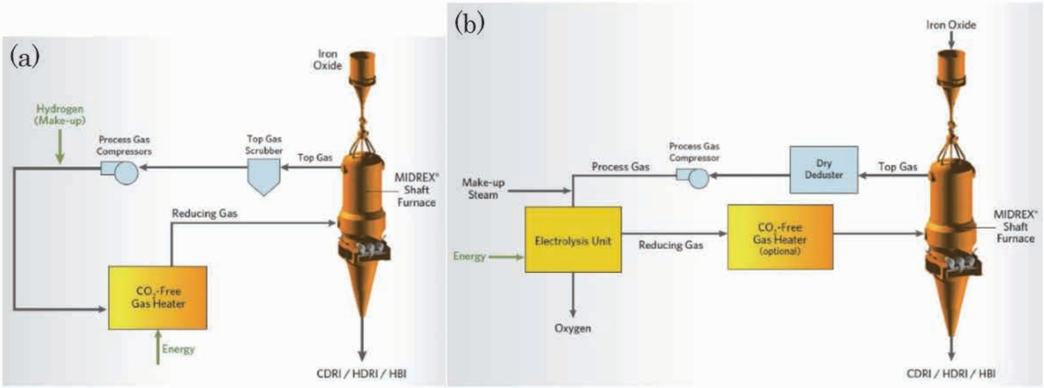

Fig. 8 MIDREX H_2 Process: (a) hydrogen supplied over-the-fence, (b) integrated hydrogen generation

flowsheets is approximately 650 Nm^3/ t-DRI. As the energy source for the reducing gas heater, hydrogen up to 150 Nm^3/ t-DRI, or another low CO_2 load heat source, such as waste heat, electricity, or natural gas, is required. By combining the MIDREX H_2 Process with an electric furnace, it is possible to reduce CO_2 emissions by 80% or more compared with the case where crude steel is produced by the blast furnace–basic oxygen furnace process, although the amount of reduction varies depending on the CO_2 load of the electric power used.

6. Challenges faced by hydrogen ironmaking

This section describes the challenges in the partial replacement with hydrogen in the MIDREX NG Process described in the previous section, and in the steps towards using 100% hydrogen in the MIDREX H_2 Process. As shown by the chemical reaction formula in Fig. 6, a large amount of hydrogen has already been used for iron ore reduction in the current MIDREX NG Process based on natural gas. Therefore, the partial replacement with hydrogen in the MIDREX NG Process or the MIDREX H_2 Process should be called an evolution from the MIDREX NG Process rather than a breakthrough in technology.

As can be seen, the hurdle to MIDREX H_2 is not high, but there are some challenges. One of them is the temperature in the shaft furnace. The increase in hydrogen in reducing gas causes a transition from carbon-monoxide reduction (Reaction 2 in Fig. 6), which is exothermic, to hydrogen reduction (Reaction 1 in Fig. 6), which is endothermic. This affects the heat balance in the shaft furnace, and it is necessary to increase the amount of heat supplied to the shaft furnace. The MIDREX H_2 allows several methods of responding in accordance with the situation of each project.

Another challenge exists in the carbon content of product DRI. Reduction with 100% hydrogen results in 0% carbon content in the DRI. The most common operations in electric furnaces nowadays actively exploit carbonaceous materials such as coke breeze or the carbon contained in ore-based iron sources (OBM) such as DRI and pig iron. This is because the carbon lowers the melting point of iron and is also required to reduce iron oxide remaining in the DRI. There also are advantages in combusting carbon with oxygen blown, to generate a great amount of energy and shorten the melting time. That is, without carbon, the efficiency of the electric furnace would be significantly reduced. Therefore, it is necessary to optimize carbon concentration in DRI for the electric furnace and DR plant as a whole and change the operating conditions accordingly, considering many factors including the cost of CO_2 emissions. The utilization efficiency of carbon contained in DRI is higher than that of carbonaceous materials such as coke breeze. Therefore, it may be necessary to add some carbon to the DRI in some DR plants. In such cases, it is possible to obtain 1.4% carbon in DRI, by adding the natural gas of 50 Nm^3/ tonne, for example.[7)]

The biggest challenge in realizing hydrogen ironmaking is to reduce the cost of green hydrogen and to stabilize its supply. Globally, most hydrogen is currently produced from fossil fuels through steam reformers, whereas green hydrogen is produced by the electrolysis of water, in which CO_2-free electricity is used. The water electrolysis technology is not new, and much development has been made in electrolytic cells. However, a large amount of electric power is required regardless of which technology is used [Note 3)], and electricity accounts for most of the operating cost of electrolytic cells. To replace the natural gas at the current price, the electricity unit cost must decrease to around \$0.01/kWh to be economically viable. Furthermore, even with the currently established technology, it

---

[Note 3)] The amount of hydrogen that can be produced by 1 MWh of electricity is approximately 200 Nm^3 (18 kg).

is not possible to supply the required amount of hydrogen to DR plant. The most ambitious project recently announced in Europe has a plan to produce hydrogen by 100 MW of alkaline electrolysis.[8] This scale, however, must be increased by a factor of 6 to 8 to cover the hydrogen required for one MIDREX Module. Furthermore, even if the electricity unit cost comes down to $0.01/kWh, the equipment cost of electrolytic cells will need to be reduced to 1/3 to 1/4 of the current equipment cost in order to make the price of product hydrogen match the price of hydrogen produced from fossil fuels. Development aiming to increase the scale of electrolytic cells is also under way, but it seems that it will still take time to be economically viable even if the equipment costs are reduced by increasing the scale.

In order for hydrogen to be stably supplied and the hydrogen economy to be realized, it is necessary to work on the challenges of hydrogen infrastructure such as storage and transportation of hydrogen, in addition to the challenge of hydrogen production cost.

Yet another challenge in realizing hydrogen economy is power generation. For example, suppose that the current amount of crude steel in Japan is produced by feeding scrap and the DRI produced by MIDREX H_2 to an electric furnace at a ratio of 50:50. In this case, the DR plant alone would require approximately 25 GW of green electric power, corresponding to 300,000 ha of solar panels, 40,000 units of wind turbines (7,500 ha of land), or 20 nuclear power plants. Such a huge amount of green electric power is required, and this is considered as a challenge to be addressed at the national level.

7. Demonstration plant of MIDREX H_2 Process

In September 2019, ArcelorMittal, S.A. announced that it would work with Midrex Technologies Inc. to construct a demonstration plant for producing steel using hydrogen in Hamburg, Germany. The purpose of this project is to demonstrate that DRI produced using only hydrogen as a reductant can be used in an electric furnace to produce molten steel. In this demonstration plant, hydrogen contained in the furnace top gas of an existing MIDREX Module that uses natural gas as a reductant is recovered and is used to produce 100,000 tonnes of DRI annually. As future scheme, it is planned to produce a part or all of the hydrogen based on renewable energy. In this project, both companies plan to tackle technological challenges, including the physical characteristics and melting properties of DRI produced by hydrogen reduction.

Conclusions

The year 2019 marked the 50th anniversary of the birth of the MIDREX Process. At the same time, 37 years have passed since Midrex Technologies Inc. joined the Kobe Steel group. Continuing to improve and modify this simple and excellent process has enhanced its efficiency and has made its evolution in line with the market, which has led to the success of the business to date. Against the backdrop of recent trends in the iron and steel industry, the role of the MIDREX Process is expected to become greater than ever as a technology to produce high-grade iron source called DRI, which can meet the high demand for steel quality and at the same time greatly reduce greenhouse gas emissions.

The MIDREX Process is a well-established technology with a wealth of experience. It is considered to be the most reliable technology, whose introduction can not only reduce the amount of greenhouse gas emissions immediately, but also realize the even more significant reduction required in the future.

References

1) Blast Furnace Roundup 2002. Iron and Steelmaker. August 2002.
2) Midrex Technologies, Inc., 2018 World Direct Reduction Statistics.
3) J. Kopfle et al., DIRECT FROM MIDREX 2nd QUARTER 2019.
4) C. Cotton, DIRECT FROM MIDREX 1st QUARTER 2019.
5) World Steel Association. FACTSHEET Steel and raw materials 2019.
6) Treatise on Process Metallurgy, Volume 3: Industrial Processes, Elsevier , 2013, p.170.
7) V. Chevrier et al., MIDREX H_2^{TM}: Ultimate Low CO_2 Ironmaking and its place in the new Hydrogen Economy. AISTecH 2018, conference, Philadelphia, PA.
8) REUTERS. "German energy grids say plans ready for 100 MW hydrogen plant". February 11, 2019, https://uk.reuters.com/article/us-amprion-opengrideurope-hydrogen/german-energy-grids-say-plans-ready-for-100mw-hydrogenplant-idUKKCN1Q01S4, (accessed 2020-02-10).

Destruction of Old or Abandoned Chemical Weapons by Controlled Detonation

Ryusuke KITAMURA*1

*1 Project Department, CWD Project Center, Engineering Business

Abstract

While a large part of the world's stockpile of chemical weapons has been destroyed already, the destruction of non-stockpiled chemical weapons will continue in the future. Dismantling non-stockpiled chemical munitions such as old/abandoned chemical weapons is a very difficult task and involves a high risk of accidents. Controlled detonation is suitable for old/abandoned chemical weapons, since it can destroy chemical munitions without prior dismantling. In controlled detonation, the shells of chemical munitions are fragmented, and the chemical agents and explosives filling the shells are destroyed by the shock wave, as well as by the high-pressure and high-temperature environment produced by the detonation of the donor charge. A detonation chamber and a controlled detonation system, whose main component is the detonation chamber, have been developed and used in destroying many old/abandoned chemical weapons in and out of Japan since 2004. The controlled detonation system and destruction of chemical weapons are outlined in this report.

Introduction

Chemical weapons were first used in 1915 during World War I. Since then, many countries have developed, produced, retained, and used chemical weapons. In areas that were battlefields in the past, they are still found as unexploded munitions. In addition, chemical weapons, dumped in the territory of a country by the country itself or abandoned by another country, have been found in the ground as well as in water, and this has become a problem, not only for the safety and health of the residents, but also for the local environment and economic activities.

Following the entry into force of the 1997 Chemical Weapons Convention, which obliges Japan to destroy abandoned chemical weapons in China, the Engineering Business of Kobe Steel conducted technical research and development aimed at taking part in this destruction project. Since receiving an order for the treatment of the chemical munitions left by the old Japanese armed forces and found in Lake Kussharo (Hokkaido) in 2000, the company has been performing chemical weapons destruction in various ways. In particular, the company has detoxified many old or abandoned chemical weapons using a controlled detonation system developed in-house, called DAVINCH™ Note), and has also provided its customers with destruction facilities which utilize the controlled detonation system.

This article introduces Kobe Steel's DAVINCH™ system and also outlines chemical weapons and chemical weapon destruction performed by the DAVINCH™ system.

1. Chemical weapons

1.1 What are chemical weapons?

In a broad sense, chemical weapons are munitions for killing or incapacitating humans with chemical substances. As mentioned above, modern chemical substances with high toxicity were first used as weapons of mass destruction during World War I. In early days, chlorine gas was simply put on the wind and flowed toward the enemy; but soon, projectiles filled with toxic chemical substances (chemical agents) were fired with artillery, for example, to efficiently deliver them to the enemy. The projectile also contained built-in explosives such as a burster for opening the munitions shell to scatter and evaporate chemical agents.

After that, each country competed to develop chemical agents and the means to deliver them to the enemy (projectiles, bombs dropped from aircraft, etc.), and chemical weapons diversified rapidly. Famous chemical agents such as phosgene (molecular formula, $COCl_2$; NATO code, CG) and mustard gas (molecular formula, $(CH_2CH_2Cl)_2S$; NATO code, HD) had already been used during World War I. In addition, during World War II, the old Japanese armed forces manufactured, in large quantities, a mixture of HD and lewisite (molecular formula: $CHCl = CHAsCl_2$, NATO code: L), called a Kii (yellow) agent, and diphenylcyanoarsine (molecular formula: $(C_6H_5)_2AsCN$, NATO code: DC) and/or diphenylchloroarsine (molecular formula: $(C_6H_5)_2AsCl$, NATO code: DA), called Aka (red) agent. During the Cold War after World War II, sarin and VX, which have stronger toxicity, were also manufactured and stockpiled in large quantities in the former Soviet Union, the United States, and other countries.

Note) DAVINCH is a registered trademark of Kobe Steel, Ltd.

1.2 Chemical Weapons Convention

The Convention on the Prohibition of the Development, Production, Stockpiling and Use of Chemical Weapons and on their Destruction (hereinafter referred to as the "Chemical Weapons Convention") was adopted in 1992 and entered into force in 1997. There are 193 states parties to the convention, and Japan signed in 1993 and ratified it in 1995.

The Chemical Weapons Convention stipulates that:

- the states parties shall not develop, produce, acquire, retain, transfer, or use chemical weapons;
- the states parties shall declare chemical weapons to retain and the production facilities of the chemical weapons and, in principle, destroy them within 10 years after the convention comes into force (by April 2007, at the time of entry into force);
- the organization for the prohibition of chemical weapons (OPCW) shall be established as an organization to verify compliance with the convention through inspections, etc., in response to reports from states parties.[1]

1.3 Stockpile vs. non-stockpile

Chemical weapons that are stocked without being used are called "stockpile chemical weapons." After the entry into force of the Chemical Weapons Convention, the destruction of stockpile chemical weapons has been promoted by the states parties to it that retained chemical weapons. To date, approximately 72,000 tonnes of chemical agents have been declared to OPCW worldwide, of which approximately 70,000 tonnes (more than 97%) have been destroyed.

On the other hand, chemical weapons other than those stockpiled, e.g., munitions that were dumped underground or underwater and unexploded munitions, are called non-stockpile chemical weapons. Many non-stockpile chemical weapons remain unrevealed, making it hard to progress with their destruction.

1.4 Old chemical weapons and abandoned chemical weapons

The Chemical Weapons Convention also stipulates that the states parties shall destroy old chemical weapons in their own countries and chemical weapons abandoned in the territory of other states parties (hereinafter referred to as "abandoned chemical weapons").

Fig. 1 Examples of old chemical weapons

Old chemical weapons are defined as those produced before 1925, or those produced between 1925 and 1946 that have deteriorated to such an extent that they can no longer be used as chemical weapons.[1] Corresponding to this are the chemical weapons used by the old Japanese armed forces, found in Japan, and the chemical weapons used during World War I and found in Belgium and France (**Fig. 1**).

Abandoned chemical weapons are defined as chemical weapons abandoned by a state after January 1st, 1925 in the territory of another state without the consent of the latter.[1] The chemical weapons used by the old Japanese armed forces and found in China correspond to this.

These old or abandoned chemical weapons are most often found as non-stockpile weapons.

2. Treatment of chemical weapons

2.1 Various treatment methods

In the past, when chemical weapons that had become unexploded munitions, weapons of defeated nations and the like were to be destroyed, they were often dumped in the ocean. However, with the international ban on marine dumping, as well as the Chemical Weapons Convention having entered into force, the nations that retain large amounts of stockpiled chemical weapons are obliged to destroy them in a short period of time and, as a result, various methods of destruction have been developed. The main ones include neutralization, incineration, and detonation.

The neutralization is a treatment method in which chemical agents of chemical weapons are mixed with reagents in a reactor so as to be decomposed by chemical reactions. Incineration is a method for decomposing chemical agents by burning them in high-temperature incineration furnaces. These two methods are suitable for the mass treatment of each chemical agent alone. Hence, they have been used in many countries to destroy stockpiled chemical agents stored in tanks and the like. In the United States, mass incineration treatments with liquid incinerators have been carried out at most facilities treating chemical weapons since 1990. Recently, Syrian chemical weapons have been neutralized on board a U.S. vessel on the Mediterranean Sea. Kobe Steel also has experience in neutralizing chemical agents left by the old Japanese armed forces at Lake Kussharo, Hokkaido (2000) and Samukawa, Kanagawa Prefecture (2004).

On the other hand, dismantling chemical projectiles, bombs, etc., to separate chemical agents from explosives for individual treatment carries the double risk of exposure to the chemical agents and detonations of the explosives. Furthermore, non-stockpiled chemical weapons left under the ground or in the ocean for a long period of time are difficult to dismantle because of changes such as the corrosion and deformation of the projectiles.

2.2 Detonation treatment

The detonation treatment, in which munitions are detonated to destroy any chemical agent and explosives contained therein, is suitable for treating non-stockpiled chemical munitions such as old or abandoned chemical weapons.

There are two types of detonation treatments, i.e., static detonation and controlled detonation. In static detonation, chemical munitions are heated in a detonation chamber, in which the chemical agents are pyrolyzed. Furthermore, the explosives, such as the burster, are ignited and exploded, and the pyrolysis gas, released from the munitions shell, and the vapor of undecomposed chemical agents are decomposed and removed by a gas treatment device such as a secondary combustion furnace in the subsequent stage. The detonation chamber is always in communication with the subsequent gas treating device and, therefore, there are stringent restrictions on the amount of explosive in chemical ammunition that can be charged at one time, due to the explosion resistance performance. On the other hand, this method is suitable for the mass treatment of relatively small munitions because the throughput can be increased by increasing the charging frequency of the munitions.

In controlled detonation, donor charges are attached to each piece of chemical ammunition, which is subjected to detonation blasting in a sealed explosion-resistant steel container (detonation chamber) so as to destroy the energetic materials and chemical agents. The treatment in a chamber with high explosion resistance offers advantages including the fact that large-sized munitions can be treated, and that the batch treatment facilitates the checking of the destruction of each piece of chemical ammunition and there are measures for dealing with any abnormality that may occur. In addition, by increasing the size and strength of the detonation chamber, the explosive quantity that can be treated at one time can be increased so as to treat a large amount of munitions.

Kobe Steel had the experience, in 2000, at Lake Kussharo, of cutting a chemical bomb, neutralizing its chemical agent, and detonating the energetic materials. After that, the company continued the development of the detonation chamber, etc., applying the manufacturing technology for pressure vessels, and put into practical use the DAVINCH™ system that allows controlled detonation without cutting chemical munitions.

3. Controlled detonation

3.1 DAVINCH™ system

The DAVINCH™ (Detonation of Ammunition in a Vacuum Integrated Chamber) is Kobe Steel's controlled detonation system. Its treatment process is outlined in **Fig. 2** and **Fig. 3**. A donor charge is attached to each piece of chemical ammunition, which is placed in a detonation chamber and the chamber is then depressurized with a vacuum pump. After the addition of an appropriate amount of oxygen, the valve is closed to completely seal the chamber. Subsequently, the donor charge is initiated by remote control so as to detonate the chemical munitions. The sealed detonation chamber contains the pressure of the explosion and the generated gas, and even if the undecomposed chemical agent remains, it will not leak to the environment. The detonation under reduced pressure alleviates the impact load on the detonation chamber and extends its fatigue life, while decreasing noise and vibration.

After the detonation, detonation product gas (offgas) containing a high concentration of hydrogen and carbon monoxide, as well as solid residue, such as shell fragments and dust, remains in the detonation chamber. Then, the valve in the pipe connecting the detonation chamber and the offgas treatment system is opened, and the offgas is sent from the detonation chamber to the offgas treatment system by a vacuum pump. The offgas treatment system not only removes dust in the offgas, but also oxidizes the above-mentioned

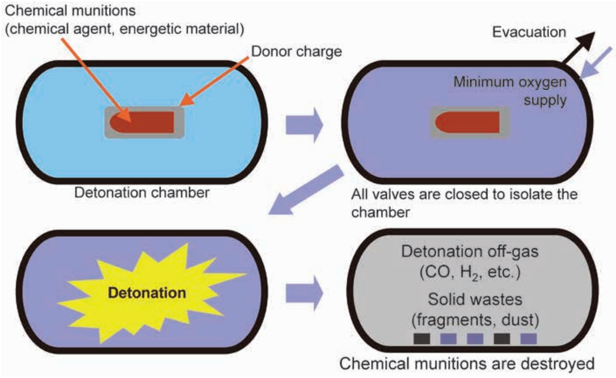

Fig. 2 Destruction process of DAVINCH™ system-(1): detonation

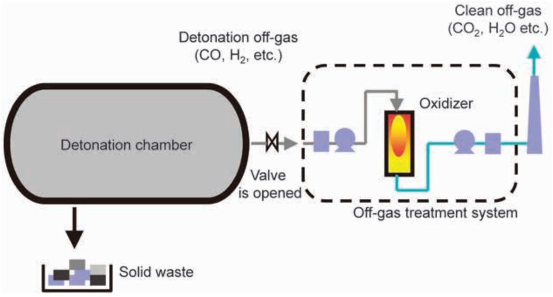

Fig. 3 Destruction process of DAVINCH™ system-(2): off-gas treatment

combustible components such as hydrogen and carbon monoxide. Furthermore, it removes acid gas and the like to convert the gas into harmless treated waste gas containing carbon dioxide, water vapor, nitrogen, etc., and releases the gas into the atmosphere through an activated carbon filter in case a trace of the chemical agent still remains.

3.2 Destruction of chemical munitions by detonation

The pressure and temperature generated by the detonation of explosives reach several GPa and several thousand K, respectively, in an extremely short period of time. When the donor charge is initiated, the shock wave generated by the detonation propagates to the chemical agent inside the chemical munitions through the munitions shell, and some of the chemical bonds of the chemical agent molecule are broken by the shock wave.[2)] Soon, tens to hundreds of micro-seconds after the detonation, the shell of the chemical munitions is fragmented, and when it comes into contact with the products of detonation at high temperature and high pressure, the chemical agents undergo various chemical reactions. Furthermore, they are decomposed almost completely by pyrolysis and reaction with oxygen in the atmosphere at a high temperature, the atmosphere lasting for a longer period of time (approximately 1 second).

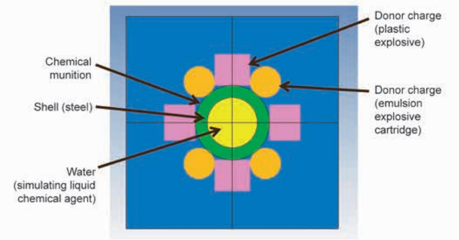

(1)Before detonation (simulation model, cross section of chemical munition with donor charge)

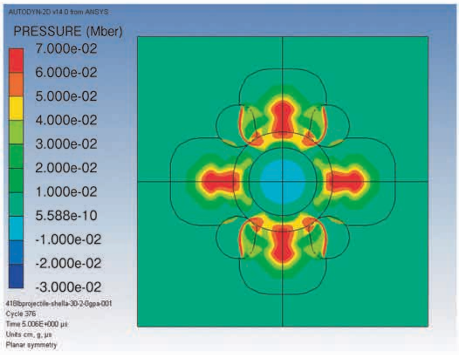

(2) Pressure contour at 5μs after detonation

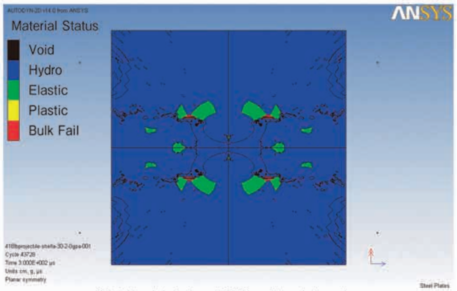

(3) Material status at 300μs after detonation

Fig. 4 Numerical simulation of behavior of a piece of chemical ammunition in destruction by detonation

Numerical analysis was performed on the behavior of a piece of chemical ammunition during detonation treatment. An example is shown in **Fig. 4**. Fig. 4 (1) depicts the simulation model. This figure shows the state in which a plastic explosive and a cartridge-filled emulsion explosive are attached as donor charges to the chemical munitions before detonation. Fig. 4 (2) shows the pressure contour diagram of the cross section of the piece of ammunition approximately 5 μs after the initiation of the donor charges, and it can be seen that the shock wave propagates in the munitions shell. The munitions shell is scattered in pieces 300 μs after the ignition (Fig. 4 (3)).

The burster is also initiated by the shock wave transmitted through the munitions shell and is consumed. In other words, the detonation using donor charge completes destruction by breaking chemical munitions, while detoxifying the chemical agents and explosives that have been the sources of danger.

Fig. 5 Detonation chamber delivered to Poelkapelle, Belgium

3.3 Detonation chamber

Fig. 5 shows an example of the detonation chamber. A detonation chamber is a steel container with hemispherical or semi-elliptical heads attached to the both ends of a cylindrical shell, in which one end of the container opens as a lid. The lid and body are sealed by fastening the flanges with hydraulically driven clamps. The detonation chamber has a double shell structure, in which the inner chamber protects the outer chamber from the fragments of the munitions shell that scatter during detonation, and the outer chamber has the role of containing the detonation pressure and gas. The inner chamber is replaced when the damage caused by the fragments exceeds its limit. The outer chamber is used while its remaining life is predicted by the monitoring of fatigue damage through the measurement of strain during detonation.

4. Achievements of controlled detonation by DAVINCH^{TM} system

4.1 Port of Kanda

Chemical munitions of the old Japanese armed forces during World War II, filled with aka (red) agent and kii (yellow) agent, were found on the seabed of the port of Kanda in Fukuoka prefecture. In response, Kobe Steel lifted and recovered about 3,000 of these chemical munitions from 2004 to 2013 and destroyed them with the DAVINCH^{TM} system. In 2017, another object suspected of being chemical ammunition was discovered in the same area again, and Kobe Steel also lifted and recovered and destroyed it from 2018 to early 2019 with the DAVINCH^{TM} system.

4.2 Belgium

In Belgium, which was a site of fierce battles during World War I, more than 200 tonnes of unexploded munitions are still discovered and recovered every year, about 5% of which are chemical munitions. The Belgian Ministry of Defense dismantled the chemical munitions for treatment but decided to use the DAVINCH^{TM} system for the treatment of munitions that are difficult to dismantle.

Kobe Steel delivered the DAVINCH^{TM} facility to the Belgian military base in Poelkapelle in the western part of the country (Fig. 5), and in 2008, the Belgian force began destruction using the facility. By the end of 2018, they had destroyed a total of about 13,700 munitions including approximately 4,400 chemical munitions, mainly filled with DC or DA, and 9,300 conventional munitions which include smoke agent containing arsenic compounds. The destruction is still ongoing.

4.3 France

In France, where many unexploded munitions of World War I are found, as in the case of Belgium, the Ministry of Defense is proceeding with a project, named SECOIA, using a facility for the destruction of old chemical weapons at the Mailly-le-camp military site. The DAVINCH^{TM} system has been adopted in the center of SECOIA facility; Kobe Steel has received an order from the French prime contractor and delivered the system. Currently, the prime contractor is preparing for the start of the destruction operation.

4.4 Destruction of abandoned chemical weapons in China

In China, abandoned chemical weapons left by the old Japanese armed forces during World War II have been found in various places, and the Japanese government has been destroying them. Since 2010, Kobe Steel has been conducting destruction in Nanjing, Wuhan, Shijiazhuang, and Harbin using mobile DAVINCH^{TM} systems. In addition, since 2014, treatment has been implemented by a fixed DAVINCH^{TM} system in Haerbaling, Jilin Province, and in the near future, large-scale DAVINCH^{TM} systems will be delivered to accelerate treatment.

Conclusions

Chemical weapons, whose use began about 100 years ago, not only caused inhumane damage during the war, but they are still threatening the lives of the residents and the environment as unexploded munitions, etc., in various places. Under such circumstances, many old or abandoned chemical weapons have been destroyed without accidents in and outside of Japan from 2004 to the present using DAVINCH™ systems developed by Kobe Steel.

Kobe Steel will continue to improve the design of detonation chambers, process, and equipment, while striving to improve the measures for minimizing the risk of leakage and exposure to chemical agents and preventing the spread of pollution, thus to improve the safety and efficiency of treatment.

References

1) Chemical weapons convention. September 27 2005.
2) T. Matsunaga et al. 2000 Environmental research in Japan. Ministry of the Environment, 2001, pp.56-1-56-48.

Design of Detonation Chamber for Destructing Chemical Warfare Materials

Koichi HAYASHI*[1]

*[1] Project Department, CWD Project Center, Engineering Business

Abstract

A detonation chamber is a device for destroying chemical warfare materials by detonation, using tens of kilograms of explosives in the process. Special structural features are required to satisfy fragment resistance, operability and leak tightness. The normal design code for static pressure vessels cannot be applied to the basic structural design of the robust detonation chamber because the detonation shock wave causes instantaneous dynamic pressure. Hence, the Code Case "Impulsively loaded pressure vessels," published recently by the American Society of Mechanical Engineers (ASME), was used as the design guideline. It requires dynamic pressure analysis and dynamic stress and strain analysis, which are used for the evaluation of each mode of failure such as fatigue damage and local strain limit, to allow detailed design. This paper introduces the design features with examples.

Introduction

A detonation chamber is a device inside which a chemical weapon is detonated using an explosive of several tens of kilograms. There are structural limitations in order to satisfy application-specific performance such as fragment resistance, operability, and leak tightness. The normal design code for static pressure cannot be applied as-is to the structural design for robustness. This is because the shock wave that occurs during detonation causes an impulsive load.

Recently, special codes for impulsive load, ASME Section VIII Division 3[1)] (hereinafter referred to as "ASME") and Code Case 2564[2)] (hereinafter referred to as "Code Case"), have been published, and these are now used as design guidelines. Kobe Steel participates in the Task Group of these ASME special codes and cooperates in providing information, etc. These special codes provide techniques for performing dynamic pressure analysis and dynamic stress/strain analysis to evaluate each fracture mode, including fatigue damage and local strain limitation. Although the design procedure and evaluation criteria are complicated and stringent, the application of these codes has made it possible to design safer detonation chambers and to evaluate their safety.

This paper introduces the structural features of detonation chambers, their design technique, and examples of their design and evaluation.

1. Structure of detonation chamber

Detonation chambers are basically steel pressure vessels, and **Fig. 1** shows a model diagram of the basic structure. For detonation destruction of chemical munitions, it has structural features with the functions of fragment resistance, operability, leak tightness, and robustness to withstand detonation impact. These features are outlined below.

1.1 Fragment resistance

If the chemical weapon to be detonation-destructed is a piece of ammunition, the fragments of the ammunition shell will collide with the inner surface of the detonation chamber at high speed during the detonation and cause damage to the surface. Robustness decreases when the pressure-resistant part intended to withstand the detonation

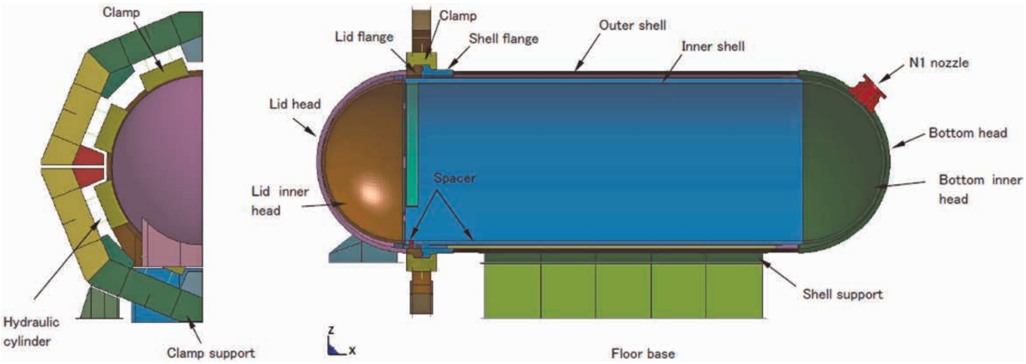

Fig. 1 Structural model of detonation chamber

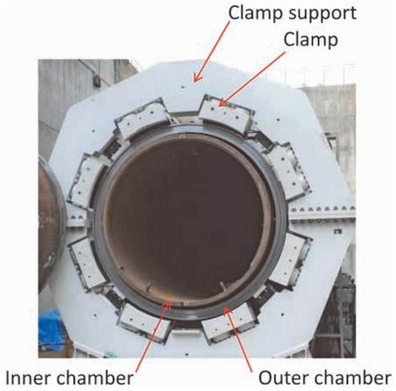

Fig. 2 Inside view of detonation chamber

shock wave is thinned by damage. As shown in **Fig. 2**, the body and heads have double wall structures, each consisting of an outer shell and inner shell, in which the outer shell is responsible for the sealing performance of the pressure vessel, and the inner shell is responsible for fragment resistance. A gap is provided between the inner shell body and the inner shell lid head so that the inner shell does not become a closed vessel, and the shock wave pressure leaks from the inner shell to the inner surface of the outer shell.

The inner shell is made of high-strength steel of 800 MPa grade (JIS SHY685) with high fragment resistance. In case of damage, the inner shell alone can be pulled out from the outer shell and replaced.

1.2 Operability

It is necessary to carry in and place a chemical weapon inside the detonation chamber and collect the fragments after detonation. For this reason, the vessel is made horizontal, and the lids are hydraulically driven so that they can be fully opened. Fig. 2 shows the open state. For detonation destruction, the operator places each chemical weapon at the center of the axis of the detonation chamber. Therefore, the diameter is kept to 3m or less from the viewpoint of operability.

The horizontal vessel is subjected to a large, horizontal, impulsive load on the mount support during detonation. In early days, large strains and cracks occurred for this reason. In order to solve these problems, the support parts have been reviewed and improved in detail, including the size of the ribs, their combinations, and the welding method, on the basis of analysis and actual operation data. **Fig. 3** shows an example of the improved mount support structure.

The pressure caused by the shock wave is inversely proportional to the cube of the propagation distance. Therefore, in the case of a cylindrical vessel with a given capacity, the stress on the cylindrical body can be reduced by increasing the inner diameter and shortening the overall length. The above-mentioned operability problem, however, limits the diameter of the horizontal cylinder. Therefore, when increasing the processing capacity of explosives, the axial length of the cylinder is extended.

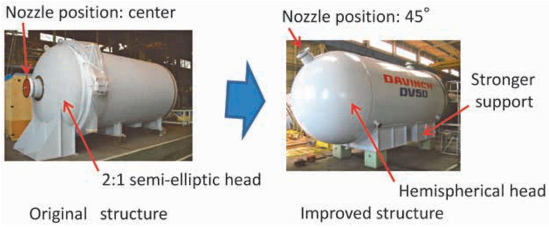

Fig. 3 Example of structural improvement

1.3 Leak tightness

The allowable concentration of the chemicals released from chemical weapons into the treatment environment is low, and the movable lids must have high leak tightness so that gas leakage during detonation can be prevented. In the original structure, the lid was fixed by a pair of split rings fastened by bolts, however, with the increase in explosive load, the structure was changed to a hydraulic clamping type with higher leak tightness (Fig. 2). The lid-side and body-side flanges are hydraulically tightened with eight clamps to maintain sealing performance between the two flanges. Their deformation behaviors have also been confirmed by dynamic analysis, and various mechanical improvements have been implemented, such as a fitting structure with a spigot joint on each flange.

1.4 Structural robustness against detonation shock waves

The greatest issue in the evaluation of structural robustness is brittle fracture due to explosion shock waves. To prevent this, the body has a multi-layered structure, in which thin plates are laminated to form a thick body structure as shown in **Fig. 4**. In this multi-layered structure, even if a crack occurs in the innermost layer (first layer), which receives the shock wave, the crack does not propagate into the second and outer layers due to discontinuity. Consequently, it avoids the occurrence of a brittle fracture that abruptly penetrates the entire thickness. In the event that a crack occurs in the first layer, as shown in the upper left of Fig. 4, the existence of the crack in the first layer can be confirmed

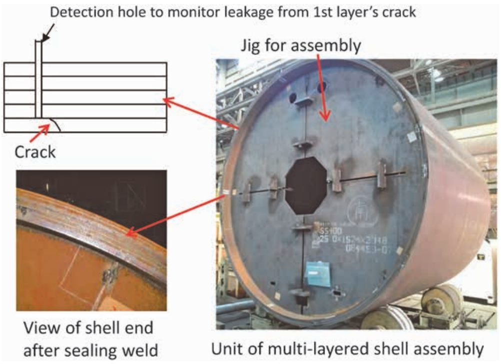

Fig. 4 Multi-layered outer shell

by detecting gas leakage from a detection hole. Meanwhile, the heads, nozzles, flanges, etc. have single-walled structures made of 3.5% Ni steel with high toughness, such as SA203Gr.E or SA350LF3, which is focused on brittle-fracture resistance rather than tensile strength.

The inner shell body is installed on a spacer with its axis aligned with that of the outer shell body. The inner shell is not fixed to the outer shell so that it can easily be replaced, as mentioned above. Therefore, the inner shell moves in the axial and vertical directions due to the impact energy of detonation and collides with the outer shell. Thus, the impulsive load at the time of collision between the inner shell and the outer shell must be studied. Especially at the localized collision point, the stress generated in the outer shell is elevated. To alleviate this, measures have been taken such as changing the shape of the head from 2: 1 semi-elliptical to a hemispherical shape and changing the nozzle position 45° upward from the center of the head (original nozzle position), as shown in Fig. 3.

2. Structural design

When designing the thickness of an impulsively loaded pressure vessel, the simplest calculation method is to use the formula for a static pressure vessel and set a large safety factor (reduce the allowable stress) in consideration of impulsive load. Setting this safety factor, however, requires many actual values, which makes an appropriate setting difficult. In addition, the detonation chamber-specific structure itself, as mentioned above, plays a critical part in robustness, making the above formula inapplicable. Hence, Kobe Steel has established its own method of designing detonation chambers and evaluating their safety using the ASME special codes as design guidelines.

This section outlines this method of design and safety evaluation, while introducing an example of design and evaluation aiming at the largest class of detonation chamber to date, with a designed explosive load exceeding a 60 kg TNT equivalent.

2.1 Design Input

In the design of detonation chambers, the concept of "design pressure" as in the usual design code is inapplicable, and the detailed structure of each detonation chamber, the material used, and the explosive load (TNT equivalent) are used as design inputs. In addition, the detonation method, including the detonation position of the explosive and the detonation time difference, is also used as design inputs. Even with a given explosive load, the distribution of shock waves differs if detonated at a single position or divided into three positions. In addition, since the mechanical properties of the material used change in accordance with the strain rate under impulsive load, stress-strain curves based on high-speed tensile test results are used.

2.2 Explosion analysis

Fig. 5 shows the change with time of pressure distribution at the time of explosion, analyzed using the impact analysis software AUTODYN®. Note 1) This is an example of simultaneous detonation at three points, in which the inner diameter of the outer shell is 3.0 m, explosive load is 64.2 kg TNT (hereinafter, all the calculation examples in this paper use these conditions) and shows that the pressure wave repeats reflective diffusion with the passage of time.

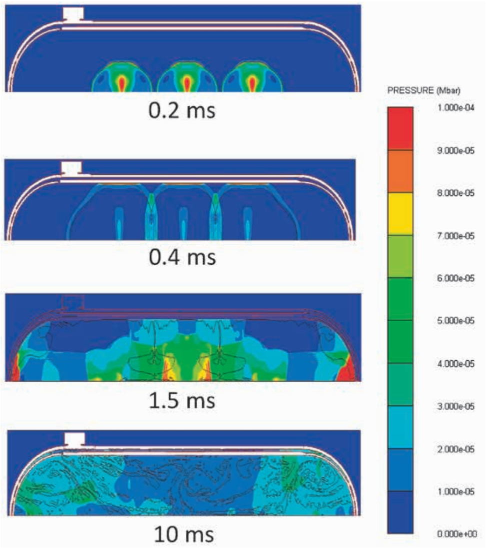

Fig. 5 Change with time of pressure distribution

Note 1) Analysis software based on explicit method designed for a wide range of impact problem analyses such as detonation. Provided by ANSYS1®.

The fluctuation status of the pressure distribution changes depending on detonation conditions, such as the detonation position and detonation time of the explosive. It should be noted that a static pressure vessel has a uniform pressure distribution in the vessel, whereas in a chamber that is subjected to a detonation shock wave, the received pressure differs depending on each position and time. Therefore, it is necessary to find the time history of pressure for each location. **Fig. 6** shows an example of the pressure time history of the inner surface of an outer shell head. The pressure does not decay monotonically but shows several peaks. This indicates that each shock wave repeats reflective diffusion to exert an impact force on the location.

2.3 Dynamic structure analysis

Dynamic stress and strain distributions are calculated by impact structure analysis software LS-DYNA®Note 2) on the basis of the time history of pressure at each position. Similar to pressure, stress and strain distribution that occur in the outer shell repeatedly show peaks. This also takes into account the impulsive load of the inner shell collision. Example analysis results will be introduced individually for each of the following evaluation items.

2.4 Evaluation based on ASME and Code Case

This section describes the basic concept of the evaluation method and evaluation examples for the four types of fracture modes.

2.4.1 Leak before burst mode of failure (LBBM)

The LBBM is specified in ASME KD-141 and indicates that no crack propagates at a high enough speed to cause catastrophic fractures. The multi-layered part of the body is structurally recognized as LBBM by ASME KD-810, while the single-walled part is judged to be LBBM if both of the following two conditions (I) and (II) are met.

(I) Assuming that a crack has reached 80% of the total thickness (t) of a material, the stress intensity factor, K_I, at the crack tip shall be smaller than the fracture toughness value, K_{Ic}, of the material.

(II) The remaining ligament (distance from the crack tip to the free surface) shall be smaller than $(K_{Ic}/\sigma_{ys})^2$.

The following describes the detailed evaluation method. The crack shape is assumed to be semi-elliptical as shown in ASME KD-410, and the ratio of depth (a) to length ($2c$) to be 1:3. The K_I value at the crack tip is expressed by the following equation.3)

$$K_I = [\sigma_0 G_0 + \sigma_1 G_1 (a/t) + \sigma_2 G_2 (a/t)^2 + \sigma_3 G_3 (a/t)^3 + \sigma_4 G_4 (a/t)^4]\sqrt{\pi (a/Q)} \quad \cdots\cdots (1)$$

$$Q = 1 + 1.464 (a/c)^{1.65} \quad \cdots\cdots (2)$$

$$\sigma(x) = \sigma_0 + \sigma_1 (x/t) \quad \cdots\cdots (3)$$

$\sigma(x)$ is calculated by Eq. (3) on the basis of the instantaneous maximum stress:

wherein,

σ_0 to σ_4: coefficients when the stress $\sigma(x)$

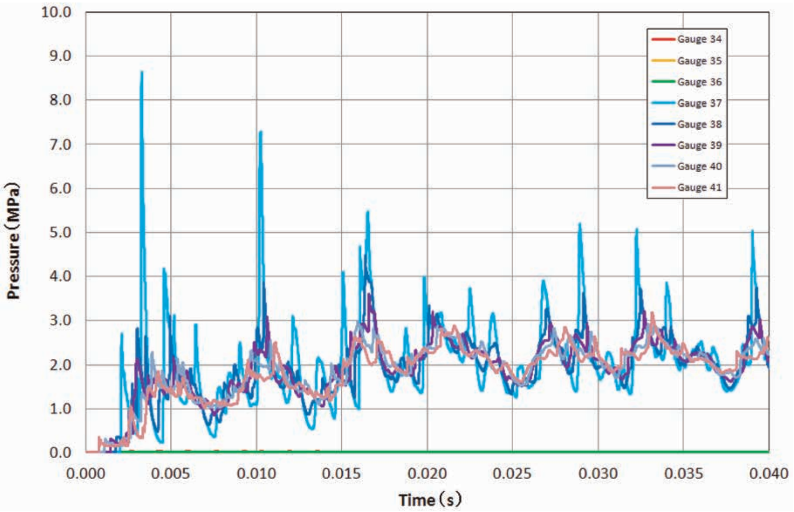

Fig. 6 Time history of pressure of inside surface of outer lid head

---

Note 2) High-speed nonlinear dynamic analysis software based on explicit method provided by Lawrence Software Technology Corporation.

orthogonal to the crack is expressed by a fourth-order polynomial

t: plate thickness,

x: distance (0 to t) from the edge,

Q: crack shape coefficient,

G_0 to G_4: influence coefficient, and

σ_{ys}: static yield strength.

K_{Ic} is calculated using the equation below.

$$(K_{Ic}/\sigma_{ys})^2=5(CVN/\sigma_{ys}-0.05) \cdots\cdots\cdots\cdots \quad (4)$$

wherein,

CVN: the absorbed energy value obtained by the Charpy impact test in relevance with the toughness value of the material.

Next, an evaluation example of the chamber, our subject this time, is shown. Regarding (I), K_I =107 MPa m$^{1/2}$, and K_{Ic} = 225 MPa m$^{1/2}$ which satisfies $K_I < K_{Ic}$. Regarding (II), the remaining ligament is 20% of the wall thickness of 75 mm, which is 15 mm, so $(K_{Ic} / \sigma_{ys})^2$ = 670 mm, which satisfies remaining ligament $<(K_{Ic} /\sigma_{ys})^2$. Therefore, since both conditions (I) and (II) are satisfied, it is judged to be LBBM.

2.4.2 Global plastic instability

The Code Case requires dynamic elastic plastic analysis to show that an impulsive load will not form a plastic instability state. For example, there shall be no complete plastic hinge formation around the opening. In the case of a detonation chamber, the exhaust gas nozzle part of the body-side head and the flanges on the lid side and body side are evaluated. The design margin of the impulsive load is specified as 1.732. Specifically, analysis evaluation is performed using a load of 175% of impulsive load (pressure), which corresponds to the designed explosive load.

Fig. 7 shows an example of the distribution of effective equivalent plastic strain viewed from the lid side of the body side flange. Although an effective equivalent plastic strain is observed on the flange member, an elastic region is confirmed to exist over the entire cross section. That is, no complete plastic hinge is confirmed to exist on the body side flange and no plastic instability state is judged to exist.

2.4.3 Local strain limit

The Code Case stipulates the following three conditions for the local plastic strain limit.

(1) The acceptable value of the maximum equivalent plastic strain shall be 0.2% on average for the thickness of the vessel.

(2) The acceptable value of the maximum plastic strain component, linearized through the thickness of the vessel, shall be 2% (1% at welds).

(3) The acceptable value of the maximum peak equivalent plastic strain at any point in the vessel shall be 5% (2.5% at welds).

These are the criteria for a one-time detonation, and the cumulative residual plastic strain caused by multiple detonations must be evaluated on the basis of the same criteria. It should be noted, however, that a shakedown has been experimentally confirmed in the high strain region even in the case of impulsive load deformation caused by detonation,[4)] and the so-called ratcheting phenomenon, in which the cumulative residual plastic strain increases with each detonation, does not occur. Thus, the evaluation should be performed on the basis of the amount of a single residual plastic strain caused by the maximum amount of detonation.

Table 1 shows an example of the analysis results of the maximum peak plastic strain component and the equivalent plastic strain at the maximum peak under the above condition (3) in the lid head in this case example. The example result is 50,000 (25,000 at welds) μ or less, which satisfies the criterion of condition (3). Although the calculated value is omitted, conditions (1) and (2) are also satisfied and it is judged to fall within the criteria.

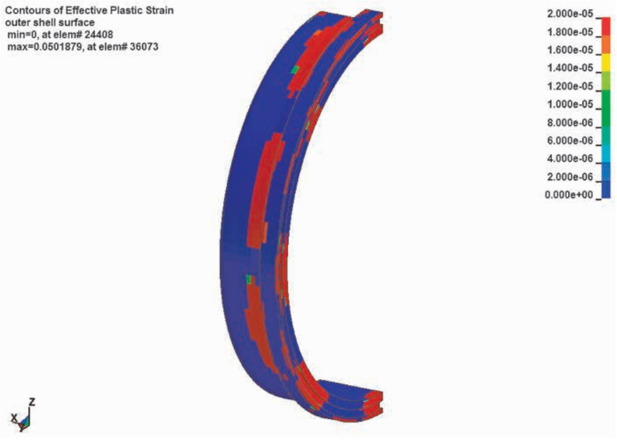

Fig. 7 Contours of effective equivalent plastic strain in shell flange (175% load)

Table 1 Maximum peak equivalent plastic strain of lid head

Plastic strain component						Equivalent plastic strain	Acceptable range
$\varepsilon_{xx,p}$	$\varepsilon_{yy,p}$	$\varepsilon_{zz,p}$	$\varepsilon_{xy,p}$	$\varepsilon_{yz,p}$	$\varepsilon_{zx,p}$	$\varepsilon_{eq,p}$	
-589	75	210	23	1	521	792	<50,000 <25,000 weld

unit ; μ

2.4.4 Fatigue fracture evaluation

When the LBBM is proved, the fatigue fracture evaluation permits the use of ASME KD-3 to obtain the number of cycles until a crack occurs. If the LBBM is not proved, fracture mechanical evaluation must be performed on the basis of ASME KD-4, which evaluates the propagation of cracks that have occurred.

As mentioned above, the latest model of the detonation chamber uses a material with high fracture toughness and the LBBM has been proved, so evaluation based on ASME KD-3 has been carried out. The following describes the outline.

(1) Strain amplitude

From the time history of strain amplitude, the equivalent strain amplitude is calculated for each strain peak group for each time via the following equation using the rainflow counting algorithm from ASME KD-353.

$$^{mn}\Delta\varepsilon_{ij} = {}^{m}\varepsilon_{ij} - {}^{n}\varepsilon_{ij} \cdots\cdots\cdots\cdots \quad (5)$$

$$^{mn}\Delta\varepsilon_{range} = \sqrt{2}\sqrt{\{({}^{mn}\Delta\varepsilon_{11} - {}^{mn}\Delta\varepsilon_{22})^2 + ({}^{mn}\Delta\varepsilon_{22} - {}^{mn}\Delta\varepsilon_{33})^2 + ({}^{mn}\Delta\varepsilon_{33} - {}^{mn}\Delta\varepsilon_{11})^2 + 6({}^{mn}\Delta\varepsilon_{12}^2 + {}^{mn}\Delta\varepsilon_{23}^2 + {}^{mn}\Delta\varepsilon_{31}^2)\}/3} \cdots\cdots\cdots\cdots \quad (6)$$

wherein,

$^{m}\varepsilon_{ij}$: strain component at time m

$^{mn}\Delta\varepsilon_{range}$: equivalent strain amplitude

(2) Fatigue strength reduction factor

Because the fatigue strength of local shape discontinuities, such as the base of the nozzle, is decreased, the strain amplitude is multiplied by a fatigue strength reduction factor for the evaluation. The fatigue strength reduction factor is basically a factor related to the stress concentration coefficient calculated from the shape.

(3) Fatigue curve

Being a low cycle fatigue due to plastic strain, it is evaluated using a strain-life curve instead of a stress-life curve. The evaluation is performed on the curve shown in **Fig. 8** with a margin of three times the life of the best fit curve estimated from the ASME design fatigue curve. The value obtained by multiplying the strain amplitude at each time by the fatigue strength reduction factor and the corresponding lifetime N_i on the fatigue curve are obtained, and the fatigue damage level $1/N_i$ of one strain peak group is calculated. Next, the total $\Sigma 1/N_i$ is calculated for all strain peak groups generated by one detonation. This yields the total fatigue damage level from one detonation.

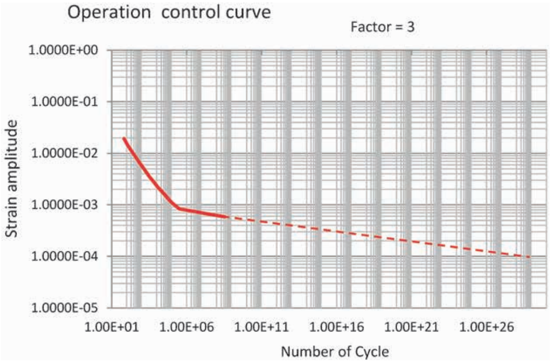

Fig. 8 Fatigue curve

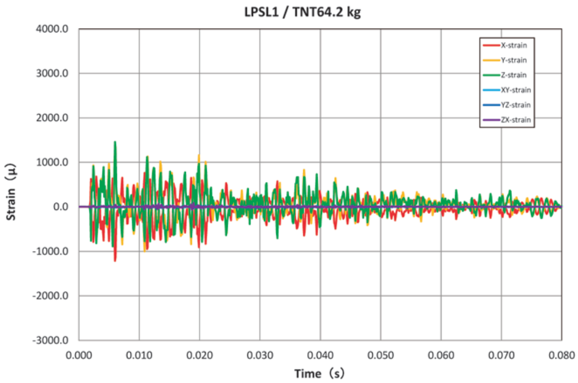

Fig. 9 Time history of dynamic strain of top of lid head

(4) Fatigue damage level during multiple detonations

For example, if the planned number of detonation cycles is n and the explosive conditions, such as explosive load, are the same for all detonations, the cumulative fatigue damage level is given by $n \times \Sigma 1/N_i$. If the cumulative fatigue damage level reaches 1, it is judged to have reached the end of life, so the tolerable detonation cycle in the design calculation is given by $n = 1/(\Sigma 1/N_i)$.

Fig. 9 shows the dynamic strain time history of this example (lid head part). The fatigue damage level per detonation cycle, obtained by the above procedure, is 7.8E-05, and the tolerated number of detonation cycles is 12,800 cycles. In this example, the tolerated number of detonation cycles by design is approximately 1,700 cycles, and the design criteria is satisfied.

In the case of this example, all four fracture modes satisfy the criteria, and safety is guaranteed by the design.

3. Design verification and operation management

ASME KD-12 stipulates design verification by testing, and design verification has been performed on detonation chambers by actually measuring the strain in detonation testing. There is also a technique called fracture testing, however, in the

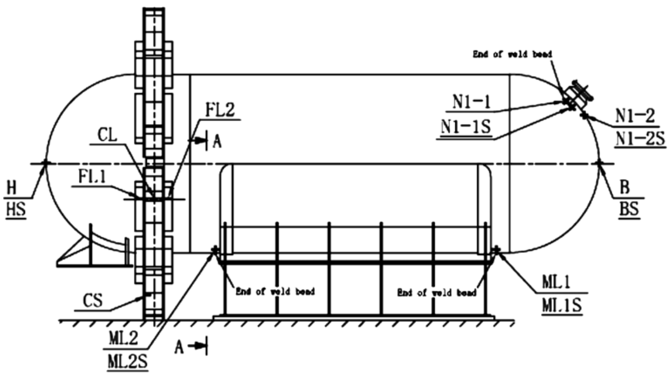

Fig.10 Positions of strain gauge

case of detonation chambers, the strain generated by the designed explosive load is measured. The critical points shown in **Fig.10** are selected as the measurement positions. The static strain gauge confirms the cumulative residual plastic strain (Section 2.4.3), and the dynamic strain gauge confirms the fatigue damage from each detonation (Section 2.4.4). The cumulative calculation of fatigue damage can be performed during the test using a proprietary calculation program.

In addition, strain is measured during actual operation, and cumulative residual plastic strain and cumulative fatigue damage are calculated for each detonation, which is used for maintenance by predicting repairs and replacement timings.

Conclusions

More than ten years have passed since a detonation chamber was introduced into a real-world chemical weapons destruction project. During that period, structural design techniques have been established on the basis of the ASME's special design codes for impulsively loaded pressure vessels. Kobe Steel will strive to further improve the design and reflect it in maintenance, improvement, and development for further enhancement of its safety.

Finally, we would like to express our sincere gratitude to the late Dr. Robert E Nickell, the former president of ASME, for his cooperation and guidance in design.

References

1) ASME Code Section VIII Division 3. Alternative Rules for Construction of High Pressure Vessels.
2) Code Case 2564-4. Impulsively Loaded Pressure Vessels, Section VIII Division 3.
3) WRC Bulletin 471 May. 2002.
4) J. K. Asahina et al. "ASME" Proceedings of PVP2011-57843, pp.135-139.

Strengthening of Aluminum Alloy Forgings for Automotive Suspension by Two-step Aging

Masayuki HORI[*1] · Kenichi HIRUKAWA[*2] · Masashi NAKANO[*3] · Masakazu TANAKA[*4] · Yohei OKAFUJI[*3]

[*1] Aluminum Casting & Forging Plant, Aluminum Casting & Forging Unit, Advanced Materials Business
[*2] Kobelco Research Institute, Inc.
[*3] Kobe Aluminum Automotive Products, LLC
[*4] Suspension Plant, Aluminum Extrusion & Suspension Unit, Advanced Materials Business

Abstract

In order to improve the fuel efficiency of automobiles, it is important to reduce the weight of vehicle bodies. The weight of suspensions is also being reduced, by applying Al-Mg-Si aluminum alloy forgings, for example. Further reducing the weight of suspensions will require additional strengthening of the material, and Kobe Steel has conducted a study to increase the strength by two-step aging. As a result, a two-step aging process combining pre-aging at 160℃ and high-temperature aging at 190℃ has achieved a peak proof stress of 390 MPa in a short time period of only 8 hours. Obtaining the same peak proof stress by single-step aging at 160℃ requires 56 hours. This is attributed to the fact that β″ phase, having a size of 3 to 4 nm, which is greater than the critical size for non-reversion, precipitates with a high number density during the pre-aging and grows at the high temperature to increase the strength. This technology has enabled a weight reduction of 3% over that of the conventional technology and is expected to contribute to improving fuel efficiency and reducing the carbon dioxide emissions of automobiles.

Introduction

Recently, regulations on exhaust gas have become even more stringent due to global environmental problems, and the further reduction of exhaust gas, especially carbon dioxide, has become an important issue in the automobile industry as well. The improvement of fuel efficiency through the weight reduction of vehicle bodies is a promising means that is causally linked to the emission reduction of carbon dioxide, the cause of global warming.[1)] In addition, the vehicle body weight must be reduced to compensate for the weight increase due to additional safety measures, environmental measures, and equipment enhancement. Suspension materials have been studied to meet these weight reduction needs, and the application of 6000 series aluminum forgings has been expanding.[2)] For further weight reduction, the strengthening of material is effective, and Kobe Steel uses 6000 series aluminum alloy forgings (KD610) with the addition of Cu.[3)]

Yet further weight reduction requires additional strengthening, and an approach from the aspect of processing is also being studied. As one method, it is generally known that strengthening can be achieved by artificial aging at a low temperature for an extended period of time, in which the strengthening is attributable to fine and densely dispersed precipitates. Such a long aging time, however, causes problems of decreased productivity and an increased environmental burden. Kaneko reported that the peak proof stress of a sheet of A6061 alloy is improved by two-step aging with pre-aging at 120℃ for 24 hours.[4)] This, however, poses the problem of a long pre-aging time. Moreover, such studies are being actively conducted for sheet materials that are BH-treated[Note 1), 5)] but there are few reports for structural members. Hence, Kobe Steel studied the effect of two-step aging on strengthening by applying short-period pre-aging to 6000 series aluminum forgings and considered the mechanism of such strengthening through microstructural observation. This paper introduces the outline of the study.

1. Test method

Material with the chemical composition shown in **Table 1** was used for the test. A billet of φ90 mm was cast by a horizontal continuous casting machine and shaved to φ84 mm. The shaved billet was homogenized at 500℃, air cooled, and then heated to 520℃ to be forged at a reduction rate of 70% (φ84 mm → t 25.2 mm). After solution heat treatment and subsequent water cooling, pre-aging was performed at a temperature between 120 and 180℃ for 5 hours, and the second-step aging treatment was performed at 190℃ to prepare the test material. Hereinafter, the material obtained by performing pre-aging and

Table 1 Chemical composition of specimen

(mass%)

Si	Fe	Cu	Mn	Mg	Cr	Zn	Ti	Al
0.97	0.22	0.43	0.45	0.97	0.17	<0.01	0.03	Rem.

[Note 1)] BH treatment is a treatment that uses the heat of paint baking to increase the strength (proof stress).

second step aging is referred to as a two-step aged material. The above heat treatment procedure is summarized in **Fig. 1**. For comparison, single-step aging curves for 160℃ and 190℃ were prepared. All the heat treatments were performed in the atmosphere.

Age hardening behaviors were evaluated by a tensile test. Each tensile test piece, a JIS No.4 subsize test piece (gauge length 25 mm), was collected parallel to the forging direction (cogging direction). Thin film specimens were prepared by electropolishing the pre-aged and two-step aged materials and were subjected to observation by transmission electron microscope (hereinafter referred to as "TEM"). The evaluation of the precipitate phase after pre-aging was performed by differential scanning calorimetry (hereinafter referred to as "DSC") measurement. These test pieces were collected from the positions shown in **Fig. 2**.

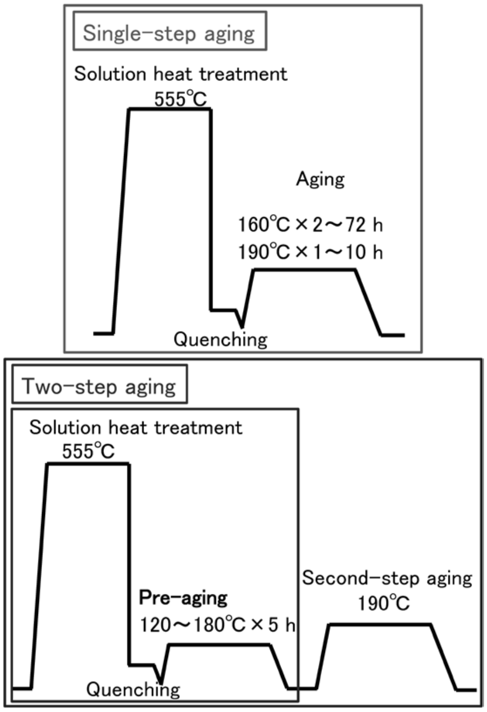

Fig. 1 Heat treatment processes of specimens

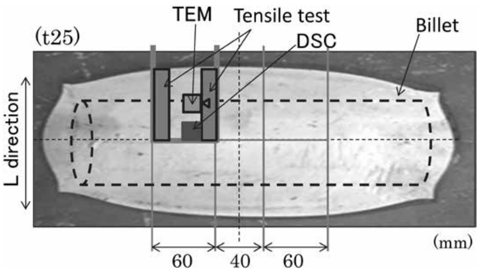

Fig. 2 Collection positions of test pieces

2. Test results and considerations

2.1 Aging curves

Fig. 3 shows single-step aging curves at 160℃ and 190℃, respectively, as well as a two-step aging curve at 190℃ after a pre-aging at 160℃ for 5 hours. The peak proof stresses were 390 MPa for the aging temperature of 160℃ and 375 MPa for the aging temperature of 190℃, the former yielding a higher strength. The aging times to the respective peaks were 56 hours and 3 hours. Meanwhile, it was found that pre-aging at 160℃ ×5 hours and subsequent aging at 190℃ can reduce the total aging time from 56 hours to 8 hours without sacrificing the peak proof stress at 160℃.

Hence the effect of the pre-aging temperature on the tensile properties of the two-step aged material was investigated to obtain the optimum pre-aging temperature. The results are shown in **Fig. 4**. The aging conditions for the second step were 190℃ ×3 hours. When the pre-aging time of the first step

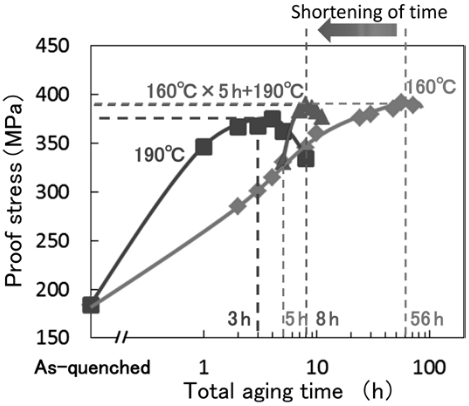

Fig. 3 Single-step aging curves at 160℃ and 190℃, and two-step aging curve at 190℃ after pre-aging at 160℃×5 h

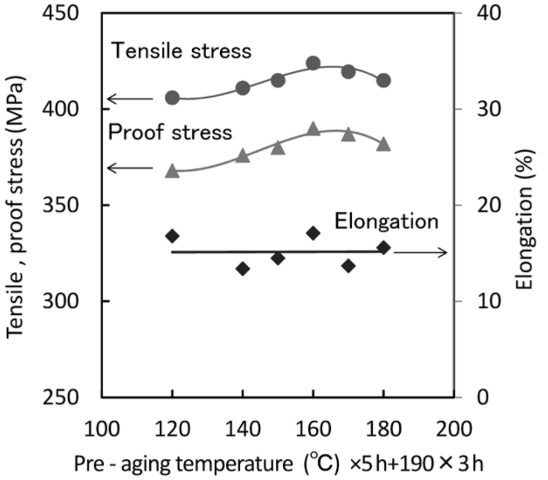

Fig. 4 Effect on tensile properties of pre-aging temperature

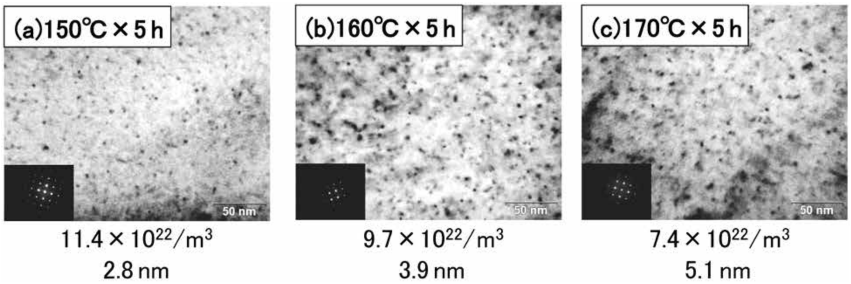

Fig. 5 TEM micrographs after pre-aging (upper values: number density of precipitates, lower values: size of precipitates)

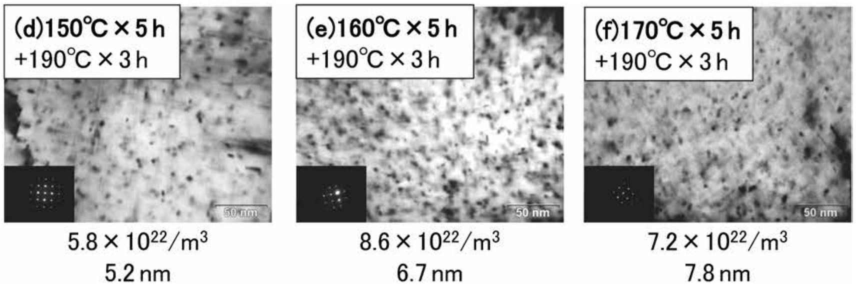

Fig. 6 TEM micrographs after two-step aging (upper values: number density of precipitates, lower values: size of precipitates)

was fixed at 5 hours to vary the aging temperature, the highest strength was found to be reached at 160℃. Here, a decision was made to investigate this mechanism in detail by microstructure observation.

2.2 Microstructural observation

Fig. 5 shows TEM micrographs after 5 hours of pre-aging at 150℃, 160℃ and 170℃. Precipitates are observed by the TEM for all the aging conditions, and these precipitates are considered to be β'' phase.[6] The precipitates become finer and more densely populated due to having been aged at lower temperatures.

Fig. 6 shows the TEM micrographs of the pre-aged materials in Fig. 5 subsequently aged at 190℃×3 hours in the second step. Regardless of the pre-aging conditions, the size of the precipitates is increased by the second-step aging. For the material pre-aged at 150℃, the number density of precipitates is found to be significantly decreased by the second-step aging. The relationship between the precipitate size and the number density is summarized in **Fig. 7**. It should be noted that the number density of precipitates has been calculated by measuring the number of black dots precipitated in the vertical direction of each photograph and multiplying the number by a factor of three. The pre-aging at a low temperature makes precipitates finer and more densely populated, while the second step aging increases the precipitate size. However, some portion of the material pre-aged at 150℃ has been found to have undergone reversion. From this, it is estimated that a critical size of precipitates that undergo reversion at 190℃ exists between 3 and 4 nm.

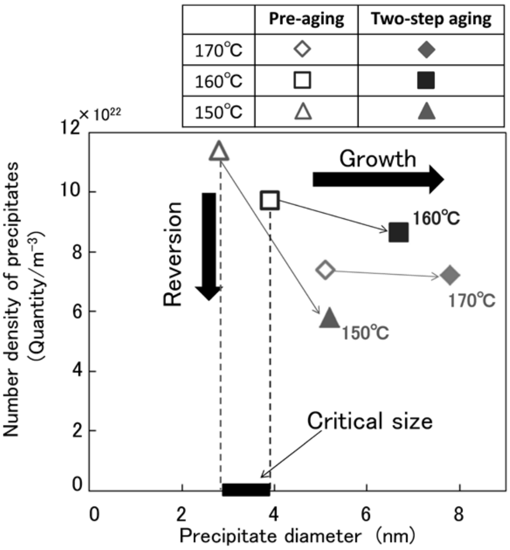

Fig. 7 Relationship between size and number density of precipitates after pre-aging and two-step aging

2.3 DSC

In order to confirm the microstructural change during heat treatment, DSC was performed while combining the aging and heating rate of the second step (**Fig. 8**). The results show an exothermic peak 1, considered to be attributable to β'', and an exothermic peak 2, considered to be attributable to β'.[7] The pre-aging temperature of 150℃ or lower results in a high β''peak and the pre-aging temperature of 160℃ or higher results in a smaller peak. This seems to indicate that the precipitation of β'' is completed at 160℃ and higher.

Fig. 9 shows the results of TEM observation, in which the material pre-aged at 160℃ × 5 hours has been quenched at the exothermic peak 1 temperature of 220℃. A comparison with post pre-aging (Fig. 5(b)) shows that the density of precipitates has decreased. From this, it is estimated that some of the β'' precipitates have undergone reversion, while the rest has coarsened.

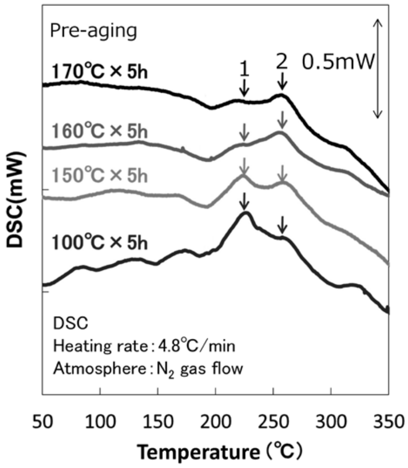

Fig. 8 DSC results after pre-aging

2.4 Mechanism of two-step aging in appropriate conditions

A model of the precipitation process is shown in **Fig.10**. The model assumes that β'' phase precipitates during the pre-aging, and then the β'' phase grows during the second-step aging and contributes to strengthening. Compared with the pre-aging at 160℃ (Fig.10 (b)), pre-aging above 170℃ (**Fig.10** (a)) results in β'' precipitating at a lower density during the pre-aging. In the subsequent second-step aging, the β'' phase grows and contributes to strengthening. On the other hand, when pre-aging is performed at 150℃ or below (Fig.10 (c)), finer β''

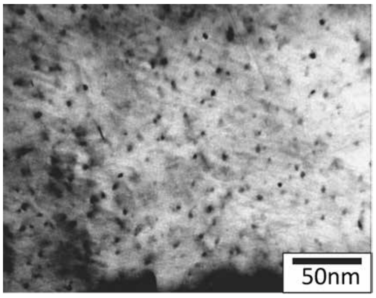

Fig. 9 TEM micrograph of specimen pre-aged at 160℃ × 5 h and quenched at temperature of DSC peak 1 (Number density of precipitates: 5.2×10^{22}/m^3, size of precipitates: 6.7 nm)

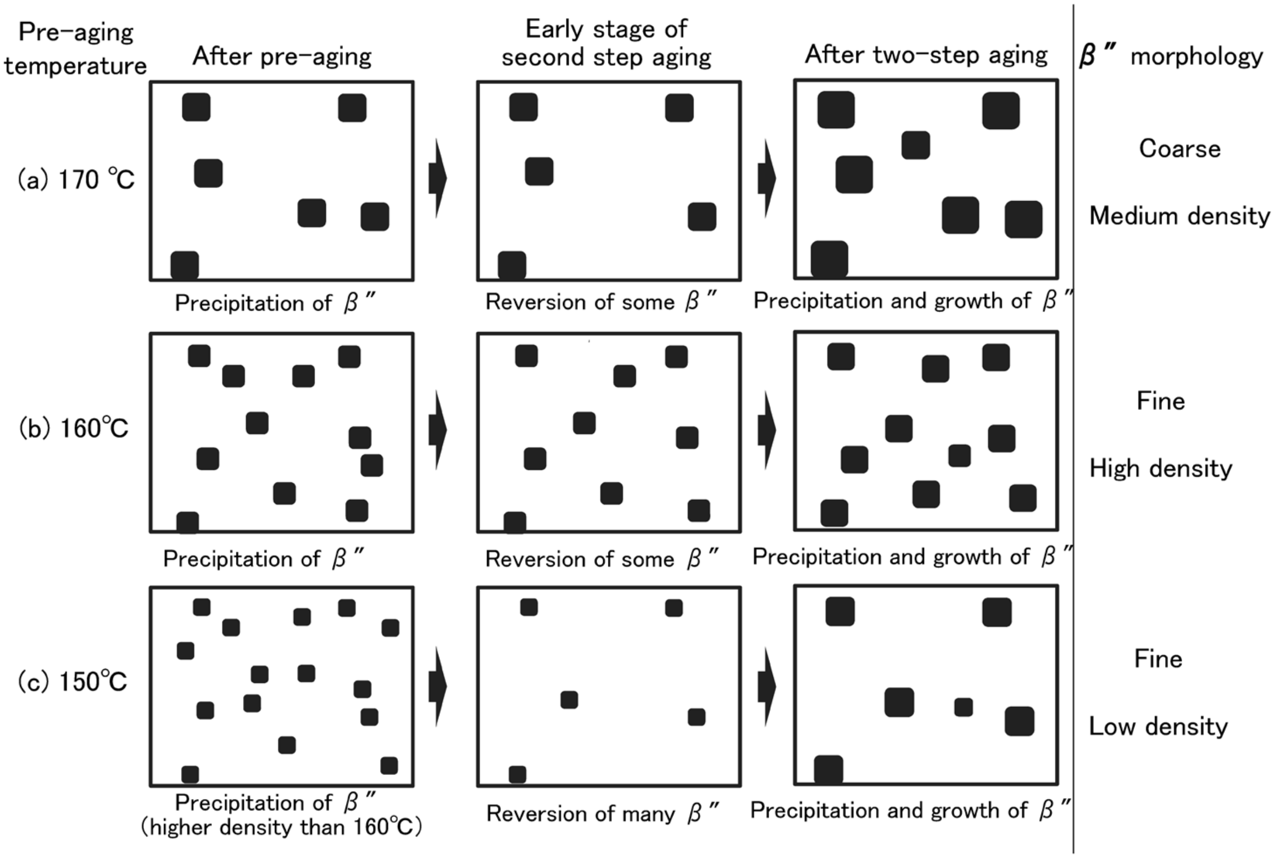

Fig.10 Schematic models of precipitation processes for two-step aging

phase is precipitated at a higher density compared with the pre-aging at 160℃. However, since the precipitate size is small, most of the precipitates undergo reversion during the second-step aging. This is considered to have caused the precipitate density after the second-step aging to become lower than that for the pre-aging at 160℃. In other words, 160℃ is considered to be the temperature at which the β″ phase that has precipitated during 5 hours of pre-aging remains at the highest density during the second step aging without undergoing reversion.

3. Weight reduction effect of strengthening by two-step aging

The relationship between the proof strength and weight reduction rate of aluminum alloys is shown in **Fig.11**.8) Kobe Steel is already mass-producing KS651 and KD610, each having a strength higher than that of A6061. It has been found that further strengthening of the material can be realized by the newly developed two-step aging. This new approach is expected to achieve a weight reduction of approximately 3% compared with the conventional KD610, while minimizing the decrease in productivity.

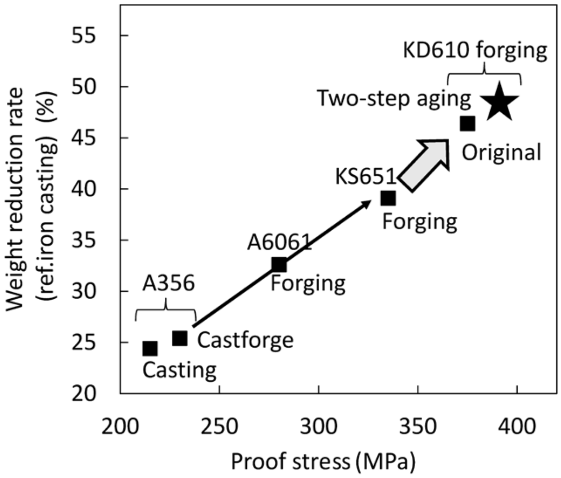

Fig.11 Relationship between proof strength and weight reduction rate of aluminum alloy8)

Conclusions

The effect of pre-aging on the aging behavior of Al-Mg-Si-Cu alloy has been studied. As a result, the peak proof stress has been found to be increased by changing the aging temperature from 190℃ to 160℃, which, however, requires a long heat treatment time of 56 hours.

Meanwhile, short-time strengthening conditions utilizing two-step aging have been investigated, and the following has been found:

- Two-step aging: By applying first-step aging (160℃ ×5 hours) followed by second-step aging (190℃ ×3 hours), the peak proof stress obtained at low temperature after an extended period of time was achieved in 8 hours.

The strengthening mechanism under these conditions is considered to be as follows:

- It has been found that precipitating β″ phase greater than a critical size of 3 to 4 nm at a high density during pre-aging results in growth without reversion during the second step aging.
- A high pre-aging temperature results in a sparse distribution of precipitates, and a low pre-aging temperature also results in a sparse distribution of precipitates due to reversion during the second-step aging. In neither case could high peak proof stress be achieved.

Automotive materials are required to be even lighter to improve fuel efficiency. Kobe Steel will respond to these weight reduction needs and realize the strengthening of material for further expanding the use of aluminum forged suspensions.

Reference

1) K. Minato. IATSS Review. 2004, Vol.29, No.2, pp.103-108.
2) T. Watanabe et al. ALUTOPIA. 2007, Vol.37, No.4, pp.9-14.
3) Y. Inagaki et al. *R&D Kobe Steel Engineering Reports*. 2009, Vol.59, pp.22-26.
4) J. Kaneko. Journal of Japan Institute of Light Metals (J. JILM). 1977, Vol.27, No.2, pp.49-56.
5) K. Yamada et al. Journal of Japan Institute of Light Metals (J. JILM). 2001, Vol.51, No.4, pp.215-221.
6) H. Suzuki et al. Journal of Japan Institute of Light Metals (J. JILM). 1980, Vol.30, No.11, pp.609-616.
7) M. Kanno et al. Journal of Japan Institute of Light Metals (J. JILM). 1978, Vol.28, No.11, pp.553-557.
8) Y. Inagaki et al. *R&D Kobe Steel Engineering Reports*. 2005, Vol.55, No.3, pp.83-86.

Mechanism of Attaining High Strength Sintered and Surface-rolled Gear and Merits of Its Application in Automotive Field

Yuji TANIGUCHI*[1] · Satoshi NISHIDA*[2]

*[1] Steel Powder Plant, Steel Powder Unit, Advanced Materials Business
*[2] Steel Powder Unit, Advanced Materials Business

Abstract

With the aim of expanding the application to automobiles, a study was conducted to determine the applicability of sintered parts to transmission gears that require high fatigue strength. Recent studies have reported that sintered and surface-rolled gears based on pre-alloyed steel powder can achieve fatigue strength equal to or higher than that of conventional wrought steel gears, but the mechanism that enables the former to achieve a fatigue strength higher than that of the latter has not been fully clarified. Hence, Kobe Steel has investigated the factors that may bring higher fatigue strength to sintered and surface-rolled gears in comparison with wrought steel and found that it is attributable to their highly compressive residual stress. Also studied were the advantages of applying sintered and surface-rolled gears. By optimizing the surface-rolling conditions so as to improve the tooth profile accuracy, the same contact-pressure fatigue strength as that of the ground product can be obtained without any grinding, suggesting the possibility of eliminating the grinding process.

Introduction

Recently, the reduction of carbon dioxide emissions has become a major challenge as a measure against global warming, and electrification is rapidly progressing in the field of automobiles. Since sintered parts are mainly used for automotive engines, there is a concern that their use may decrease due to the electrification of vehicles.

Under such circumstances, transmission gears are being considered for a new application of sintered parts. Since high fatigue strength is required for the material of transmission gears, low-alloyed steels for machine structural use, such as SCr420, are mainly used after carburization and quenching. Sintered materials tend to have porosities inside, posing the issue that their fatigue strength is lower than that of wrought steel. Meanwhile, densification of the near-surface by surface rolling processing has achieved a fatigue strength equal to or higher than that of the wrought steel gears.1), 2) In particular, Ni-Mo pre-alloyed steel powder that does not contain any easy-to-oxidize elements such as Cr has the advantage that there is little concern about performance degradation due to oxidation even during sintering and heat treatment under the atmosphere of endothermic gas (commonly known as "RX gas"). On the other hand, despite the porosities, which have not been completely removed by surface rolling processing, surface-rolled sintered gears exhibit a fatigue strength superior to that of wrought steel gears, the mechanism of which behind this phenomenon has not been fully elucidated.

Hence, Kobe Steel has conducted a comparative study with wrought steel gears in order to elucidate the factors that increase the fatigue strength of surface-rolled sintered gears. Furthermore, the benefit of replacing wrought steel gears with surface-rolled sintered gears was also examined, with a view to the expansion of applications of the latter. This paper provides an overview.

1. Strengthening mechanism of surface-rolled sintered gears

As for the strength of gears, common practice is to consider bending strength, tooth surface strength, and scoring strength. This section describes the contact fatigue strength of surface-rolled sintered gears.

1.1 Factors affecting contact fatigue strength of gears

Pitting damage is a typical tooth surface damage of gears. Surface hardness, internal defects (inclusion and porosities), the amount of residual austenite, and compressive residual stress are considered to affect the occurrence of pitting.3) Transmission gears are used in driving conditions with high contact-pressure load and slippage, and the tooth surface of each gear is subjected to a temperature rise due to frictional heat. It is reported that not only normal temperature hardness (initial hardness), but also the hardness after annealing at 573 K affects the pitting resistance.4) A comparative study of these factors has been conducted using a surface-rolled sintered gear and a wrought steel gear.

1.2 Test method

The test material of sintered steel was made from a mixed powder prepared by adding 0.3% graphite powder to 0.5% Ni-1.0% Mo pre-alloyed powder (completely alloyed powder) produced by water atomization. A disk shaped blank with a diameter of 70 mm, a height of 30 mm and a target density of 7.5 g/cm^3 was compacted and sintered at 1,120℃ for 60 min in a N_2-10%H_2 atmosphere. The blank was cut into the shape of the helical gear specified in **Table 1**, surface-rolled, and then carburized and quenched. The surface rolling method was plunge-type rolling, and the amount of surface rolling equaled the tool pushing depth of 1.2 mm. The carburizing and quenching conditions were gas carburizing at 930℃ for 120 min, followed by annealing at 160℃ for 120 min. The test material of wrought steel was JIS SCr420 (hereinafter referred to as SCr420) that was cut into the same helical gear shape as the above sintered-steel test material and was carburized and quenched. The carburization and quenching were performed under the conditions of pulse carburizing at 950℃ for 210 min and annealing at 150℃ for 60 min. In order to minimize the effect of the surface roughness on the strength, the maximum height, Rz, specified in JIS B 0601: 2001, was set to 2 μm or less by a tooth surface grinding finish for all the gears.

Table 1 Specifications of test gears (helical gear)

	Drive	Driven
Material	Evaluation material	SCM420 carburized
Module	3	
Pressure angle (deg.)	20	
Helix angle (deg.)	20	
Number of teeth	16	24
Face width (mm)	6	25
Standard pitch circle diameter (mm)	51.1	76.6

The contact fatigue test was performed on power re-circulating type test equipment. The fatigue limit load was determined as the load for which no damaged area reaches 2% even if the number of load cycles exceeds 1.5×10^7. A PSPC-type micro X-ray measuring apparatus was used to measure the amount of residual stress and residual austenite.

1.3 Test results and discussion

The results of the contact fatigue test are shown in **Fig. 1**. The vertical axis represents the calculated value of the Hertz contact stress at each pitch point. This test has also confirmed that the surface-rolled sintered gear has higher contact fatigue strength than the wrought steel gear.

Table 2 shows the measurement results for surface hardness and the amount of residual austenite. The hardness and the amount of residual austenite of the surface-rolled sintered gear and wrought steel gear were found to be almost the same.

Fig. 2 shows a cross-sectional photograph near the pitch point (broken-line frame in the figure). No coarse inclusion was found in either one of the gears,

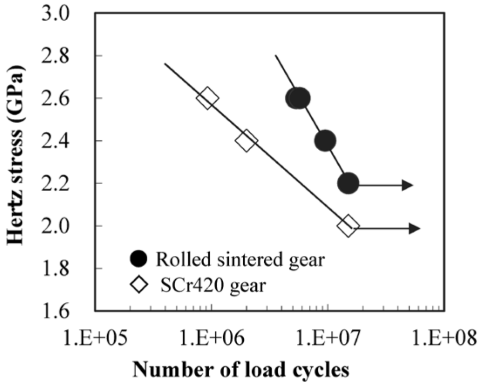

Fig. 1 Results of contact fatigue test

Table 2 Surface hardness and amount of residual austenite

		Rolled sintered gear	SCr420 gear
Surface hardness (HV)	before testing	708	717
	after tempering 573K	656	667
Amount of retained austenite phase (%)		14.1	16.0

Rolled sintered gear

SCr420 gear

Fig. 2 Porosities and inclusions near pitch point but there were many small porosities in the surface-rolled sintered gear. Here, image analysis has been performed on the near-surface and a part with a width of 1 mm and depth of 0.5 mm inside, about 1 mm from the surface, and the number of porosities included in the area, as well as the equivalent circle diameter of all porosities, were calculated. The results are shown in **Table 3**. In the near-surface area densified by the surface rolling, coarse porosities of 10 μm or more are as few as 0.6% of the total, and also the maximum diameter is as small as 13.4 μm. Therefore, the influence of porosities on the strength is considered to be extremely small.

The near-surface residual stress of the gear tooth was measured by removing the surface in the depth direction by electro-polishing. **Fig. 3** shows the results of the residual stress measurement in the direction of the tooth depth. The surface-rolled sintered gear has been found to have a higher compressive stress remaining in the near-surface compared with the wrought steel gear. Compressive residual stress is known to be effective for improving contact fatigue strength,5) and the results of this test suggest that it also contributes to the improvement of the contact fatigue strength of the surface-rolled sintered gear.

Table 3 Pore size and distribution of surface-rolled and sintered gear

		Surface	Inside
Mean diameter (μm)		2.8	5.3
Maximum diameter (μm)		13.4	21.6
Ratio of pores (%)	<5μm	89.7	60.7
	5～10μm	9.8	27.5
	>10μm	0.6	11.8

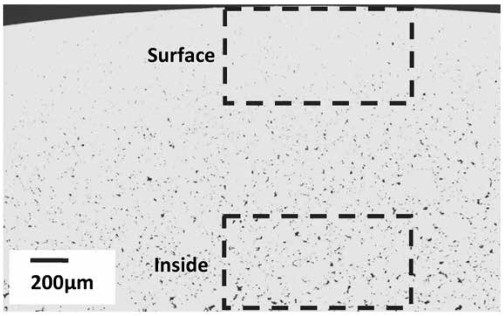

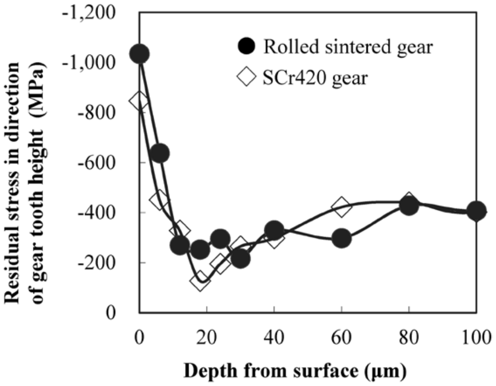

Fig. 3 Near-surface residual stress distribution in tooth depth direction

It should be noted that there is a difference in the magnitude of residual stress between the surface-rolled sintered gear and the wrought steel gear, which is considered to be attributable to the fact that the surface-rolled sintered gear has a density difference between the near surface layer and the inside. That is, the deformation amount at the time of carburizing and quenching differs between the near-surface, which has been densified by surface rolling, and the interior, in which porosities remain. Therefore, the surface-rolled sintered gear results in a greater compressive residual stress than the wrought steel gear, which has little difference in density distribution. It is inferred that this is the expression mechanism of the excellent contact fatigue strength of the surface-rolled sintered gear.

2. Advantages of applying surface-rolled sintered gear

2.1 Tooth profile adjustment effect in the surface rolling process

For automotive transmissions, downsizing and weight reduction are required for the sake of fuel efficiency improvement, and excellent silence from the aspect of driving comfort. Correspondingly, there is an increasing demand for strength improvement and noise reduction for gears. It is known that the tooth profile accuracy of a gear affects its strength and noise,6), 7) and in order to meet the above requirements, the tooth surfaces are more often ground to improve the tooth profile accuracy (hereinafter referred to as gear-tooth grinding).

Fig. 4 shows the production processes of wrought steel gears and surface-rolled sintered gears, respectively, when gear-tooth grinding is performed. In the case of wrought steel gears, the only process step that can adjust the tooth profile accuracy is gear-tooth grinding. In the case of surface-rolled sintered gears, on the other hand, it has been reported that tooth profile adjustment is possible, not only in the gear-tooth grinding process, but also in the surface rolling process,8) and it is expected that the gear-tooth grinding step after heat treatment can be eliminated by improving the tooth profile accuracy in the surface rolling step. This section focuses on the possibility of improving tooth profile accuracy and of eliminating the gear-tooth grinding step by improving the surface rolling conditions from the viewpoint of tooth surface strength.

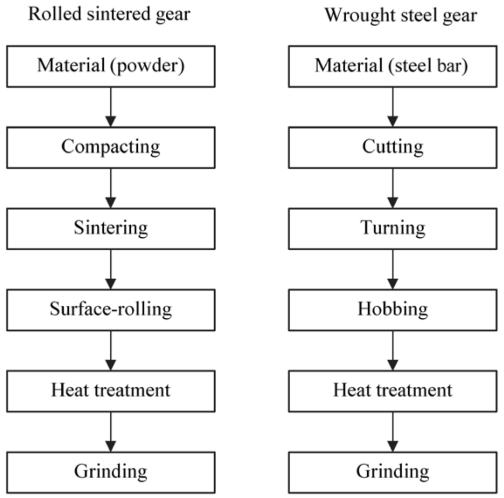

Fig. 4 Comparison of production process between rolled sintered gear and wrought steel gear

2.2 Test method

A 0.5% Ni-1.0% Mo pre-alloyed powder was prepared by water atomization. Graphite powder was added in the amount of 0.3% to prepare a mixed powder for the test. Blanks with a target density of 7.5 g/cm^3 were compacted and sintered in an N_2-10%H_2 atmosphere at 1,120℃ for 60 min. These blanks were cut into the spur-gear shapes specified in **Table 4**, and subjected to surface rolling, followed by carburizing and quenching. Surface rolling was performed on a plunge-type roller under conventional conditions with an amount of stock rolled normal to a tooth flank of 0.14 mm. In addition, as the improved version of these conditions, the amount of stock rolled normal to tooth flank was set to 0.11 mm, and the surface rolling was carried out while the surface rolling die shape was adjusted to improve tooth profile accuracy. Carburizing and quenching conditions were gas carburizing at 930℃ for 120 min and annealing at 160℃ for 120 min. The gear that had been surface-rolled under the conventional conditions was subjected to carburization, quenching and tooth grinding to obtain a tooth profile accuracy of JIS N4-class.

The contact fatigue test was performed on power re-circulating type test equipment and the fatigue limit load was determined as the load when the damaged area did not reach 2% even if the number of load cycles exceeded 1.5×10^7.

2.3 Test results and discussion

Fig. 5 shows the measurement results for the tooth profiles. The tooth profile of the gear that was surface-rolled under the conventional conditions is

Table 4 Specifications of test gear (spur gear)

	Drive	Driven
Material	Evaluation material	SCM420 carburized
Module	3	
Pressure angle (deg.)	20	
Number of teeth	13	26
Face width (mm)	6	10
Standard pitch circle diameter (mm)	39.0	78.0

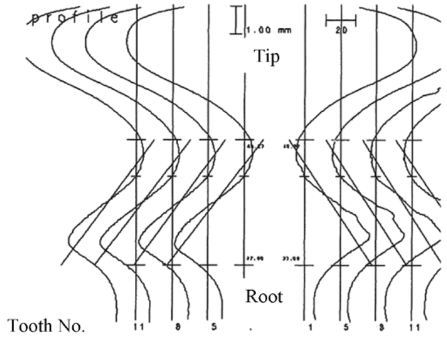

(a) Surface-rolled under conventional rolling condition (without grinding)

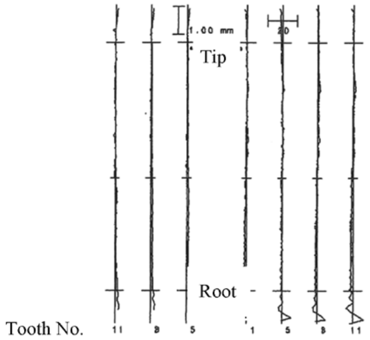

(b) Surface-rolled and ground

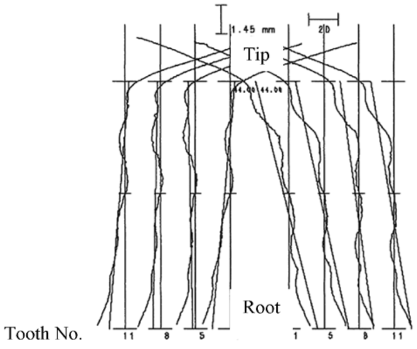

(c) Surface-rolled under modified rolling condition (without grinding)

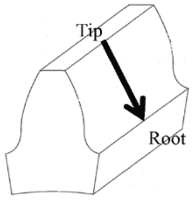

Fig. 5 Comparison of tooth profiles

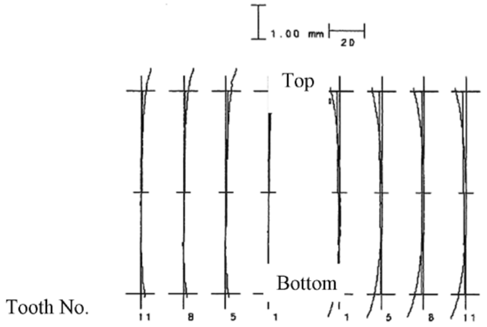

(a) Surface-rolled under conventional rolling condition (without grinding)

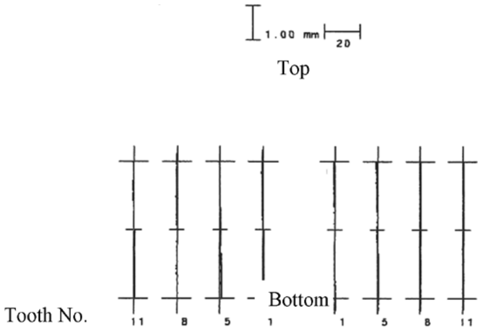

(b) Surface-rolled and ground

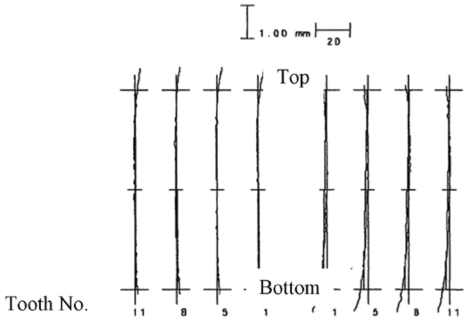

(c) Surface-rolled under modified rolling condition (without grinding)

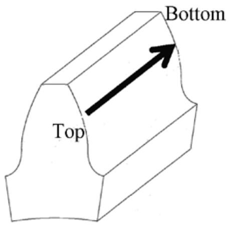

Fig. 6 Comparison of lead profiles

shown in (a), that of the gear surface-rolled under the conventional conditions and ground is shown in (b), and that of the gear surface-rolled under the improved conditions is shown in (c). The gear that was surface-rolled under the improved conditions with the aim of improving tooth profile accuracy had significantly reduced tooth profile errors compared with the one prepared under the conventional conditions. However, it did not reach the same level of accuracy as the tooth ground gear. **Fig. 6** shows the measurement results for the lead profiles. There was almost no difference in the lead profile error between the surface-rolled gear with or without tooth grinding, and each gear showing a favorable lead profile accuracy.

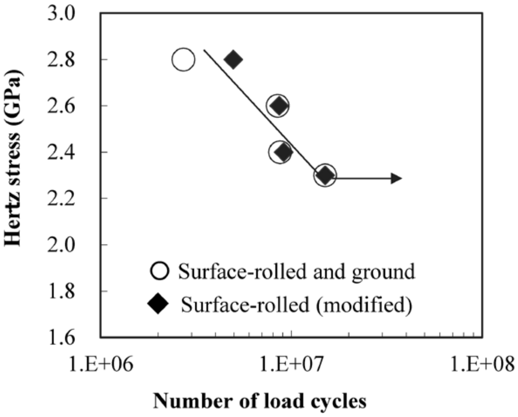

Fig. 7 Results of contact fatigue test

Fig. 7 shows the results of the contact fatigue test. The gear (a) that had been surface-rolled under the conventional conditions caused severe vibration, which led to an abnormal stopping of the test machine, disabling the evaluation of contact-pressure strength. On the other hand, the gear that had been surface-rolled under the improved conditions indicated no problem during the operation test and had the same contact-pressure fatigue strength as that of the tooth ground gears. It is probable that the gear that had been surface-rolled under the improved conditions had a sufficiently small tooth profile error and did not have a decrease in tooth surface strength. It has been shown that, by adjusting the surface rolling conditions, a tooth surface strength life equivalent to that of the tooth-ground gears can be obtained without performing gear-tooth grinding.

Conclusions

The strengthening mechanism and application advantages of the surface-rolled sintered gear have been studied, and the following results were obtained.

(1) Surface-rolled sintered gears have excellent contact-pressure fatigue strength because surface rolling generates a compressive residual stress greater than that of wrought steel gears.

(2) The surface-rolled sintered gear allows the adjustment of the tooth profile accuracy in the surface rolling process, and even if the gear-tooth grinding process after heat treatment is eliminated by adjusting the conditions, the same contact-pressure fatigue strength as that of the tooth ground gear can be achieved.

Finally, we would like to express our sincere gratitude to everyone involved in Suwa University of Science, Tottori University, and NISSEI Co., ltd. for their great cooperation in surface rolling technology and gear evaluation technology of this study.

References

1) T. Takemasu et al. JSMME. 2011, Vol.5, No.12, pp.825-837.
2) S. Nishida et al. Journal of the Japan Society of Powder and Powder Metallurgy. 2014, Vol.61, No.6, pp.318-323.
3) M. Nagahama et al. *R&D Kobe Steel Engineering Reports*. 2006, Vol.56, No.3, pp.53-58.
4) A. Hatano et al. CAMP-ISIJ. 1993, 6, p.796.
5) R. Ishikura et al. DENKI-SEIKO (Electric Furnace Steel), 2010, Vol.81, No.2, pp.99-108.
6) M. Yoshizaki. Transactions of the Japan society of mechanical engineers. C. 2001, Vol.67, No.660, pp.2651-2658.
7) K. Nakamura. Transactions of the Japan Society of Mechanical Engineers. 1966, Vol.32, No.238, pp.1001-1006.
8) H. Sasaki et al. Procedia Engineering. 2014, Vol.81, pp.316-321.

Melting and Casting Technologies for Titanium Aluminide Intermetallics

Daisuke MATSUWAKA*[1] · Tomohiro NISHIMURA*[2] · Fumiaki KUDO*[3] · Yuuzo MORIKAWA*[4] · Hitoshi ISHIDA*[2]

*[1] Application Technology Center, Technical Development Group
*[2] Materials Research Laboratory, Technical Development Group
*[3] Kobelco Research Institute, Inc.
*[4] Production Department, Titanium Plant, Titanium Unit, Advanced Materials Business

Abstract

Alloys based on the titanium aluminide (TiAl) intermetallic compound are lightweight and have excellent high temperature strength and oxidation resistance. Therefore, they are being increasingly used in low-pressure turbine blades of jet engines for commercial aircraft, against the backdrop of fuel consumption reduction needs and the like. Kobe Steel has been working on the development of a manufacturing technology for TiAl material with international competitiveness, devised a melt deoxidation method utilizing the phenomenon of decreased oxygen solubility when high concentration aluminum is added, and achieved an oxygen concentration of 0.03 mass% or less. The company has also realized a narrow composition range (Al content ±0.3 mass%) and improved casting yield (+25% or higher compared with the conventional method) by constructing a melting and casting process using the cold crucible induction melting (CCIM) method. This paper also details the technology for recycling titanium scrap and describes future prospects.

Introduction

Alloy based on titanium aluminide (hereinafter referred to as "TiAl alloy") is light weight, with a density about half that of a Ni-based alloy, and has excellent high-temperature strength and oxidation resistance. Thanks to this, it is increasingly adopted for the low-pressure turbine blades of commercial aircraft jet engines to meet the recent need to reduce fuel consumption and CO_2 emissions.[1), 2)]

The 48-2-2 alloy (Ti-48Al-2Cr-2Nb at.%), the current de facto standard for TiAl alloy, was developed by the General Electric Company. After that, pioneering research and development was vigorously carried out in the 1990s, including work by Takeyama et al., showing the guiding principle for the structural design of the alloy for forging,[3)-5)] and practical applications of TiAl alloys are progressing in Europe, which is highly environment-conscious. In the future, as the practical applications progress further, they are expected to be adopted more widely in next-generation aircraft engines and may possibly spread to other fields.[6)-8)]

In Japan, the Cross-ministerial Strategic Innovation Promotion Program (hereinafter referred to as "SIP"), led by the Cabinet Office, has promoted structural design guidelines and the development of manufacturing technology to improve heat resistance (Innovative Design and Production Technology of Novel TiAl Alloys for Jet-engine Applications).[9)]

This paper presents various issues in the manufacturing technology of TiAl alloy material (melting, casting and recycling) and describes the achievements and future prospects of Kobe Steel's efforts to establish its mass production technology.

1. Manufacturing technology of TiAl base material

1.1 Typical melting and casting process and technical issues

The melting and casting technology of TiAl alloy includes special melting processes such as vacuum arc remelting (hereinafter referred to as "VAR") adopted for titanium and titanium alloys, electron beam melting, plasma arc melting (hereinafter referred to as "PAM"), vacuum induction melting, and cold crucible induction melting (hereinafter referred to as "CCIM").[10)]

High quality is required for TiAl alloy due to its applications. This raises issues especially in ensuring compositional uniformity, which greatly affects the material structure (and thus affects product characteristics), and in reducing casting defects. In order to satisfy such high quality requirements, GfE mbH (Germany), the world's largest company in the field, melts the material by the VAR method and then casts it using a centrifugal casting method.[11)] In addition, since the raw materials are expensive, recycling scrap with a view to cost reduction is expected to become more important in the future as the alloy's applications to aircraft engines expand.

1.2 Melting and casting technology by CCIM method

Table 1 compares the respective technical issues associated with the processes introduced in the previous section. As shown in this table, the CCIM method is considered to be the most suitable, as regards scrap recycling and compositional uniformity, for the melting and casting process of TiAl alloy. Hence, this paper introduces the results of past efforts in the CCIM method.

As mentioned above, in the melting of TiAl alloy, it is most important to keep its components at predetermined concentrations. The CCIM is a method in which an object is strongly agitated by induction heating to be uniformly melted (**Fig. 1**). Since a split-type water-cooled copper crucible is used as the melting container, a solidification skull (solidified shell) is formed in the part that comes into contact with the water-cooled copper. Taking this phenomenon into consideration, Kobe Steel has optimized the arrangement of the raw materials, composition and order of addition, in advance. These efforts have enabled a narrow-width control (± 0.3 mass% of the target) of the Al concentration in the TiAl alloy when an identical composition is melted continuously. On the other hand, in order to improve the quality and to reduce the cost of TiAl alloy castings, it is effective to improve the yield of sound material by reducing the casting defects in the material. Kobe Steel has developed a technology to produce sound material without casting defects by controlling the casting rate in the melting process based on the CCIM method and has successfully improved the yield by 25% or more compared with the conventional method, which involves tilting the water-cooled copper crucible to pour the molten metal into a mold installed below.

1.3 Recycling technology for TiAl alloy scrap

The greatest obstacle in recycling titanium scrap is the increase in impurity elements, one of the main impurity impurities being oxygen. Various techniques have been attempted to deoxidize titanium,[12)-16)] however, the deoxidation of titanium is thermodynamically difficult.

In the case of TiAl alloy also, industrial recycling is limited to the scrap that occurs in-house, and there are various problems in the practical application of recycling excessively contaminated scrap. For this reason, high-grade raw materials with a low oxygen

Table 1 Comparison of technical issues in melting processes for TiAl alloy

Melting process	Atmosphere	Heat source	Homogeneity & composition controllability	Scrap recycle	Total
VAR (skull melt-pour)	Vacuum	Arc	△ : Fair ・double/triple melt required ・evaporation loss (Al, Cr, etc.)	△ : Limited flexibility for electrode preparation	△ Fair
EBM	High vacuum	Electron beam	× : No good ・high evaporation loss (Al, Cr, etc.)	○ : Normal flexibility	× Bad
PAM	Inert-gas	Plasma arc	○ : Good ・depend on blended compositions of additional materials	○ : Normal flexibility	○ Good
CCIM	Inert-gas	Induction heating	◎ : Excellent ・strong magnetic stirring	◎ : High flexibility	◎ Excellent

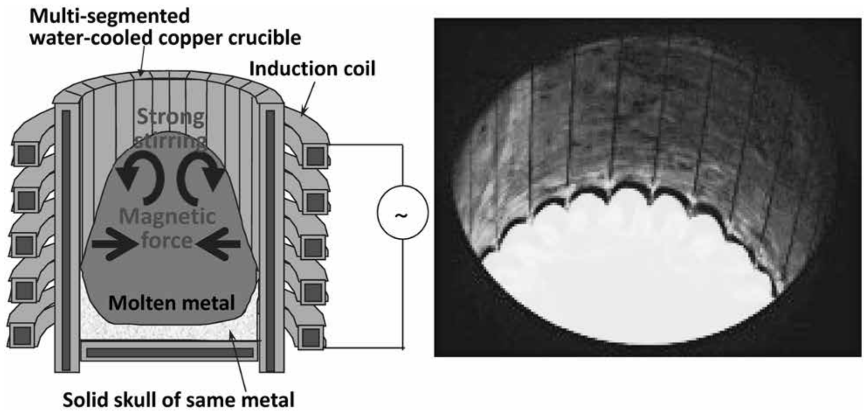

Fig. 1 Schematic diagram of cold crucible induction melting (CCIM)

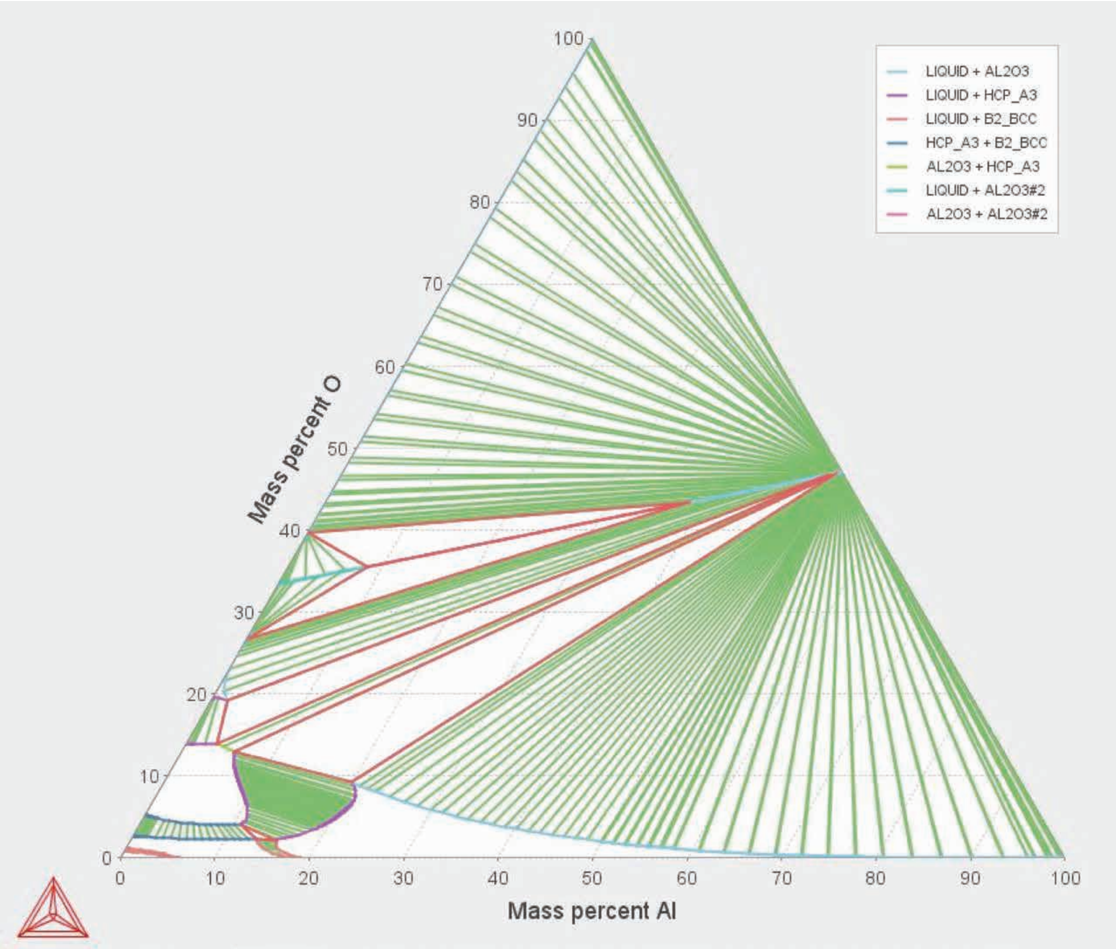

Fig. 2 Ternary isothermal section of Ti-Al-O at 1,973K (calculated by Thermo-Calc)

concentration must be used as the raw materials for TiAl alloy, which is an active metal like titanium.

Hence, Kobe Steel has focused on this thermodynamical feature: the oxygen solubility in the intermetallic compound decreases significantly when the aluminum concentration in a general TiAl alloy is higher than 30-40 mass% and the company has verified the feasibility of performing deoxidation by adding aluminum during TiAl alloy melting (**Fig. 2**). The results are shown in **Fig. 3**. TiAl alloy containing 0.8 mass% oxygen was melted with PAM or CCIM and metallic Al was added. As a result, it has been clarified that deoxidation down to 0.1 mass% or less can be achieved in the high Al concentration region of more than 40 mass%. The product of this deoxidation reaction has been confirmed to be Al_2O_3.

Then, flux was added to separate the molten TiAl alloy from Al_2O_3, in addition to further reducing the oxygen concentration. For the flux, the CaO-CaF_2 system was selected because of its low melting point (easy to melt, with high reactivity) and its high solubility of Al_2O_3. **Fig. 4** shows the results when the flux is added. Comparison of the oxygen concentrations with and without flux addition at a given Al concentration shows that the oxygen concentration has been reduced by the flux addition, as intended. When no flux is added, the deoxidation product Al_2O_3 (spot-like precipitates in the upper photograph of **Fig. 5**) is scattered in the TiAl alloy, which makes it difficult to separate it from the alloy

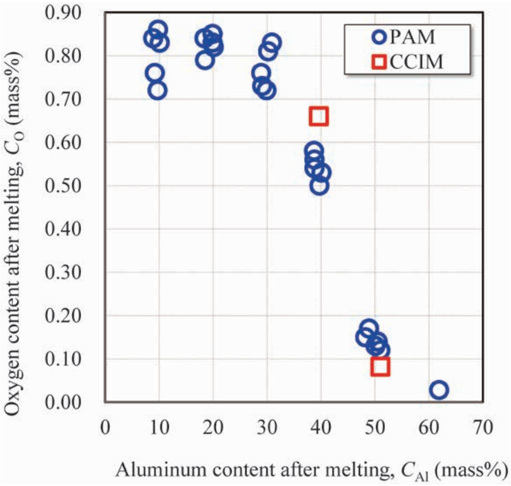

Fig. 3 Effect of aluminum content on deoxidation behavior in molten TiAl alloy

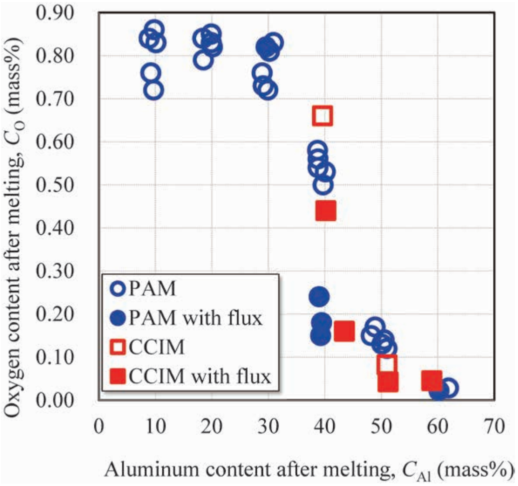

Fig. 4 Effect of flux addition

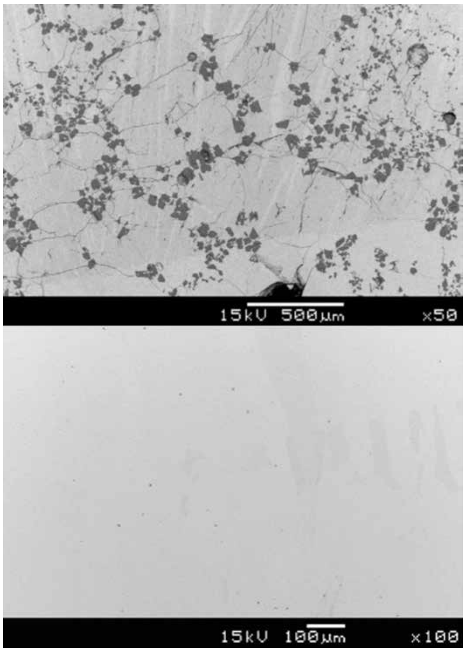

Fig. 5 SEM images of sample cross-sections after melting without flux (upper) and with flux (lower)

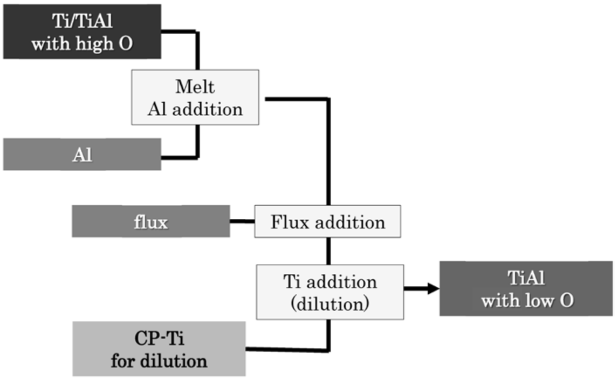

Fig. 6 Schematic diagram for TiAl alloy deoxidation process

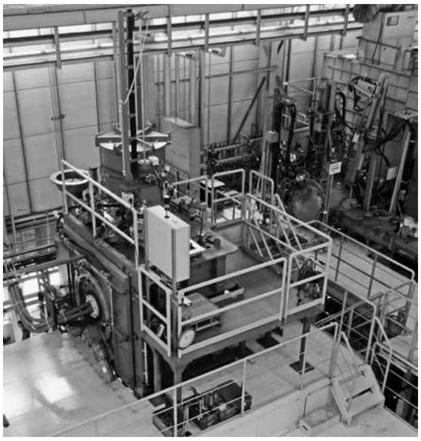

Fig. 7 Appearance of pilot-scale CCIM furnace

after deoxidation. On the other hand, the addition of the flux has been confirmed to eliminate Al_2O_3 from the TiAl alloy solidified after melting (Fig. 5, lower photograph). This is considered to be the result of Al_2O_3 being absorbed in the molten flux. Also, when the obtained TiAl alloy with a high Al concentration is added with Ti for composition adjustment and to dilute the Al concentration, the remaining Al_2O_3 has been confirmed to decompose (dissolve in TiAl alloy again), verifying the points made in this discussion.

The recycling technology utilizing this principle for scrap with highly dissolved oxygen (hereinafter referred to as the "high-Al melt deoxidation method") has a fast reaction rate because the deoxidation reaction proceeds during melting. In the case of the TiAl alloy, the additive amount of Ti (amount of dilution of Al concentration) can be small, so future development for practical applications is expected. **Fig. 6** shows a schematic diagram of this process.

2. Efforts to establish mass production technology

As mentioned at the beginning, Kobe Steel has been working on the development of "high-grade, low-cost ingot manufacturing technology" by CCIM in the SIP project, "Development of innovative manufacturing process for TiAl Blade." The company has used pilot-scale CCIM equipment (**Fig. 7**), which was introduced for the purpose of establishing the technology for mass production and has demonstrated a narrow width control of Al concentration by optimizing the melting conditions to achieve high quality, the reduction of casting defects and improvement of yield by optimizing casting conditions.

3. Future prospects

The aircraft industry is expected to continue to grow at an annual rate of approximately 5%, and the market for TiAl alloy is expected to expand.

To further expand the adoption of TiAl alloy, it is most important to produce the material with higher quality at a lower cost. In particular, the recycling of scrap containing expensive elements is expected to become ever more important. Hence, Kobe Steel believes that the high-Al melt deoxidation method and the CCIM method, which is not restricted by the shape of the scrap, can be promising as mass production technology.

As the additive manufacturing technology is disseminated and the understanding of its merits and demerits progresses, it is expected that the demand for TiAl alloy powder will increase sharply as the conversion from the current manufacturing technology (precision casting, isothermal forging, total machining, etc.) occurs. High-grade, low-cost material manufacturing technology is also indispensable for powder production. For these future issues, Kobe Steel plans to participate in the "Development of Powder Manufacturing Process and Basic Technologies for High Performance TiAl based Alloy Turbine Blades" in "Material Revolution by Integrated material Development System," which is one of the subjects of the second phase of SIP, to continue to upgrade TiAl alloy as a basic technology for mass production.

Conclusions

Attempts have been made to develop the melting and casting processes for low-cost high-quality TiAl alloy, and the following results have been obtained:

(1) Optimizing the composition, arrangement and addition order of raw materials has enabled a narrow width control of Al concentration in TiAl alloy (± 0.3 mass% of the target) when an identical composition is melted continuously.

(2) Controlling the casting rate has improved the yield of sound material without casting defects by 25% or more compared with the conventional method.

(3) A melt deoxidation process has been devised on the basis of the phenomenon of oxygen solubility in the intermetallic compound decreasing as the Al concentration increases.

This work was supported by Council for Science, Technology and Innovation (CSTI), Cross-ministerial Strategic Innovation Promotion Program (SIP), "Structural Materials for Innovation" (Funding agency:JST).

References

1) T. Fujimura et al. Journal of IHI technologies. 2008, Vol.48, No.3, pp.153-158.
2) M. Takekawa et al. Journal of IHI technologies. 2013, Vol.53, No.4, pp.16-19.
3) M. Takeyama et al. Journal of the Japan Society for Technology of Plasticity. 2015, Vol.56, No.654, pp.535-539.
4) Y. W. Kim. Bulletin of the Japan Institute of Metals. 1993, Vol.32, No.2, pp.73-77.
5) E. Schwaighofer et al. Intermetallics. 2014, Vol.44, pp.128-140.
6) T. Tetsui. Materials Science and Engineering: A. 2002, Vol.329-331, pp.582-588.
7) S. Nishikiori. Kinzoku, Materials Science & Technology. 2006, Vol.1038, No.7, p. 738.
8) Y. Koyanagi et al. Titanium・Japan. 2015, Vol.63, No.4, pp.303-306.
9) Cabinet Office. Strategic Innovation Promotion Program (SIP) Phase 1 Evaluation, Final Report. https://www8.cao.go.jp/cstp/gaiyo/sip/saishuhokoku.html (as of 2020-03-26).
10) T. Kusamichi et al. *R&D Kobe Steel Engineering Reports*. 1999, Vol.49, No.3, pp.13-14.
11) V. Guther. Intermetallics. 2018, Vol.103, pp.12-22.
12) G. Z. Chen. Nature. 2000, Vol.407, pp.361-364.
13) K. Ono et al. Materia Japan. 2002, Vol.41, No.1, pp.28-31.
14) T. Okabe. Journal of Japan Institute of Light Metals. 2005, Vol.55, No.11, pp.537-543.
15) T. Ikeda et al. Seisan kenkyu. Monthly journal of the Institute of Industrial Science. 1994, Vol.46, No.6, pp.298-305.
16) Y. Xia. Mater. Trans.. 2017, Vol.58, No.3, pp.355-360.

Evaluation for Morphology of Regions Having Microtexture in Ti-6Al-4V Alloy Forging Products

Dr. Yoshinori ITO*1 · Dr. Hiroyuki TAKAMATSU*2 · Shogo SAEKI*3 · Dr. Nobuhiro TSUJI*4

*1 Materials Research Laboratory, Technical Development Group
*2 Digital Innovation Technology Center, Technical Development Group
*3 Takasago Quality Assurance Department, Advanced Materials Business
*4 Kyoto University Graduate School

Abstract

Titanium alloys contain regions having microtexture, in which the crystallographic orientation of the alpha phase is similar. Because the regions with microtexture deteriorate mechanical properties, it is important to evaluate their morphology. In this study, ultrasonic measurement was conducted, and the results were compared with characterization results obtained by the SEM/EBSD method. It has been verified that backscattered signals by ultrasonic measurement can be used for the evaluation of the regions having microtexture.

Introduction

Titanium alloys are used in aerospace industry thanks to their excellent specific strengths. Ti-6Al-4V is the most popular among titanium alloys. This alloy consists of α phase with hcp structure and β phase with bcc structure, and volume fraction of α phase is approximately 90 % at room temperature.1), 2)

The mechanical properties of titanium alloy depend on the microstructural morphology of α phase. In applications that require high fatigue strength and ductility, the α phase is controlled to be granular. The outline of the process is as follows. First, a lamellar type of α phase is formed by cooling from a high temperature region, in which β single phase is stable, to room temperature. Next, hot forging is conducted at a temperature where the two phases of $\alpha+\beta$ are stable to make the granular morphology of α. After that, solution heat treatment and aging heat treatment are performed in the $\alpha+\beta$ region as needed.

The size of α grains after hot forging, observed by an optical microscope, is as fine as approximately 10 to 20 μm. However, it is reported that α grains form microtexture with a similar crystal orientation over a range exceeding several hundred micrometers, and such regions are called macrozones or microtextured regions.3)-14) This paper refers to these regions as "macrozones." Each macrozone behaves like one large crystal grain and is reported to deteriorate fatigue properties.3), 4) Therefore, in order to provide titanium alloy forgings with excellent quality, it is important to evaluate the macrozone.

Macrozones are generally evaluated by the electron backscatter diffraction in scanning electron microscopes (SEM/EBSD).15), 16) However, this method leads to destructive evaluation, and requires a long time for wide range measurements. For non-destructive evaluation, studies are conducted using ultrasonic waves11), 12), but they are limited to cross-sectional evaluations.

Macrozones (a metallographic structure in a broad sense) are said to affect the scattering behavior of ultrasonic waves. In a study using a Ti-5Al-6V-2Sn alloy forging, Ginty et al. reported that maximum intensity of backscattered signal (the signal of ultrasonic waves that scatter in the direction opposite to the incident direction) is obtained when ultrasonic wave incident in a vertical direction of flat grain boundaries in a macrostructure.17)

Humbert et al. observed the microstructure of an IMI834 alloy forging having a great number of macrozones whose morphologies are long and arranged in parallel to each other, and showed that a large amplitude of backscattering is obtained when an ultrasonic wave incident in the vertical to the extended direction.7) They discussed the reasons that the arrangement of the localized microtextures causes a pseudo-periodic fluctuation of crystal orientation (corresponding to the fluctuation of the elastic modulus described later). However, there are many unclear points about the quantitative effect of localized microtextures on the backscattering behavior of ultrasonic waves.

Hence, Kobe Steel evaluated the morphology of macrozones and its effect on the backscattering behavior of ultrasonic waves in cylindrical material of Ti-6Al-4V alloy.18) The results showed that macrozones elongated in the longitudinal direction were formed and that anisotropy of the amplitude of the backscattered signals was exhibited, which depended on the incident direction of the ultrasonic wave. Moreover, this anisotropy has been shown to be explained by the fluctuation of the elastic modulus caused by macrozones.

The present study conducted a further investigation of the previous study.18) Hence, its purpose is to clarify the effects of the incident direction and incident angle of ultrasonic wave on the amplitude of backscattered signals and to evaluate a three-dimensional morphology of macrozones. The subject material is a Ti-6Al-4V alloy forging, which has been cogged into a cylindrical shape in the $\alpha+\beta$ phase region and has a granular morphology of α.

1. Experimental method

1.1 Preparation of test material

The test material is Ti-6Al-4V alloy. The lowest temperature in the β single phase region (β transus) is 988 ℃. A columnar material having a diameter of 405 mm was heated and held in the β monophase region and then water-cooled. After the oxidation scale on the surface had been removed, cogging and upset forging were performed multiple times in the hot temperature range of $\alpha+\beta$ to obtain a columnar material with a diameter of 165 mm. The forged material was air-cooled to room temperature. Specimens were cut out from this columnar material and used for the evaluation. **Fig. 1** shows the specimen position in forged material and its coordinate system. Hereinafter, the plane vertical to the tangential direction (TD) of the columnar material will be referred to as the "longitudinal section," and the plane vertical to the axial direction (AD) will be referred to as the "transverse section."

1.2 Microstructure of columnar material and SEM/EBSD measurements

The optical micrograph observed for the longitudinal section of the columnar material is shown in **Fig. 2**.[18] In this figure, the gray regions, each observed in the form of a lump, are granular α, which occupies the most region of the microstructure. Although it is difficult to distinguish from the photograph of this magnification, in space of granular α, there exist small colonies which consist of a plate-shaped α phase and a residual β phase.

In this study, electron backscatter diffraction (EBSD) measurement was performed in a scanning electron microscope (SEM) to evaluate the macrozone. At that time, in order to evaluate the three-dimensional morphology, the longitudinal section and the transverse section were evaluated, respectively.

1.3 Ultrasonic measurement

The shape of the specimen is a cuboid with lengths in the radial direction (RD), axial direction (AD), and tangential direction (TD) of 52 mm, 35 mm, and 57 mm, respectively. A frequency of 10 MHz was used for the ultrasonic measurement. The wavelength that propagates through the titanium alloy is approximately 600 μm. A flat probe was immersed in water with the specimen, an ultrasonic wave was sent from the probe, and a backscattered signal from inside the material was received by the same probe. The transmitted ultrasonic wave was a pulsed plane wave. The incident wave was transmitted in 2 directions in the RD and AD of the columnar material. For the measurement in the RD, the incident angle was tilted with reference to the RD (0°). The probe was tilted along two directions, a direction parallel to the AD and a direction parallel to the TD. Measurements were performed with angles tilted at a pitch of 1° in the range of - 4° to + 4°. The backscattered signal was amplified with a gain of 40 dB to make sufficient signal strength for analysis. The strength of the backscattered signal, generated when the ultrasonic wave propagated inside the material, was averaged with respect to the depth direction of the material and was used for the analysis. Hereinafter, this averaged value will be referred to as the "backscattered signal strength."

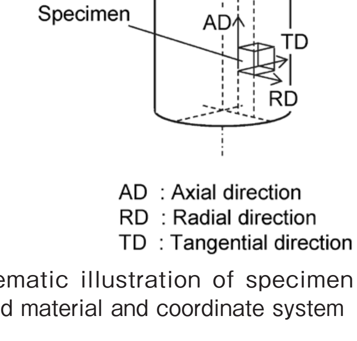

Fig. 1 Schematic illustration of specimen position in forged material and coordinate system

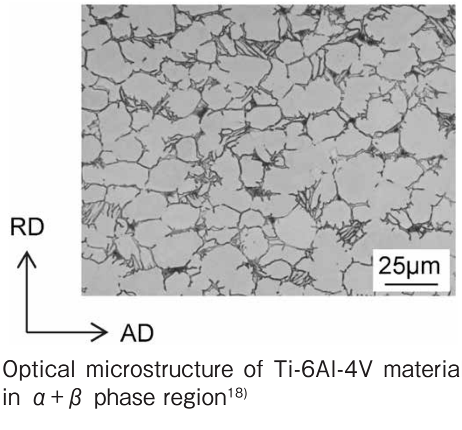

Fig. 2 Optical microstructure of Ti-6Al-4V material forged in $\alpha+\beta$ phase region[18]

1.4 Basic principle of ultrasonic measurement

The ultrasonic wave propagates in a material and scatters at the interface of two regions with different acoustic impedances. The acoustic impedance is expressed by Equations (1) and (2).

$$Z=\sqrt{\rho \cdot V_L} \quad \cdots\cdots\cdots\cdots \quad (1)$$

$$V_L=\sqrt{C/\rho} \quad \cdots\cdots\cdots\cdots \quad (2)$$

wherein Z is the acoustic impedance, ρ is the density of the material, C is the elastic modulus of the material, and V_L is the acoustic velocity of the vertical wave.

The density inside a material is regarded to be homogeneous, and if the material has inside it an inhomogeneous microstructure whose elastic modulus is different from that of the surroundings, scattering occurs at the interface.

The main phase of Ti-6Al-4V alloy is α phase, and this paper focuses on the elastic modulus of α phase. The elastic constants, C_{11}, C_{33}, C_{12}, C_{13}, and C_{44} of an α-phase titanium single crystal consisting of hcp lattice are reported to be 162.4 GPa, 180.7 GPa, 92.0 GPa, 69.0 GPa and 46.7 GPa, respectively.[19] Here, C_{11} and C_{33} are elastic constants in the direction vertical to the c axis of the hcp lattice and in the direction parallel to the c axis, respectively. Because of the symmetry of the hcp lattice, the elastic modulus depends on the angle θ formed by the c axis with respect to the direction of stress loading and is equivalent around the c axis. The change in the elastic modulus with θ is shown in **Fig. 3**.[18] Thus, the change in crystal orientation accompanies the change in elastic modulus, which causes the scattering of ultrasonic waves. That is, the existence of macrozones is envisaged to cause the scattering of ultrasonic waves.

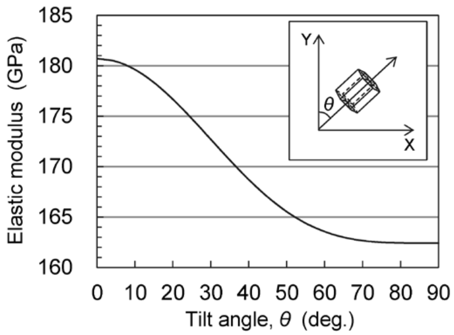

Fig. 3 Relationship between elastic modulus and tilt angle of c-axis in hcp lattice (α phase)[18]

2. Experimental results and discussion

2.1 Morphology of macrozone

Fig. 4 shows the inverse pole figure orientation maps (IPF maps) obtained by SEM / EBSD.[15), 16), 20)] Fig. 4 (a) is the measurement result in the longitudinal section, and Fig. 4 (b) is the measurement result in the transverse section. The coloring of each IPF map has been based on the standard triangle shown in the figure and shows the crystal orientation in the RD of respective measurement point. **Fig. 5** (A) to (H) are (0001) pole figures[15), 16), 20)] of the α phase in the regions A to H shown by the white rectangle frame in Fig. 4 (a).

First, the focus is on the IPF map of the longitudinal section (Fig. 4 (a)). Macrozones are found to be formed extending in the axial direction. Their thickness is several hundred μm and their length exceeds 1 mm. Under the optical microscope, a microstructure of granular α with a diameter of about 20 μm is observed (Fig. 2), while the results of SEM / EBSD measurement show that many adjacent α grains have a similar crystal orientation. Macrozones are also observed in the transverse

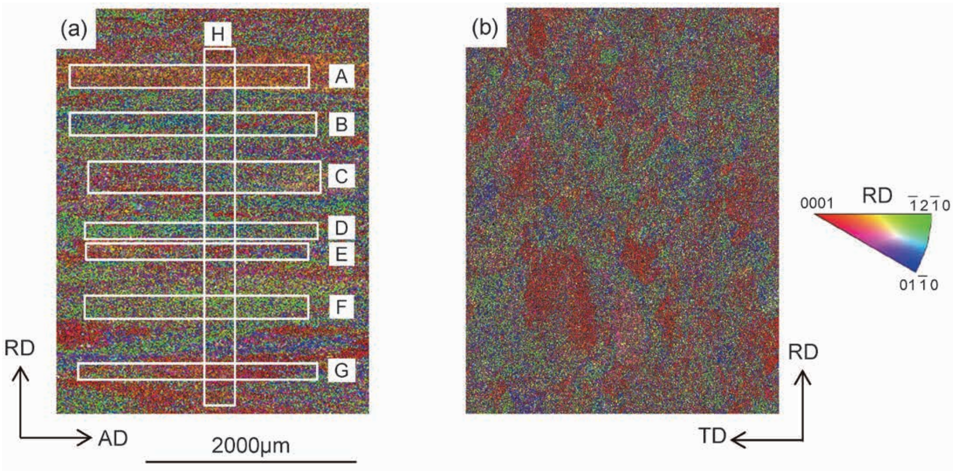

(a) Longitudinal section

(b) Transvers section

Fig. 4 EBSD IPF maps of Ti-6Al-4V material forged in $\alpha+\beta$ phase field

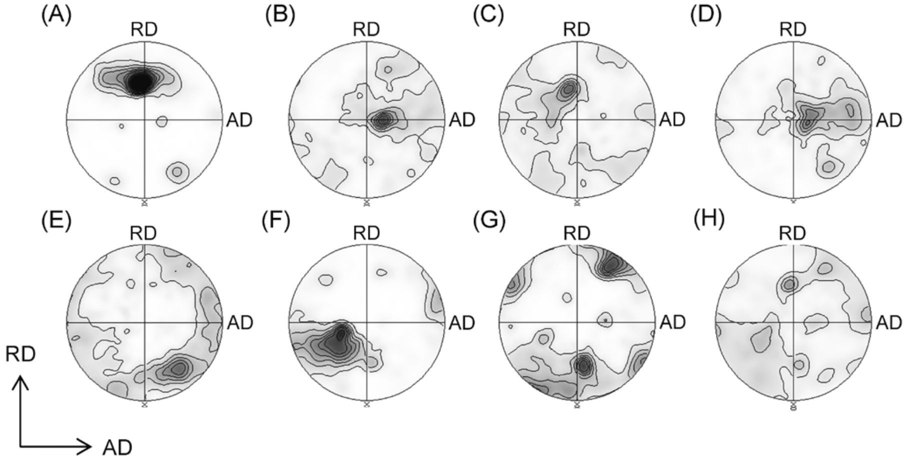

Fig. 5 (0001) pole figures of α phase in region A through H shown in Fig.4 (a)

section (Fig. 4 (b)), but unlike the longitudinal section, they are almost equiaxial in shape. That is, it has been clarified that fibrous macrozones has been formed in the columnar material of the Ti-6Al-4V alloy used in this study.

In order to examine the features of the macrozones recognized in the longitudinal section in detail, the crystal orientation information in the frame indicated by the white rectangle in the figure has been organized in the format of pole figures15), 16), 20) (Fig. 5). The regions A to G lie such that the long side of each rectangle is parallel to the axial direction (AD) of the columnar material, while region H lies such that the long side of the rectangle is parallel to the radial direction (RD). In the region A (Fig. 5 (A)), a strong texture of c-axis is observed in the orientation tilted from the TD to RD. This indicates that the region surrounded by each white rectangle in the IPF map of Fig. 4 (a) can be regarded as if it were a single crystal grain, as expected from the fact that each measurement point is mainly displayed in red or yellow. Similarly, in Fig. 5 (B) to (F), the c-axes are tilted in almost one orientation. However, the orientations of texture are different from each other. For example, in the region B (Fig. 5 (B)) adjacent to the region A, almost all c-axes are tilted in the orientation close to the TD, unlike the region A. The region C (Fig. 5 (C)) and the region D (Fig. 5 (D)) show strong texture in orientations close to the region A and the region B, respectively. In the region E (Fig. 5 (E)) and the region F (Fig. 5 (F)), the observed textures are different from those of the regions A to D. In the region E, relatively high intensity of the c-axes is observed near the opposite side of the RD near the circumference of the pole figure. In the region F (Fig. 5 (F)), relatively high intensity of the c-axis is observed in the vicinity of the orientation tilted parallel from the TD to AD. In the region G (Fig. 5 (G)), unlike the regions A to E, there are approximately three locations at which the intensity of the c-axis is relatively high. As shown in Fig. 3, the elastic modulus of the α phase changes depending on the angle θ. The results of Fig. 4 (a) and Fig. 5 (A)-(G) suggest that a large number of macrozones extending in the AD are formed in the columnar material of Ti-6Al-4V alloy and, due to the difference in crystal orientation (formed angle θ) in each region, the elastic modulus changes at a pitch of several hundred μm along the RD. On the other hand, strong texture isn't found in the region H (Fig. 5 (H)), in which the long sides of the region, from which the crystal orientation information is extracted, matches the RD, and the degree of texture intensity is small compared with the regions A to G. The IPF map in Fig. 4 (a) is considered to indicate that, if the long side of the rectangle matches the RD, the region contains multiple macrozones and shows no strong texture.

As described above, the columnar material of Ti-6Al-4V alloy forged in the $\alpha+\beta$ region has long fibrous macrozones extending in the AD and their crystal orientations (θ) are different from each other. It is considered that this difference has caused the fluctuation of the elastic modulus along the RD. On the other hand, the texture of crystal orientation in the region in the vertical direction is not remarkable, suggesting that the fluctuation of the elastic modulus along the AD is small.

2.2 Strength of backscattered signal obtained by ultrasonic measurement

Fig. 6 shows the strength of the backscattered signal obtained when the columnar material is measured parallel to the RD and AD. Similar to the results of the previous study,18) the backscattered signal strength is greater when measured in the RD than when measured in the AD, showing an

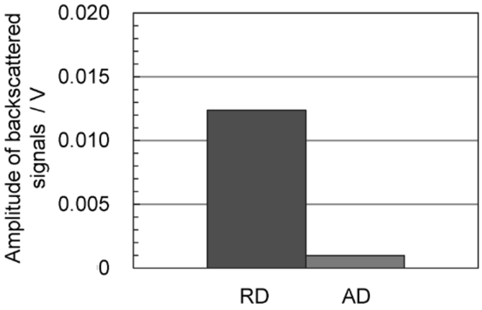

Fig. 6 Amplitude of backscattered signals obtained in RD and AD in ultrasonic measurements on Ti-6Al-4V material forged in $\alpha+\beta$ phase region

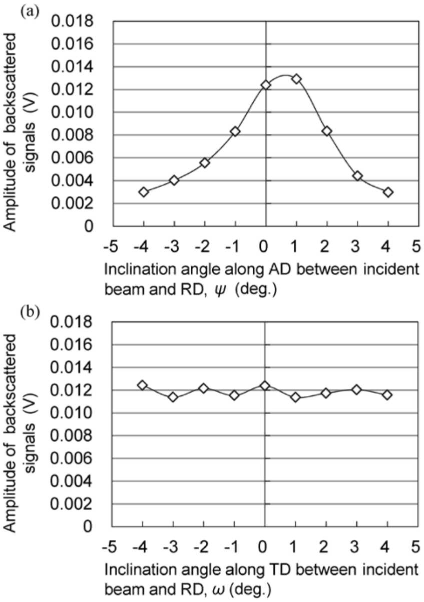

Fig. 7 Influence of incident angles and inclination direction on the amplitude of backscattered signals ((a) inclined along AD, (b) along TD)

anisotropy depending on the measurement direction. In a forging of near α-type titanium alloy, it has been pointed out that the periodic fluctuation of the elastic modulus causes the backscattering of ultrasonic wave.[7)] As shown in the previous section, the columnar material of Ti-6Al-4V alloy used in this study has a macrozone extending in the AD. Although the periodicity has not been evaluated in this study, the fluctuation of the elastic modulus is observed along the RD, in which the pitch of the fluctuation is several hundred μm and is close to the wavelength of the ultrasonic wave. On the other hand, no fluctuation of the elastic modulus is considered to occur along the AD. Therefore, the anisotropy of the backscattered signal strength observed in this study is also considered to be due to the presence or absence of variation in the elastic modulus in the measurement direction. In other words, the backscattering behavior can be said to change reflecting the morphology of the macrozone.

Focusing on the fact that the strength of the backscattered signal of the ultrasonic wave changes depending on the morphology of the macrozone, a study has been conducted on the utilization of the macrozone for morphological evaluation. **Fig. 7** shows the results of study on the changes in the strength of the backscattered signal by tilting the incident angle in the range from -4° to +4° for the measurement in the RD. Fig. 7 (a) shows the results when the tilt is along the AD, and Fig. 7 (b) shows the results when it is along the TD. The zero degree on the horizontal axis indicates that an ultrasonic wave has been sent in parallel with the RD. From Fig. 7 (a), it can be seen that the change in the strength of the backscattered signal is greater when the tilt is made along the AD. The maximum backscattered signal strength is reached at the tilt angle of 1°, and the strength drops sharply regardless of whether the tilt is made in either the positive or negative direction. On the other hand, as shown in Fig. 7 (b), there is almost no change in the strength of the backscattered signal when the tilt is made along the TD. Thus, it has been clarified that the strength of the backscattered signal responds sensitively to the incident angle, and that the change in the strength of the backscattered signal due to the incident angle greatly depends on the tilt direction.

This behavior is considered to be caused by the morphology of the macrozones formed in the columnar material of Ti-6Al-4V alloy. Since this study has investigated the fibrous macrozones extending in the AD, the interface of the macrozones has been formed in parallel to the AD. When ultrasonic wave propagates along the RD, elastic modulus fluctuations are caused by the macrozones, resulting in a backscattered signal with strong intensity. When the incident angle is tilted along the AD, however, the angle between the interface of the macrozone and the incident direction changes accordingly, resulting in slow fluctuations of the elastic modulus along the propagation direction of the ultrasonic wave. This is considered to have caused the sharp drop in the strength of the backscattered signal. It should be noted that the reason for the maximum strength of the backscattered signal being measured at the tilt angle of 1° is presumed that the extension direction of the macrozone is not perfectly parallel to the AD but is slightly slanted.

On the other hand, when the incident angle is tilted along the TD, almost no change occurs in the strength of the backscattered signal. The macrozones are fibrous and have a curved interface in the TD. In addition, the tilt along the TD does not change the relationship between the macrozone and the extension direction. Therefore, it is considered that the change in the variation of the elastic modulus at the incident angle is small, hardly changing the strength of the backscattered signal.

As described above, it has become clear that the strength of the backscattered signal obtained by ultrasonically measuring the columnar material of Ti-6Al-4V alloy is sensitively affected by the incident direction and incident angle, and its behavior is affected by the morphology of the macrozone.

Conclusions

This study has shown that the strength of the backscattered signal of the ultrasonic wave depends on the morphology of the macrozone formed in titanium alloy forgings and changes sensitively depending on its incident direction and incident angle. This phenomenon can be exploited in the morphological evaluation of macrozones by ultrasonic waves. The morphology of the macrozones dealt with in this study are fibrous, however, there may be other morphologies such as pancake-shaped or oval-shaped. It is believed that a more universal morphological evaluation technology can be established by performing similar evaluations on these morphologies. It is considered that the spatial distribution of macrozones also affect the mechanical properties, and further studies will be conducted in the future.

References

1) J. W. Elmer et al. Materials Science and Engineering A. 2005, Vol.391, pp.104-113.
2) S. Kar et al. Metallurgical and Materials Transaction A. 2006, Vol.37, pp.559-566.
3) A. P. Woodfield et al. Titanium 95 Science and Technology. 1995, pp.1116-1123.
4) K. Le Biavant et al. Fatigue & Fracture of Engineering Materials & Structures. 2002, Vol.25, pp.527-545.
5) L. Germain et al. Acta Materialia. 2005, Vol.53, pp.3535-3543.
6) L. Germain et al. Acta Materialia. 2008, Vol.56, pp.4298-4308.
7) M. Humbert et al. Acta Materialia. 2009, Vol.57, pp.708-714.
8) R. Whittaker et al. Materials Science and Technology, 2010, Vol.26, pp.676-684.
9) L. Toubal et al. Metallurgical and Materials Transaction A. 2010, Vol.41, pp.744-750.
10) N. Gey et al. Acta Materialia. 2012, Vol.60, pp.2647-2655.
11) A. Moreau et al. Materials Characterization. 2013, Vol.75, pp.115-128.
12) A. L. Pilchak et al. Metallurgical and Materials Transaction A. 2014, Vol.45A, pp.4679-4697.
13) C. Buirette et al. Materials Science and Engineering A. 2014, Vol.A618, pp.546-557.
14) S. L. Semiatin. Metallurgical and Materials Transaction A. 2020, Vol.51A, pp.2593-2625.
15) S. Suzuki. Materia Japan. 2001, Vol.40, pp.612-616.
16) R. Yoda. Compendium of Surface and Interface Analysis, The Surface Science Society of Japan (ed.). Springer, 2018, pp.127-132.
17) B. Ginty et al. Proceedings of the 14th World Conference on Titanium. 2020., 11021. pp.1-4.
18) Y. Ito et al. MATEC Web Conferences. 2020, Vol.321, p. 11021.
19) E. S. Fisher et al. Physical Review. 1964, Vol.135, pp.482-494.
20) Y. Inagaki et al. Journal of Japan Institute of Light Metals. 2002, Vol.52, pp.494-499.

An Approach to Increase Strength of Materials for Built-up Type Crankshafts

Tsukasa SHIRAFUJI*1 · Hiroyuki TAKAOKA*2 · Ryota YAKURA*2

*1 Steel Powder Plant, Steel Powder Unit, Advanced Materials Business
*2 Engineering Department, Steel Casting & Forging Plant, Steel Casting & Forging Unit, Advanced Materials Business

Abstract

Recently, there is an increasing need for improving the efficiency of low-speed diesel engines for ships. In response, Kobe Steel has newly developed an inexpensive low-alloyed steel for semi-built-up type crankshafts. This steel has a high yield point and high fatigue strength while avoiding the risk of quench cracking, which often occurs in large, forged steel products. Crank throws were manufactured from multiple steel types, including the newly developed steel, and the material properties of samples of steel pieces taken from their major parts were evaluated. The results confirmed that the newly developed steel has mechanical properties and a fatigue strength superior to those of conventional steel. It is expected that this newly developed steel will be applied to next-generation engines and contribute to compliance with environmental regulations, which are expected to become increasingly stringent.

Introduction

In response to the more stringent exhaust gas regulations in recent years, the principal engines of large ships are mainly designed to have high internal pressure and long stroke to improve fuel efficiency. As a result, semi-built-up type crankshafts, which convert the reciprocating motion generated by the explosion force of engines into rotational motion, are exposed to large bending stress generated in the pin fillets of their crank throws. In addition, a large rotational torque is generated between each throw and journal that are shrink-fitted. Environmental regulations are planned to be gradually strengthened in the future,[1] and it is expected that pin fillets and shrink fit parts will be subjected to an increasingly heavy load. Therefore, a high fatigue strength is required for the material of each crank throw to prevent fatigue fracture in the pin fillet. In addition, it is necessary to increase the gripping torque of each shrink-fitted journal to prevent micro-slippage. Hence, material properties with a high yield point are required near the shaft hole of an arm into which a journal is inserted during shrink fitting.

Semi-built-up type crankshafts are mainly made of carbon steel that has been heat-treated by air cooling after normalizing treatment. The tensile strength of the carbon steel is mainly specified to be about 600 MPa. A general method of improving the yield point and fatigue strength includes obtaining a martensitic and/or bainitic microstructure with high tensile strength by quenching during the heat treatment. In the case of large, forged steel products, however, the cooling rate becomes insufficient due to the large mass effect, disabling the transformation of carbon steel. Therefore, low-alloyed steel whose quenching property is enhanced by the addition of elements such as Ni, Cr, and Mo has been selected as a high strength material. The material for semi-built-up type crankshafts is low-alloyed steel strengthened to 800 MPa class.

Quenched low-alloyed steel with high strength, however, is not widely applied to medium or large-sized engines with a cylinder diameter of 500 mm or greater.[2] The reason is that, as the size increases, the risk of cracking upon quenching during heat treatment increases in crank throws that have complicated shapes.[2] Hence, Kobe Steel has developed a low-alloyed steel with a high strength of 800 MPa class in order to improve the yield point and fatigue strength required for the throws of semi-built-up type crankshafts. The newly developed steel requires no quenching and can avoid the risk of quench cracking peculiar to large crank throws.

On the other hand, the fatigue strength of material is known to be affected by the size of internal defects, such as non-metallic inclusions, decreasing as the defect size increases.[3] Hence, Kobe Steel has developed a super-clean steel process technology for reducing non-metallic inclusions, which become the initiation points for fatigue cracks.[2] This process has been confirmed to improve the fatigue strength of large, forged steel products.[4], [5] However, no fatigue characteristics have been verified when it is applied to a semi-built-up type crankshaft.

This paper outlines the mechanical properties and fatigue strength of crank throws (hereinafter referred to as "throws"), applying the technology for the newly developed steel and super-clean steel process, while comparing them with the ones for conventional steel.

1. Manufacturing and material of semi-built-up type crankshafts

Fig. 1 shows the manufacturing process of semi-built-up type crankshafts. A steel ingot cast after melting and smelting is heated and formed into a throw shape by forging and gas cutting. The forming of throws involves four types of methods, each of which is shown in **Fig. 2**. After the forming, the material is heat-treated to obtain the required mechanical properties, and then machined. Next, each journal of the shaft and the throw of the respective eccentric part are connected by shrink-fitting and finished to the specified dimensions by a final machining.

Table 1 shows the chemical composition and method of heat treating the steels prepared in this new process. Also, **Table 2** shows the steel-type manufacturing method, as well as the standard strength in yield point (YP) and tensile strength (TS), of the crank throw. Table 1 includes 32CrNiMo6-3, which is the steel newly developed by Kobe Steel. This steel is air-cooled after normalizing during heat treatment (normalized & tempered). It should be noted that the composition of this steel is designed to make its metallographic structure similar to that of the conventional low-alloyed steel (34CrNiMo6), which is quenched and tempered. Therefore, the newly developed steel has the same strength as the conventional low-alloyed steel, but can avoid the quench cracking peculiar to large, forged steel. It should also be noted that the smelting of No. 1

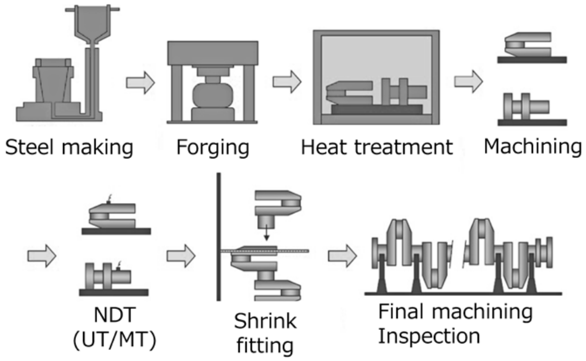

Fig. 1 Manufacturing process of semi-built-up type crankshaft

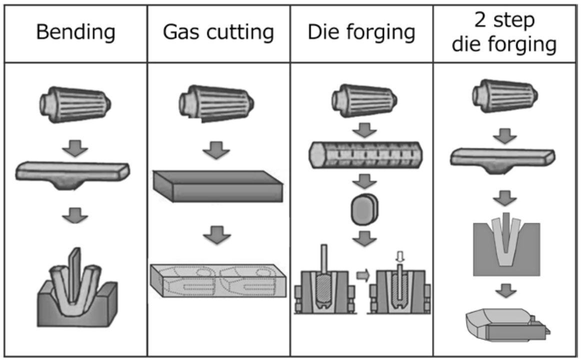

Fig. 2 Forging methods of crank throw

Table 1 Chemical composition and heat treatment methods of test steels

Steel type		Chemical composition (wt%)							Heat treatment
		C	Si	Mn	Ni	Cr	Mo	V	
32CrNiMo6-3 (developed alloy steel)	Max.	0.40	0.40	1.50	1.10	1.60	0.40	0.20	Normalized & tempered
	Min.	0.25	0.15	0.80	0.60	1.10	0.15	—	
34CrNiMo6 (conventional alloy steel)	Max.	0.38	0.40	0.70	1.70	1.70	0.30	—	Quenched & tempered
	Min.	0.30	—	0.40	1.40	1.40	0.15	—	
Carbon steel (conventional steel)	Max.	0.50	0.40	1.40	—	0.30	—	0.12	Normalized & tempered
	Min.	—	—	1.00	—	—	—	0.06	

Table 2 Forged crank throws manufactured from test steels

Throw No.	Steel type	Steel making process	Cylinder size (mm)	Forging method	Specified strength	
					YP (MPa)	TS (MPa)
1	32CrNiMo6-3	Super clean (Developed)	950	2 step die forging	≧590	≧780
2	34CrNiMo6	Tap degassing (conventional)	500	Gas cutting	≧590	≧780
3	Carbon steel	Tap degassing (conventional)	600	Die forging	≧350～370	≧590～610
4	Carbon steel	Tap degassing (conventional)	600	Gas cutting	≧350～370	≧590～610
5	Carbon steel	Tap degassing (conventional)	960	2 step die forging	≧350～370	≧590～610

throw shown in Table 2 has adopted the super-clean steel process technology, which reduces S and O in molten steel and promotes the floating separation of inclusions generated by dissolved oxygen, to reduce both sulfide-based and granular oxide-based inclusions. This has enabled the preparation of a steel ingot with high cleanliness.

In the present approach, the materials shown in Table 2 have been examined, as well as the yield point and fatigue strength in the vicinity of the arm-shaft holes and pin fillets of throws made by different methods. The following sections describe what has been done.

2. Investigation and test method for semi-built-up type crankshaft

2.1 Preparation of test pieces

The steel pieces for tensile testing and fatigue testing were collected from the vicinity of the shaft hole and the crank pin in the arm of a throw produced by the actual manufacturing process. **Fig. 3** shows the collection position of each test piece. From these steel pieces, tensile test pieces were prepared in accordance with JIS 14A (ϕ14 × 70 mm), and fatigue test pieces were prepared as smooth test pieces, each with a parallel part of ϕ10 × 30 mm.

2.2 Fatigue tests

An axial force fatigue test (push-pull) was performed on the fatigue test pieces prepared. The staircase method[6)] recommended by the International Association of Classification Societies (IACS) was used to evaluate the fatigue characteristics. The fatigue test procedure following the staircase method is as follows:

① For the first test piece, a fatigue test is performed at a stress level that is assumed to be close to the mean S_N of fatigue strength.

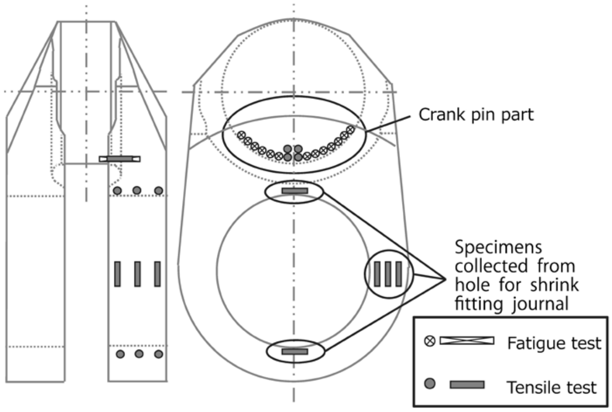

Fig. 3 Collection locations of tensile and fatigue test pieces

② For the second test piece:
②-(1) In the case where the first test piece runs out after predetermined cycles ($N_0 = 2 \times 10^6$ cycles) are loaded during Test ①, the fatigue test is to be carried out at increment stress amplitude by *d*.
②-(2) In the case where the first test piece fails before predetermined cycles ($N_0 = 2 \times 10^6$ cycles) are loaded during Test ①, the fatigue test is to be carried out at decrement stress amplitude by *d*.

③ On the basis of the results of the second test, the fatigue test is continued by changing the stress level acting on the third test piece by *d*.

④ The same test is repeated hereafter.

In this procedure, the differential stress *d* is selected so that it is as close to the standard deviation of fatigue strength as possible. The obtained results are evaluated in accordance with the following procedure.

$$F=\sum f_i,\ A=\sum i f_i,\ B=\sum i^2 f_i \quad \cdots\cdots\cdots (1)$$

wherein, i: Numbering of the stress levels,
f_i: Number of test pieces at the stress level i.

It should be noted that i and f_i in Eq. (1) are to be counted only for the less frequent event, run-out or failure, that occurs in all of the test results.

Using the above *F*, *A*, and *B*, the mean value S_N and standard deviation *s* of the fatigue strength are calculated by the following equations:

$$S_N = S_{a0} + d\left(\frac{A}{F} \pm \frac{1}{2}\right) \quad \cdots\cdots\cdots\cdots\cdots\cdots \ (2)$$

$$s = 1.62d\left(\frac{BF - A^2}{F^2} + 0.029\right) \quad \cdots\cdots\cdots\cdots\cdots\cdots \ (3)$$

Here, S_{a0} is the minimum stress level. It should be noted that regarding the operator in Eq. (2), ±, the operator is to be negative if the number of failures is lower than that of run-outs, and vice versa.[6)]

This method allows the mean fatigue strength and standard deviation to be obtained, enabling statistical evaluation of the fatigue strength. In this paper, the differential stress *d* has been selected to be 25 MPa.

3. Test results and evaluation

3.1 Results of tensile test for shrink fit part

Fig. 4 shows the relationship between the yield point and the tensile strength of the test pieces collected from the vicinity of the journal shaft hole in each arm of No. 1 to 5 throws. It is shown that the yield point and tensile strength of the newly developed steel are greatly improved compared with those of the carbon steel. Also, they are equal to or higher than those of 34CrNiMo6, which is the target of the strength class, showing that they exceed the standard strength exhibited in Table 2.

3.2 Material properties of crank pins

3.2.1 Results of tensile test

Fig. 5 shows the relationship between the yield point and the tensile strength of the test pieces collected from the crank pins of throws No. 1 to 5. The yield point and strength of the newly developed steel are much higher than those of the benchmark, not to mention those of the carbon steel, showing a large margin with respect to the standard strength shown in Table 2.

3.2.2 Results of fatigue test

Fig. 6 shows the results of the fatigue test of the test piece collected from the crank pin of the crank throw made of the newly developed steel. Since there are 4 broken test pieces and 9 unbroken test pieces, the numbering is targeted at the broken test pieces, which have occurred less frequently. Since the minimum stress S_{a0} when the breakages have occurred is 460 MPa, the mean fatigue strength and standard deviation have been calculated by substituting the respective values into Eq. (1) to (3).

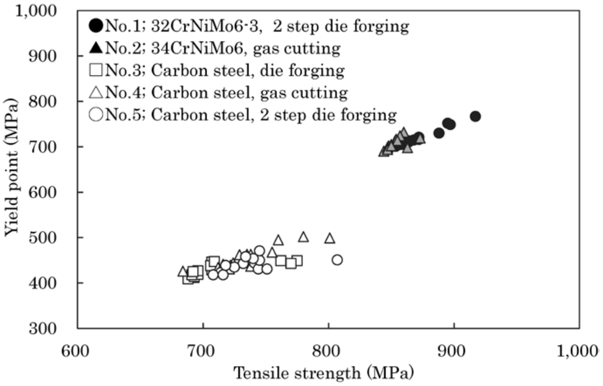

Fig. 4 Tensile test results of specimens collected from crank arm in the vicinity of hole for shrink fitting journal

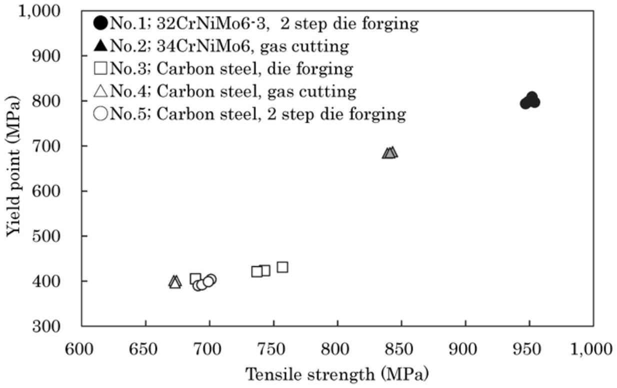

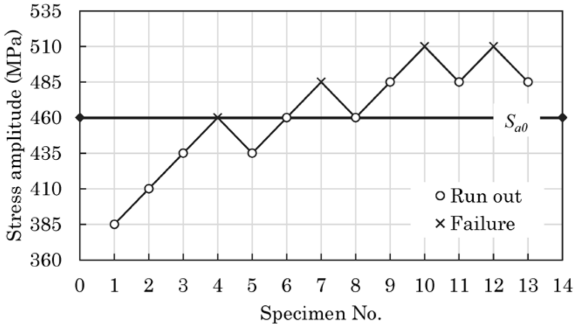

S_a (MPa)	*i*	*fi*	*ifi*	i^2fi
510	2	2	4	8
485	1	1	1	1
460	0	1	0	0
	Σ	*F* = 4	*A* = 5	*B* = 9

Fig. 6 Result of fatigue test using staircase method on developed steel

$$F=4,\ A=5,\ B=9,$$
$$S_N=S_{a0}+d\left(\frac{A}{F}\pm\frac{1}{2}\right)=460+25\times\left(\frac{5}{4}-\frac{1}{2}\right)$$
$$=478.8\,(\mathrm{MPa})$$
$$s=1.62d\left(\frac{BF-A^2}{F^2}+0.029\right)$$
$$=1.62\times 25\left(\frac{9\times 4-5^2}{4^2}+0.029\right)$$
$$=29.0\,(\mathrm{MPa})$$

As with the newly developed steel, the mean fatigue strength and standard deviation have been calculated for the conventional steel by the staircase method. The results are summarized in **Table 3**.

3.3 Evaluation of fatigue characteristics

For the statistical evaluation of fatigue characteristics based on the staircase method, IACS recommends the evaluation be made using the lower limit strength of the confidence interval, assuming that the fatigue strength is normally distributed.[6] When X = (1- α) × 100%, the lower limit of fatigue strength $S_{aX\%}$ at the X% confidence interval is calculated by Eq. (4).[6]

$$S_{aX\%}=S_N-t_{\alpha,\,n-1}\cdot\frac{s}{\sqrt{n}} \quad\cdots\cdots\cdots\cdots\cdots\cdots\cdots\cdots\cdots\cdots\cdots \ (4)$$

Table 3 Mean fatigue strength and standard deviation of test steels for crank throws

No.	steel type	d (MPa)	n	S_N (MPa)	s (MPa)
1	32CrNiMo6-3	25	13	479	29.0
2	34CrNiMo6	25	13	438	17.4
3	Carbon steel	25	13	313	1.2
4	Carbon steel	25	13	263	1.2
5	Carbon steel	25	13	313	1.2

d: Stress increment or decrement
n: Total number of the fatigue test specimens
S_N: Mean fatigue strength
s: Standard deviation

wherein, $t_{\alpha,\,n\text{-}1}$: Inverse function of t-distribution with one-sided probability α and degrees of freedom n-1, and
n: Number of test pieces.

The IACS proposes to use 90% normally as the confidence interval.[6] Accordingly, the calculation has been performed by substituting the lower limit of fatigue strength $S_{a90\%}$ of the 90% confidence interval when α = 0.1 into Eq. (4).

Meanwhile, crankshafts applied to marine engines must satisfy the designed fatigue strength specified by the classification society. In this paper, fatigue characteristics were evaluated by comparing them with the designed fatigue strength σ_{DW} specified by IACS.[6] σ_{DW} is calculated by Eq. (5).[6]

$$\sigma_{DW}=\pm\mathrm{K}\,(0.42\sigma_B+39.3)\times\left(0.264+1.073D^{-0.2}+\frac{785-\sigma_B}{4900}+\frac{196}{\sigma_B}\sqrt{\frac{1}{R_H}}\right) \quad\cdots\cdots \ (5)$$

wherein, D: crank pin diameter (mm)
R_H: pin fillet radius (mm)
σ_B: tensile strength (MPa)
K: coefficient for manufacturing process.

For the coefficient K for the manufacturing process, 1.0 is given to the crankshaft manufactured by free forging, and 1.05 is given to the crankshaft manufactured by the continuous grain flow (CGF) forging.[6] Kobe Steel has obtained special approval from all classification societies for applying K = 1.15 to the solid type crankshafts manufactured by the super-clean steel process. The manufacturing process with high coefficient K allows a crankshaft to be designed with high fatigue strength.

All of the these evaluated crankshafts are manufactured by free forging. Therefore, 1.0 is to be substituted into Eq. (5) to calculate $\sigma_{DW,\,K=1.0}$ and the fatigue strength of each throw is evaluated with normalized $S_{a90\%}$ of each one by $\sigma_{DW,\,K=1.0}$. The results are shown in **Table 4**. It should be noted that the

Table 4 Evaluation of fatigue characteristics at lower limit of fatigue strength with 90% confidence interval

No.	steel type	① σ_B (MPa)	② D (mm)	③ R_H (mm)	④ $\sigma_{DW,\,K=1.0}$ (MPa)	⑤ $t_{0.1,\,n-1}$ (MPa)	⑥ $S_{a90\%}$ (MPa)	⑥ / ④
1	32CrNiMo6-3	951	1,220	90	224	1.4	468	2.09
2	34CrNiMo6	841	645	40	229	1.4	431	1.88
3	Carbon steel	732	720	45	209	1.4	312	1.49
4	Carbon steel	673	730	55	197	1.4	262	1.33
5	Carbon steel	696	990	70	194	1.4	312	1.61

σ_B: Average tensile strength result of crank pin part
D: Diameter of crank pin
R_H: Radius of crank pin fillet
$\sigma_{DW,\,K=1.0}$: Designed fatigue strength (K=1.0)
$t_{0.1,\,n\text{-}1}$: Inverse function of t-distribution with one-sided probability α of 0.1 and degrees of freedom n-1
$S_{a90\%}$: Fatigue limit resulted from 90% confidence interval

tensile strength σ_B is the mean value of the tensile strength at the pin fillet of each crank throw plotted in Fig. 5. It is shown that the values of $S_{a90\%}/\sigma_{DW,\,K=1.0}$ for each throw are 1 or greater, which exceeds the designed fatigue strength. In particular, the crank throw manufactured by applying super-clean steel process technology and two-step die forging has excellent fatigue characteristics equivalent to $K = 2.09$ and has a large margin against the designed fatigue strength.

Conclusions

Test pieces have been collected from crank throws made of the newly developed steel and conventional steel, and their mechanical properties and fatigue characteristics have been evaluated. The following is an overview of the results:

- The vicinity of the journal shaft hole in the arm of a crank throw made of the newly developed steel has a higher yield point than the ones made of conventional steel. It also has a yield point higher than the strength standard for the conventional low-alloyed steel.
- The crank throw of the newly developed steel, the throw manufactured by super-clean steel process technology and die forging, has a high fatigue strength and its lower limit fatigue strength at 90% confidence interval is converted into the coefficient of designed fatigue strength specified by IACS UR M53 to be 2.09, indicating excellent fatigue characteristics.

On the basis of these results, Kobe Steel has obtained a special approval from many classification societies including Class NK that the newly developed steel, 32CrNiMo6-3, is the material for built up crank shafts, whose specified yield point is 650 MPa and tensile strength is 850 MPa, which are higher than conventional low-alloyed steels. In addition, the semi-built-up type crank throw made of newly developed steel through super-clean steel process technology and die forging has obtained a special approval for 1.15 as the value of the coefficient K for the manufacturing process, the coefficient in Eq. (5) for designed fatigue strength, as in the case of a solid crankshaft.2) As a result of obtaining these approvals, it has become possible to design the gripping torque and fatigue strength of semi-built-up type crankshafts to be higher than before by applying the above described original Kobe Steel technology.

It is expected that the newly developed steel and manufacturing technologies will be applied to the next generation engines and contribute to the response to environmental regulations, which are becoming increasingly stringent.

References

1) T. Yonezawa et al. Marine Engineering : Journal of the Japan Institution of Marine Engineering. 2019, Vol.54, No.5, p.680.
2) N. Fujitsuna. Kobe Steel Engineering Reports. 2016, Vol.66, No.1, pp.2-6.
3) Y. Murakami. Metal Fatigue: Effects of Small Defects and Nonmetallic Inclusions. Yokendo Co. Ltd., 1993, 265p.
4) T. Shinozaki et al. Kobe Steel Engineering Reports. 2009, Vol.59, No.1, pp.94-97.
5) R. Yakura et al. 27th CIMAC Congress. 2013, Paper No.442.
6) International Association of Classification Societies, "Calculation for I.C. Engine Crankshafts, Unified Requirement M53". 2017.

Automatic X-ray Stress Measurement System for Cold-rolled Fillet of Solid-type Crankshafts

Dr. Mariko MATSUDA[*1] · Hitomi ADACHI[*1] · Tatsuhiko KABUTOMORI[*2] · Dr. Hiroyuki TAKAMATSU[*3]
Dr. Toshihiko SASAKI[*4]

[*1] Engineering Department, Steel Casting & Forging Unit, Advanced Materials Business
[*2] Production Department, Steel Casting & Forging Plant, Steel Casting & Forging Unit, Advanced Materials Business
[*3] Digital Innovation Technology Center, Technical Development Group
[*4] Kanazawa University

Abstract

In recent years, attention has been being paid to global environmental problems, and even higher fatigue strength is required for crankshafts used in medium-speed diesel engines for onshore power generation. Surface treatment technology is drawing attention as one of the means to achieve this. In any of the surface treatment technologies, however, a tensile residual stress, which causes a decrease in fatigue strength, occurs at the boundary between the surface treated part and the untreated part, and it is necessary to understand the residual stress distribution around the surface treated part. This paper describes the evaluation of the influence of the macro-segregation peculiar to large, forged steel, and the X-ray incident angle and incident angle setting error, generated during fillet measurement, on the accuracy of X-ray stress measurement by the cosα method. Improvement measures are also described. In addition, the effectiveness of a system that can automatically and high-speed measure the residual stress in the cold rolled fillet has been demonstrated.

Introduction

Recently, the efforts to address global environmental problems have become more active, and reducing greenhouse gas emissions has become a major proposition for medium-speed diesel engines used in onshore power generation. To increase the efficiency and output of engines, crankshafts, which are the main components of engines, are also required to have higher strength and higher fatigue strength than ever before.

Kobe Steel has achieved high fatigue strength by high cleanliness, i.e., reducing the non-metallic inclusions that are inherent in the steel forgings of crankshafts for medium-speed diesel engines,[1)] and has been working on further increasing the strength of the materials. However, as it has become clear from general high-strength steel, there are concerns about gigacycle fatigue[2)] in high-strength materials exceeding 1,200 MPa, and it is becoming clear that an improvement in fatigue strength cannot be expected to match the increase in production cost.

Hence, surface treatment technology is attracting attention for its potential of further increasing the fatigue strength.[3), 4)] Kobe Steel has been developing cold rolling technology for a long time. Cold rolling results in a greater surface treatment depth than other surface treatments and is applicable to large crankshafts.[5)] Any surface treatment technology including, but not limited to, cold rolling, suffers from a problem with tensile residual stress caused at the boundary between the surface treated part and the untreated part when compressive residual stress is imparted to the surface treated part. It has been known that compressive residual stress generally improves fatigue strength, while tensile residual stress decreases it.[6)] Therefore, when designing a component to be surface treated, it is important to understand the residual stress distribution around the surface treated part.

One of the non-destructive technologies for measuring residual stress is X-ray stress measurement. The conventional X-ray stress measurement based on the $\sin^2\psi$ method,[7)] however, involves the use of large apparatuses, each requiring a large space for measurement, making it difficult to perform measurement on narrow parts such as the fillets of crankshafts. In response to this situation, a small portable X-ray stress measurement apparatus based on the cosα method has become commercially available recently.[8), 9)] This apparatus enables simple residual stress measurement in a factory even for crankshaft fillets. However, it has not been long since the use of this apparatus for general purposes began to spread and it reached its current degree of use, and there are still few studies measuring practical materials, compared with the $\sin^2\psi$ method. Therefore, when applying it to the actual crankshafts, which are large, forged steel products, it has been necessary to confirm the validity of the technique.

Also, in the case of X-ray stress measurement based on the cosα method, the measurement accuracy is known to decrease with a decreasing X-ray incident angle,[10)] which is recommended to be around 35°. In the case of crankshafts for medium-speed diesel engines, their size is relatively small among large, forged steel products, and even if X-ray stress measurement is performed with a small apparatus based on the cos α method, the incident angle at the time of fillet measurement may have to be 20° or lower. In addition, the dimensional tolerances of the actual products make it difficult to accurately grasp the X-ray incident angle for fillets with concave surfaces. Therefore, an error may occur between the input incident angle for stress analysis and the actual incident angle. This has made it necessary to verify the influence that the X-ray incident angle and incident angle error in the cos α method have on measurement accuracy. Furthermore, when measuring narrow parts such as the fillet of a crankshaft, it is an extremely complicated task to irradiate the measurement spot with X-ray under appropriate measurement conditions without making the apparatus come in contact with the measurement target. Thus, automating the X-ray measurement of fillets has been a challenge for practical application.

It is against this backdrop that Kobe Steel studied the validity of the X-ray stress measurement based on the cos α method for low alloy steel with a bainite structure, a typical material, with the aim of applying the measurement to the large, forged steel parts used for the crankshafts of medium-speed diesel engines.11) Also studied was the influence on the accuracy of X-ray stress measurement of an error occurring between the input incident angle for X-ray stress analysis and the actual incident angle.12) Furthermore, an automatic X-ray stress measurement system has been developed for the measurement of the fillets of crankshafts. The use of this measurement system has been confirmed to enable the simple measurement of a cold-rolled crankshaft fillet with high accuracy. This paper reports on the results of these studies.

1. Overview of X-ray stress measurement technology based on cos α method

X-ray stress measurement has been studied for a long time, and in it, a technique called the $\sin^2\psi$ method has hitherto been common.13) In recent years, attention has been focused on measurement by the cos α method using a two-dimensional detector. The X-ray stress measurement principle by the cos α method was first proposed by Taira et al.14) in 1978, using a photographic film as a detector.

After that, an imaging plate (hereinafter referred to as "IP") appeared in the 1980s, and Yoshioka et al.15) studied the cos α method using IP as a detector. The size of pixels on the IP was usually a little large, 100 μm, and the pixels were arranged in a grid pattern. Therefore, the application of the cos α method required a high accuracy conversion into X-ray diffraction intensity profiles on a polar coordinate system. In addition, data processing technology with 1/10 pixel or smaller was required for practical stress measurement accuracy. Furthermore, accuracy in determining the center position of the diffraction ring and the smoothing of the image were also important factors.

After 1994, Sasaki et al. solved these series of problems and established the X-ray stress measurement system based on the cos α method using IP.10) In addition, validity was shown for triaxial stress,16) macro / micro stress,17) and the case where the crystal grain is coarse,18) which had been the problems of X-ray stress measurement. However, the X-ray exposure section and the IP reading section were separated, making the workability generally low and inhibiting widespread use.

In 2009, at JST's new technology briefing session, Sasaki called for the instrumentation of the technology. Taking this as an opportunity, since 2012 several companies have commercialized integrated machines and the like, dedicated to the cos α method one after another. Since the cos α method allows stress measurement by a single X-ray irradiation, the apparatus is smaller, and the space required for the measurement is smaller than that required for the $\sin^2\psi$ method. Furthermore, the advantage of a short measurement time has been demonstrated, and it is now beginning to spread widely.

The cos α method is a technique for obtaining a 360° diffraction ring from a single X-ray irradiation with a two-dimensional detector and calculating stress from the change in the two-dimensional diffraction ring due to the strain of the sample. **Fig. 1** shows the definition of X-ray optics for acquiring a diffraction ring by the cos α method. Here, ψ_0 represents the X-ray incident angle, and 2η represents the angle between the incident X-ray and the diffracted X-ray. The circumference angle α of the diffraction ring in the figure is the angle seen

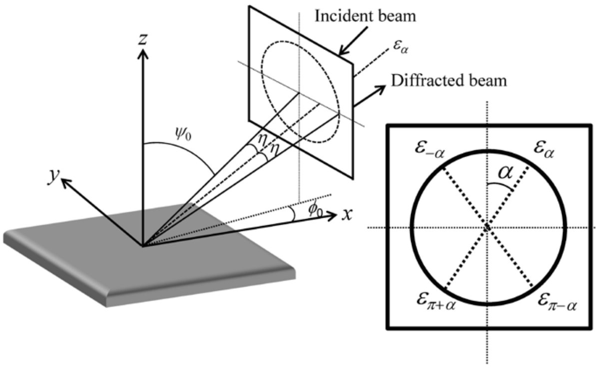

Fig. 1 X-ray optics used for cos α method

from the X-ray tube side. When the X-ray strains whose circumferential angles are α, $-\alpha$, $\pi+\alpha$, and $\pi-\alpha$ are defined to be ε_α, $\varepsilon_{-\alpha}$, $\varepsilon_{\pi+\alpha}$, and $\varepsilon_{\pi-\alpha}$, respectively, the parameter a_1 is defined from these strains and is expressed by the following equation.

$$a_1 = \frac{1}{2}\{(\varepsilon_\alpha - \varepsilon_{\pi+\alpha}) + (\varepsilon_{-\alpha} - \varepsilon_{\pi-\alpha})\} \quad \cdots\cdots\cdots\cdots\cdots\cdots \text{(1)}$$

Assuming a plane stress state and angle η being constant, the following equation holds for the relationship between the stress σ_x in the x direction at the X-ray irradiation point and a_1.

$$a_1 = -\frac{1+\nu}{E}\sin 2\eta \sin 2\psi_0 \cos\alpha \cdot \sigma_x \quad \cdots\cdots\cdots\cdots\cdots\cdots \text{(2)}$$

Here, E and ν represent the X-ray Young's modulus and Poisson's ratio of the sample, respectively. From Eq. (2), a linear relationship holds for $\cos\alpha$ and a_1 ($\cos\alpha$ diagram), and, using the slope of that line, σ_x can be calculated by the following equation.

$$\sigma_x = -\frac{E}{1+\nu}\frac{1}{\sin 2\eta \sin 2\psi_0}\left[\frac{\partial a_1}{\partial \cos\alpha}\right] \quad \cdots\cdots\cdots\cdots\cdots\cdots \text{(3)}$$

The above procedure enables the calculation of stress from the changes in the diffraction ring acquired by a two-dimensional detector.

2. Validity of X-ray stress measurement based on cos α method for crankshaft material of large, forged steel products[11)]

A typical material applied to the crankshafts of medium-speed diesel engines is CrMo-type low alloy steel with a bainite structure. **Table 1** shows the range of content ratio for each chemical composition. In the production of large, forged steel products such as crankshafts for diesel engines, it is difficult to completely avoid macro segregation that occurs in the solidification process of steel ingot. Hence, an evaluation has been conducted on the influence that the high or low macro segregation has on the accuracy of X-ray stress measurement by the $\cos\alpha$ method.

Even if X-ray stress measurement is performed on an actual component, it is difficult to verify the measurement accuracy without knowing the correct value of the residual stress that actually occurs. Therefore, it was decided to perform an X-ray stress measurement for verification on a test body whose stress is known. In other words, a specimen was cut out from an actual component, and an X-ray stress measurement was performed with the tensile stress applied by a universal tensile testing machine. At this time, the accuracy of the X-ray stress measurement was verified by comparing the stress obtained by the X-ray stress measurement with the nominal stress generated in the parallel portion of the specimen. **Fig. 2** shows the appearance of the testing setup. The specimen was a platelet of L150 × W20 × t3 mm. For specimen collection, micro-observation on the cross-section of the actual component was performed to identify sites with high segregation, and two samples were taken from each of the sites with high segregation and those with low segregation.

Table 2 shows the mechanical properties of each specimen. **Fig. 3** shows the observational results of the structure and grain size of the X-ray irradiation site in the specimen with high segregation, and **Fig. 4** shows similar observational results for specimens with low segregation. The main material

Table 1 Range of chemical composition ratios

(mass %)

	C	Si	Mn	Ni	Cr	Mo
Max.	0.45	0.40	1.20	0.50	2.50	0.35
Min.	0.36	0.15	0.80	0.30	1.50	0.15

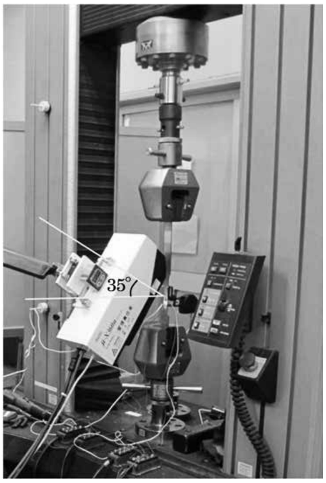

Fig. 2 Tensile test to confirm accuracy of X-ray stress measurement

Table 2 Mechanical properties of specimens

	Tensile strength (MPa)	Proof stress (MPa)
1st. specimen with high segregation	945	813
2nd. specimen with high segregation	987	828
1st. specimen with low segregation	1,035	899
2nd. specimen with low segregation	966	818

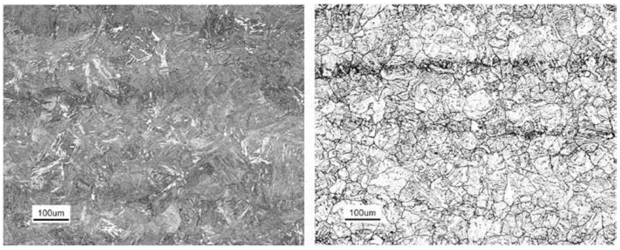

Fig. 3 Microstructures on center of specimen with high segregation

structure of all the specimens was bainite. The average grain size of the specimens with high segregation was 30 to 40 μm, and the average grain size of the specimens with low segregation was 20 to 30 μm, both of which were found to be sufficiently fine for the X-ray stress measurement. However, the specimens with high segregation had a mixed structure in which coarse crystal grains were partially present.

The μ-X360 long range model manufactured by Pulstec Industrial Co., Ltd. was used as the X-ray stress measurement apparatus. In order to exclude the influence of the affected layer that occurs when the specimen is cut out, each specimen was electropolished for a depth of 0.1 mm across a range of 15 × 12.5 mm in the center of the parallel portion. **Fig. 5** shows the appearance of the electropolished area, the X-ray stress measurement position, and their numbers. The X-ray stress measurement was performed at a total of 9 points, 3 × 3 points at a pitch of 3 mm, in the central 9 × 9 mm area in the electropolished part. The Lorentz approximation method, which is the default for μ-X360, was used to determine the peak position of the X-ray diffraction profile. Also, the X-ray elastic constant, $E / (1 + \nu) =$ 175 GPa, recommended by the Society of Materials Science, Japan (JSMS) for ferritic/martensitic steel[19] was used. The X-ray measurement conditions are shown in **Table 3**.

The nominal stress loaded on the specimen by the universal tensile testing machine was set within the elastic stress range, that is, 3 conditions of 1/4, 1/2 and 3/4 of the 0.2% proof stress. Specifically, X-ray stress measurement was performed while gradually increasing the load from the unloaded state. The main purpose of the second specimen was to confirm the reproducibility of the first result. Therefore, with an eye to measurement efficiency, X-ray stress measurement was performed under the condition of only 1/2 of the 0.2% proof stress. The nominal stress generated in the parallel portion of the specimen was calculated from the load cell value of the test machine and the cross-sectional area of the parallel portion of the specimen. At this time, to determine the influence of electropolishing, only the decrease in the thickness of the parallel portion of the specimen was examined. It is considered that stress concentration occurs at the boundary of the electropolished part, and that electropolishing on only one side causes a slight stress difference between the obverse side and reverse side of the specimen. However, preliminary verification has confirmed that their influence is small.

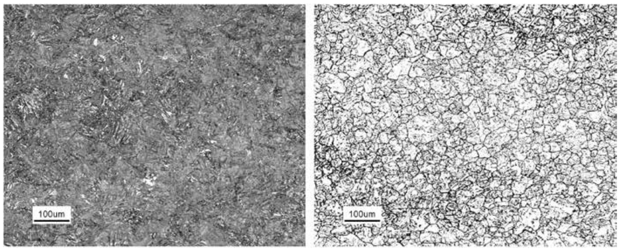

Fig. 4 Microstructures on center of specimen with low segregation

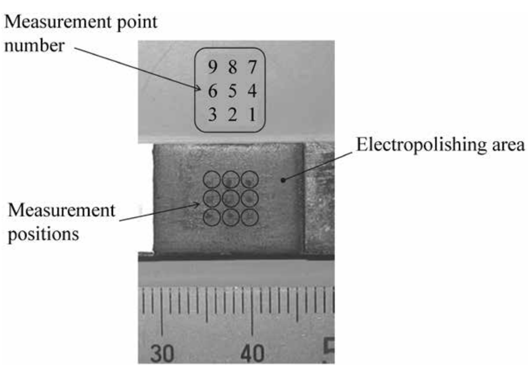

Fig. 5 Appearance of electropolishing area and X-ray measurement positions and their numbers

Fig. 6 shows the results of X-ray stress measurement at 9 measurement positions on the first high-segregation specimen and low-segregation specimen. The low-segregation specimen indicates no significant difference in the measured value at the 9 measurement positions for all the applied stresses, whereas the high-segregation specimen is found to have a significant variation in the measured values among the 9 measurement positions. In

Table 3 X-ray measurement conditions

Characteristic X-ray	Cr-K_{α}
Diffraction plane	αFe (211)
Tube voltage	30 kV
Tube current	1 mA
Irradiated area	3 mm^2
Fixed time	30 s
ψ_0 tilt angle	35°
Diffraction angle in stress free	156.4°
Filter	Vanadium foil

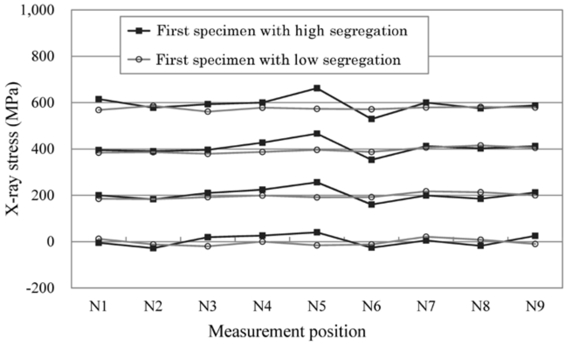

Fig. 6 Results of X-ray measurement at each position of first specimen

addition, the high-segregation specimen shows a large value at the N5 position and a small value at the N6 position, and this tendency is found to be the same regardless of the applied stress of the specimen. This suggests that some conditional difference in the segregated part influences the X-ray stress measurement.

One of the factors that greatly influences the X-ray stress measurement peculiar to the part with segregation is the bias of carbon concentration in the segregated part. If the carbon concentration differs for each X-ray irradiation site, the appearance rate of the second phase such as cementite will be different, which will affect the variation in the stress measurement of the ferrite phase by X-ray. Hence, elemental analysis by FE-SEM was performed by the EDS analyzer on the 9 positions of X-ray stress measurement in the second specimen collected from the high-segregation part. Since the area of the EDS analysis is much smaller than the area of the X-ray irradiation range, elemental analysis was conducted at two different points within the X-ray irradiation range and their average values were used. The results of the elemental analysis are shown in **Fig. 7**. The concentrations of carbon and each alloying element tend to be different for each measurement position. Therefore, the focus has been only on the carbon concentration, which has the greatest influence on the appearance rate of cementite and thus influences the X-ray stress measurement. A comparison was made between the carbon concentration and the X-ray stress measurement value at 9 measurement positions (**Fig. 8**). For the vertical axis in the figure, the difference between the nominal stress and the measured value has been taken. As shown, when the carbon concentration is high, the measured value tends to be higher than the nominal stress, and when the carbon concentration is low, the measured value tends to be lower than the nominal stress. Therefore, the bias of carbon concentration in the segregated part is considered to be one of the causes of the variation in the measurement values of X-ray stress.

Next, **Fig. 9** compares the average values of the X-ray stress, measured at the 9 measurement positions, with the nominal stress in the high-segregation specimen and the low-segregation specimen. Each plot in the figure shows the average value of the measurement at the 9 positions on the respective specimen, and the error range shows the range of maximum and minimum values among the 9 positions. The line in the figure shows the condition where the measured value and the nominal stress match. The average of the values measured at the 9 positions in the first specimen

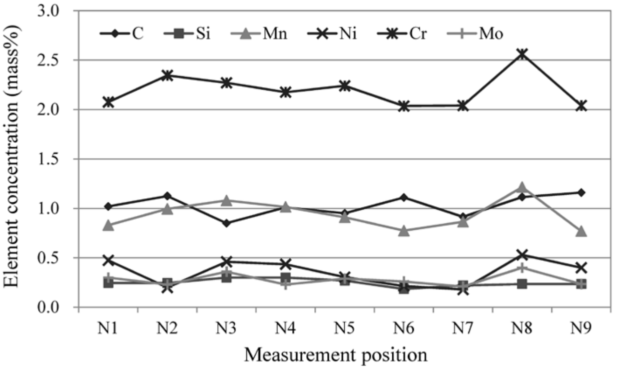

Fig. 7 Element concentration at each position of second specimen with high segregation

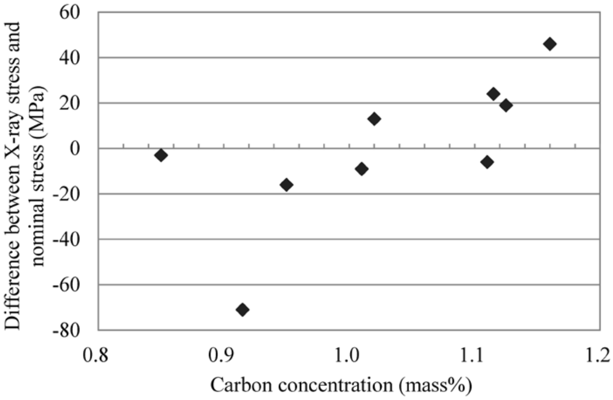

Fig. 8 Relationship between carbon concentration and difference between X-ray stress and nominal stress in second specimen with high segregation

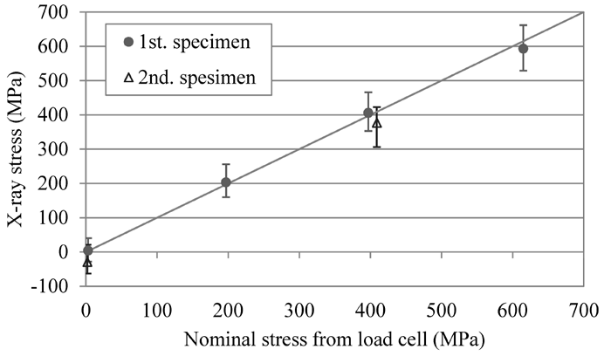

(a) First and second specimens with high segregation

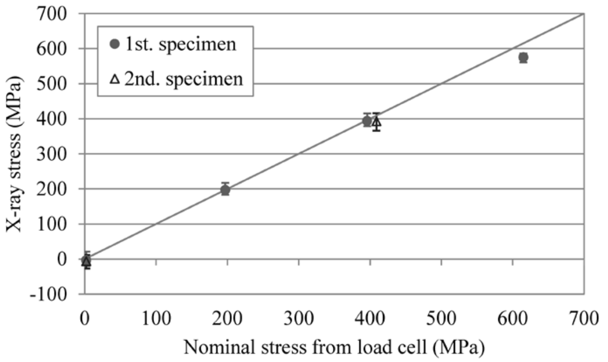

(b) First and second specimens with low segregation

Fig. 9 Comparison between mean value of X-ray stress and nominal stress at 9 measurement points shows a good agreement between the measured value and the nominal stress for both the high-segregation specimen and low-segregation specimen. On the other hand, in the case of the second specimen, there is a slight difference between the measured value and the nominal stress. Some initial residual stress occurs in the unloaded state, and the slope of the average measured value of the 9 positions is equivalent to that of the first specimen, thus, the initial residual stress is considered to have influenced the measured X-ray stress value.

From these results, in the case of high-segregation specimens, the measured value varies greatly for each X-ray irradiation position, and thus it is difficult to conclude that the measurement with only one point is sufficient for measurement accuracy. Averaging the results of the measurements at 9 positions, however, shows a good agreement between the measured values of X-ray stress and the nominal stress, which is a result similar to the one of low-segregation specimen. Therefore, an adequate number of measurement points (or a sufficient X-ray irradiation area) that can minimize the influence of segregation have been examined. For the 9 measurement positions, all the combinations of adjacent positions when the number of measurement points are 1, 2, 3, 4, 6, and 9 have been considered, and the average value of the X-ray stress measurement at each measurement position has been taken. **Fig.10** compares the high-segregation specimens and low-segregation specimens for the relationship between the number of measurement points and the average X-ray stress value under the condition of 1/4 of the 0.2% proof stress (nominal stress 197 MPa). Both the high-segregation specimen and the low-segregation specimen tended to approach the nominal stress of 197 MPa as the number of measurement points increased. In the case of high-segregation specimens, the error due to the influence of segregation is found to be significantly reduced by 3 points of measurement; and having 4 points of measurement is found to result in the variation of the measured value being at the same level as that of a low-segregation specimen. In the present study, the measurement has been performed under the condition of having the X-ray irradiation area be approximately 3 mm^2, and if the X-ray is irradiated to an area of 4 positions or more, that is, approximately 12 mm^2 or greater, and the measured value is averaged, the influence of segregation can be suppressed to the minimum. In this study, multiple points were measured and averaged. Other means include "using an oscillation method that averages the diffraction ring by swinging the measurement device or the measurement target while irradiating the X-ray," "increasing the X-ray irradiation diameter," and "measuring and averaging the values for the same site with multiple X-ray incident angles." These means are also based on the same idea as this method of increasing the number of crystals from which the diffraction information is retrieved, and all of them are considered to be effective.

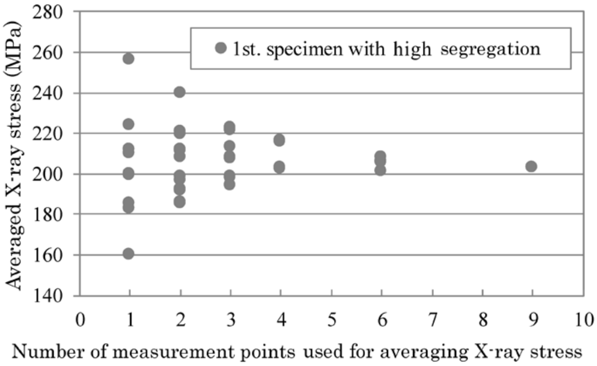

(a) First specimen with high segregation.

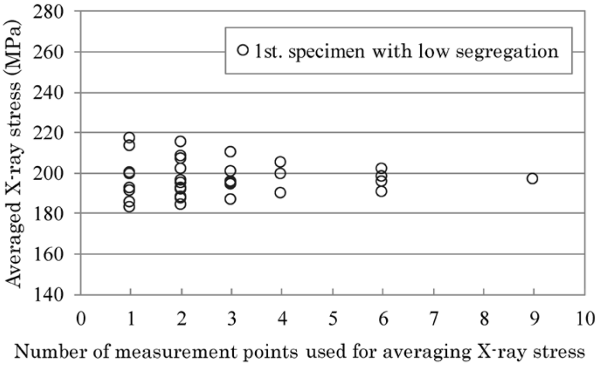

(b) First specimen with low segregation.

Fig.10 Relationship between number of measurement points used for averaging X-ray stress and averaged X-ray stress in case of nominal stress of 197 MPa

3. Influence of X-ray incident angle and incident angle setting error on accuracy of fillet measurement (12)

It has been shown that the accuracy of the X-ray stress measurement based on the cos α method decreases at the low incident angle.(10) However, when the fillet of a crankshaft for a medium-speed diesel engine is measured, the irradiation may have to be done with only a lower incident angle than recommended, depending on the measurement position. In addition, the dimensional tolerances of actual products make it difficult to accurately grasp the X-ray incident angle on the concave curved surface of a fillet. Hence, an investigation has been done to verify the influence of the X-ray incident angle and its setting error on the X-ray stress measurement accuracy based on the cos α method.

First, the influence of the X-ray incident angle on the accuracy of X-ray stress measurement was evaluated. Steel pieces were collected from a portion with low segregation in CrMo-based low alloy steel having a bainite structure, equivalent to the one described in Section 2, to prepare a platelet specimen of L150 × W20 × t3 mm. This specimen was subjected to a 4-point bending test, in which X-ray stress measurement was performed by the cos α method with a tensile (bending) stress loaded. The stress generated in the specimen was calculated from the values of the strain gauge attached to the back surface (concave side) of the specimen. In addition, electropolishing was performed with a depth of 150 μm in a range of 10 × 10 mm at the center of the specimen, and stress measurement was performed at the center of the specimen for the X-ray incident angles of 35°, 15°, 10° and 5°. The detail of the conditions of X-ray stress measurement were roughly the same as those described in Section 2.

Fig.11 shows the influence of the X-ray incident angle on X-ray stress measurement accuracy. The horizontal axis indicates the nominal stress caused by the 4-point bending, the vertical axis indicates the measured value of the X-ray stress, and the solid line in the figure indicates the condition where the nominal stress and the measured value match. For the X-ray incident angles of 10° to 35°, the measured value and the nominal stress are almost the same, but for the incident angle of 5°, the measured value deviates significantly from the nominal stress. In other words, the X-ray incident angle of less than 10° results in an accuracy of X-ray measurement that is insufficient for practical use.

Next, the influence of the setting error of the X-ray incident angle on X-ray stress measurement accuracy has been examined. The stress caused by the cos α method is calculated by Eq. (3) using the slope of the straight line of the cos α diagram. Hence, under the conditions where E and ν are constant and η is assumed to be constant, the slope of the straight line has been calculated for each X-ray incident angle of the cos α diagram, in which σ_x becomes 400 MPa. In addition, theoretical calculation has been conducted for the change in σ_x when the input incident angle for calculating the stress using Eq. (3) deviates by ± 1° and ± 2° from the actual incident angle. **Fig.12** shows the results of the theoretical calculation for the X-ray stress measurement error when the incident angle errors of ± 1° and ± 2° occur for the X-ray incident angle of 5° to 45°. When the incident angle is 35° or higher, the influence of the incident angle error on the measurement error is small. It is shown that the lower the incident angle, the greater the influence of the incident angle error, and when the incident angle is lower than 10°, the influence of the incident angle error becomes huge. It is also shown that, when the incident angle error shifts to the positive side, the influence of the incident angle error becomes smaller than when it shifts to the negative side. It has also been found that the measured stress for the incident angle error shifted to the positive side is smaller than the actual stress, and the measured stress for the incident angle error shifted to the negative side is greater than the actual stress. When residual stress is evaluated, an appropriate judgment must be made as to which shift provides the safer-side evaluation on the basis of the theoretical calculation of this paper.

As a result of the above study, it has been found that the conditions with an X-ray incident angle lower than 10° are inappropriate in terms of measurement accuracy regardless of the influence of either the low incident angle or the incident angle setting error. In other words, for measuring the fillets of crankshafts, it is important to set the measurement conditions so that the X-ray incident angle is 10° or higher.

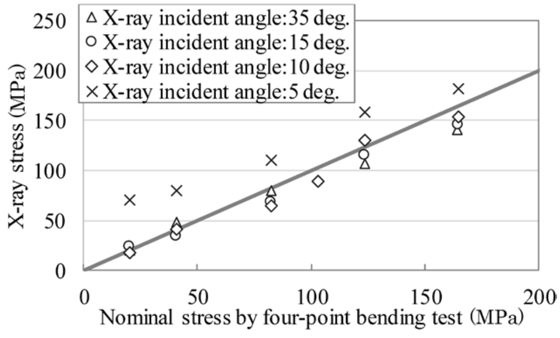

Fig.11 Influence of X-ray incident angle on accuracy of X-ray stress measurement

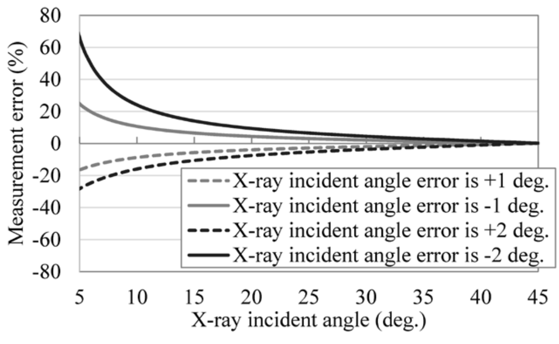

Fig.12 Relationship between X-ray incident angle and measurement error

4. Development of automatic X-ray stress measurement system

On the basis of the results of the above studies, attention must be paid to the following points for the application of the X-ray stress measurement based on the cos α method to the fillets of crankshafts for medium-speed diesel engines.

1) In order to minimize the influence of macro segregation peculiar to large, forged steel products, measurement must be done with multiple points, or with multiple X-ray incident angles and the results must be averaged or with oscillation method.
2) The X-ray incident angle must be set as high as possible (10° or higher), while the incident angle setting error must be kept to the minimum.

There is a limit to the X-ray irradiation distance that can be used for the measurement depending on the measurement position. Therefore, it is necessary to find a measurement condition for setting the X-ray incident angle as high as possible within the constraint range of not hitting the measurement target. However, since the fillets have concave surfaces, the X-ray incident angle and irradiation distance are, respectively, angles and distances relative to the fillet measurement position. Although it is possible to obtain these values by theoretical calculation and determine the optimum setting conditions for the apparatus, it is difficult to actually set the apparatus to the optimum conditions by hand. In addition, since multiple points are measured, it is necessary to set the apparatus multiple times for each measurement point, which requires a huge amount of time and labor.

Hence, Kobe Steel has developed an automatic X-ray measurement system (**Fig.13**). This system includes four types of transfer mechanisms, ① to ④, as shown in Fig.13. Mechanism ① is a rotation mechanism for the crankshaft, and mechanisms ② and ③ are for the transfer in the parallel and vertical directions of the axis of the crankshaft, respectively. Mechanism ④ is a rotation mechanism for adjusting the X-ray incident angle. The transfer mechanisms ② and ③ are used to set the apparatus within the allowable range of X-ray irradiation distance, and the mechanism ④ is used to set the X-ray incident angle as high as possible. This system has a function for judging contact between the measurement target and the apparatus, while a list of the position to be measured and the X-ray measurement conditions can be set in the control unit. This function enables continuous measurement at multiple different positions of the crankshaft fillet without hitting the apparatus on the measurement target, and also supports the oscillation method. For example, by moving only mechanism ① without changing the positional conditions of mechanisms ② to ④, it is possible to perform multiple-point measurement or use the oscillation method while rotating the apparatus in the circumferential direction of the axis of the crankshaft.

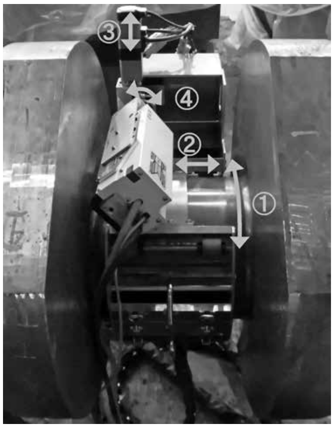

Fig.13 Appearance of developed automatic X-ray measurement

Fig.14 shows the results of X-ray stress measurement when this system is applied to a cold-rolled fillet. The horizontal axis represents the angle (fillet angle) of the direction along the fillet with respect to the center of curvature of the fillet, the left vertical axis represents the results of the X-ray stress measurement, and the right vertical axis represents the X-ray incident angle at the time of each measurement points. It has been confirmed that the cold-rolled fillet is imparted with sufficient compressive residual stress for improving fatigue strength.

Fig.14 shows the measurement results of only one position for each fillet angle. If there is concern about the influence of the macro segregation peculiar to large, forged steel products, the measurement accuracy can be improved by measuring multiple points in the circumferential direction of the axis

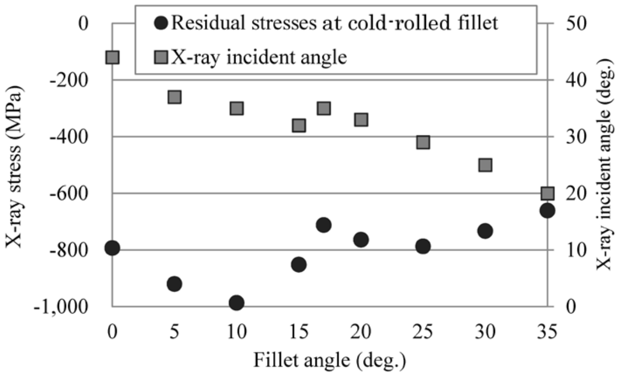

Fig.14 Measurement results of X-ray stresses and X-ray incident angles at cold-rolled fillet of crankshaft

where the cold-rolling condition is considered to be homogeneous, or by using an oscillation method. In manual measurement, there is a concern that the measurement accuracy may decrease due to an error in the incident angle setting. On the other hand, the present system sets the incident angle by the rotation mechanism (④) shown in Fig.13, which suppresses the setting error of the incident angle to the minimum.

From the results of the above studies, this system is considered to be effective in improving the accuracy of X-ray stress measurement based on the cos α method for crankshaft fillets of medium-speed diesel engines.

Conclusions

This paper has confirmed that, in the case of the CrMo-based low alloy steel, which is a typical material for crankshafts for medium-speed diesel engines, the macro segregation peculiar to large, forged steel products decreases the accuracy of X-ray stress measurement based on the cos α method. Furthermore, it has been confirmed that multipoint measurement or the oscillation method is effective in suppressing the influence of macro segregation to the minimum.

Also confirmed is the fact that an X-ray incident angle lower than 10° deteriorates the measurement accuracy significantly. When an error occurs between the actual X-ray incident angle and the set incident angle during the stress measurement of a fillet, it has been confirmed by theoretical calculation that the lower the incident angle, the greater the influence of the incident angle error on the stress measurement accuracy.

As a means for solving these accuracy problems, Kobe Steel has developed an automatic X-ray stress measurement system. It has been shown that, when this system is used to measure a cold-rolled crankshaft fillet, highly accurate measurement can easily be performed while suppressing the influence of macro segregation and incident angle setting error to the minimum.

References

1) Ryota Yakura et al. the 27th CIMAC World Congress 2013 in Shanghai. No.422.
2) T. Sakai et al. Journal of The Society of Materials Science, Japan. 2000, Vol.49, No .7, pp.779-785.
3) T. Frondelius. the 28th CIMAC World Congress 2016 in Helsinki. No.180.
4) R. Elvira et al. the 20th International Forgemasters Meeting. 2017.
5) H. Nagasaka et al. R&D Kobe Steel Engineering Reports. 1998, Vol.48, pp.68-71.
6) M. Matsuda et al. Marine Engineering : Journal of the Japan Institution of Marine Engineering. 2020, Vol.55, No.1, pp.3-10.
7) I. C. Noyan et al. Residual Stress Measurement by Diffraction and interpretation. Springer-Verlag, 1987.
8) Y. Maruyama et al. Journal of The Society of Materials Science, Japan. 2015, Vol.64, No.7, pp.560-566.
9) K. Nagao. Journal of the Surface Finishing Society of Japan. 2015, Vol.66, No.12, pp.636-641.
10) T. Sasaki et al. Journal of The Society of Materials Science, Japan. 1995, Vol.44, No.504, pp.1138-1143.
11) M. Matsuda et al. Journal of The Society of Materials Science, Japan. 2019, Vol.68, No.3, pp.285-291.
12) M. Matsuda et al. Japanese Society for Non-destructive Inspection, Proceedings of the 48th Symposium on stress-strain measurement and strength evaluation. 2017, pp.97-100.
13) Japan Society of Materials Science Edition. Revised X-ray stress measurement method. Yokendo Co.,Ltd. 1981.
14) S. Taira et al. Journal of The Society of Materials Science, Japan. 1978, Vol.27, No.294, pp.251-256.
15) Y. Yoshioka et al. Journal of the Japanese Society for Non-Destructive Inspection. 1990, Vol.39, No.8, pp.666-671.
16) T. Sakai et al. Transactions of the Japan Society of Mechanical Engineers (A). 1995, Vol.61, No.590, pp.2288-2295.
17) T. Sakai et al. Transactions of the Japan Society of Mechanical Engineers (A). 1996, Vol.62, No.604, pp.2741-2749.
18) T. Sakai et al. Transactions of the Japan Society of Mechanical Engineers (A). 1997, Vol.63, No.607, pp.533-541.
19) X-ray Material Strength Division Committee, Stress measurement and elasticity subcommittee. Journal of The Society of Materials Science, Japan. 1971, Vol.20, pp.1257-1271.